Coordination and Control of Uuman Eye and Head: A Classical Mechanics Approach

by

Indika B. Wijayasinghe, B.Sc.

A Dissertation

In

Mathematics and Statistics

Submitted to the Graduate Faculty
of Texas Tech University in
Partial Fulfillment of
the Requirements for the Degree of

Doctor of Philosophy

Approved

Bijoy K. Ghosh, Ph.D.
Chairman of the Committee

Clyde F. Martin, Ph.D.

Eugenio Aulisa, Ph.D.

Akif Ibraguimov, Ph.D.

Name-of-the-Dean-of-Graduate-School
Dean of the Graduate School

August, 2013

ACKNOWLEDGEMENTS

I wish to express my sincere gratitude to Dr. Bijoy K. Ghosh, without whom this work would not have been possible. I greatly appreciate the guidance and support he provided, which covered academics and all aspects of life. I would like to thank for the patience shown in working with me and also for the enormous amount of time spent on guiding me towards a successful work. Thank you for being an excellent mentor.

I wish to thank the committee members Dr. Clyde F. Martin, Dr. Eugenio Aulisa and Dr. Akif Ibraguimov for the guidance they have provided throughout my time in graduate school. Their help and support have greatly contributed to the success of this work.

I would also like to acknowledge the valuable support from our research collaborators, Dr. Stefan Glasauer, Dr. Olympia Kremmyda, Dr. Ulrich Buttner, Dr. Jr-Shin Li and Dr. Justin Ruths. Without their support, this work would not have been a success.

I wish to express my special thanks to Dr. M. P. B. Ekanayake for the guidance and support he has given me for many years including in the process of applying to Texas Tech University.

My thanks also go out to all the faculty members at the Department of Mathematics and Statistics for the knowledge and the support they have provided me during my time at Texas Tech University. I also would like to extend my gratitude to the staff members for helping me in numerous ways to make this journey a success.

It is important to mention and acknowledge the support provided by my parents and my brother. This journey would not have been possible without them. I would also like to thank my extended family for all the support and blessings they have provided.

Last but not least, I would like to thank all my colleagues and friends who stood by me during my time at Texas Tech University. I would like to extend my especial thanks to my roommates and to the members of the Sri Lankan Students' Association for all their support.

TABLE OF CONTENTS

ABSTRACT

The work detailed in this dissertation is on the head/eye control problem, which has been of interest to scientists since the 19th century. Some of the earlier work on this subject were done by prominent scientists such as F. Donders, J. Listing and H. von Helmholtz. In the recent decades, scientists such as D. Robinson, M. Ceylan, D. Tweed, J. Crawford, B. Glenn and T. Vilies, have done notable work on head/eye movement. This work is an extention of the work done by A. D. Polpitiya, W. P. Dayawansa, C. F. Martin and B. K. Ghosh.

In this research we use a classical mechanics approach to study the head/eye movement problem. The head and the eye are modeled as spheres pivoted at the centers and their dynamics are studied under the constraints proposed by Donders and Listing.

The eye movement, the head movement and the head/eye coordination problem are studied under two different control strategies; namely potential control and optimal control. The results are then compared with measured head/eye movement data from human subjects.

LIST OF TABLES

LIST OF FIGURES

CHAPTER 1
INTRODUCTION

The interest in the head/eye movement dates back to 1845 when prominent scientists such as Listing [35], Donders [16], and Helmholtz [59] conducted notable studies. They have observed that normally the head and the eyes do not have three degrees of rotational freedom, but move in constrained rotational spaces such that the gaze direction specifies the orientation of the head/eye. This phenomenon is referred to as the Donders' Law and for the case of the eye, it is referred to as Listing's Law. It can be noted that within boundaries, the head and the eyes can mechanically rotate with three degrees of freedom and in the case of the head, the person can voluntarily move the head with three degrees of freedom. Normally, however, the head-neck system and the oculomotor system chose to give up one degree of freedom and obey a Donders' law.

In the following chapters we study the eye movement, the head movement and the head/eye coordination under two different control strategies; namely potential control and optimal control. In the potential control, we use an imaginary potential engergy term and a friction term to generate the control torques required to drive the head/eye. The optimal control uses calculus of variation to derive the control torques while minimizing a suitable cost function.

The trajectories generated by the two control methods are then compared with measured head/eye movement data from human subjects. This enables us to measure how close the two control strategies are to the actual behavior of human head/eye controls.

In Chapter 2 we study eye movement and head movement dynamics with and without constraints described by Listing's and Donders' laws. We analyze a specific class of Donders' laws and provide a Donders' Theorem which explains the relation between the heading direction and the possible orientations of the head. Equations of motion are derived for rotational dynamics in unconstrainted rotation space ($SO(3)$), and for rotational dynamics that satisfy Listing's law and Donders' law. The dynamics of the eye and the head are analyzed with and without external torques. Rotations without external torques generate the geodesic curves. We introduce a potential

control in which, the external torques are generated by a suitable imaginary potential function and a friction term. Simulation are done to generate the geodesic curves and trajectories between two desired orientations using the potential control. A half angle rule that provides a relation between the angular velocities the Donders' law is also stated.

Chapter 3 is exclusively on head movements that satisfy a specific class of Donders' laws that can be expressed by a quadratic relation. Fick gimbal, a two gimbal system that is a special case of the quadratic Donders' laws, is also studied. A new parameterization (Tait-Bryan angles) is used for the rotation space. A new form of a potential function and a friction term that are independent of the parameterization are introduced in this chapter. This enables the utilization of different paraterizations to generate identical rotations. In this chapter we use the potential control and also an optimal control that minimized a suitable cost function, in order to generate trajectories between two orientations extracted from measured human head movement data. The simulated trajectories are then compared with the actual trajectory as extracted from the data. The comparisons are extended to the calculated torques and the cost.

The problem of head/eye coordination in order to capture and retain a stabilized image is studied in Chatper 4. This is aimed at replicating the vestibulo-ocular reflex in which the eye compensates for the slower head movement. Head/eye coordination is studied under potential control and optimal control. Simulated trajectories are generated using the two control strategies and the target and the final head orientations are extracted from the measured head/eye data. Comparisons are made between the simulated trajectories and the measured data. Comparisons are also made in terms of the calculated torques and the cost.

CHAPTER 2
DYNAMICS OF HUMAN HEAD AND EYE ROTATIONS UNDER DONDERS' CONSTRAINT

Abstract: Rotation of human head and the eye are modeled as a perfect sphere with the rotation actuated by external torques. For the head movement, the axis of rotation is constrained by a law proposed in the 19^{th} century by Donders. For the saccadic eye movement, Donders' Law is restricted to a law that goes by the name of Listing's Law. In this paper, head movement and saccadic eye movement are modeled using principles from Classical Mechanics and the associated Euler Lagrange's equations (EL) are analyzed. Geodesic curves are obtained in the space of allowed orientations for the Head and the Eye and projections of these curves on the space S^2 of pointing directions of the eye/head are shown. A potential function and a damping term has been added to the Geodesic dynamics from EL and the resulting head and eye trajectories settle down smoothly towards the unique point of minimum potential. The minimum point can be altered to regulate the end point of the trajectories (potential control). Throughout the paper, the restricted dynamics of the eye and the head movement have been compared with the unrestricted rotational dynamics on SO(3) and the corresponding EL equations have been analyzed. A version of the Donders' Theorem, on the possible head orientations for a specific head direction, has been stated and proved in appendix 1. In the case of eye movement, Donders' Theorem restricts to the well known Listing's Theorem. In appendix 2, a constraint on the angular velocity and the angular acceleration vectors is derived for the head movement satisfying Donders' constraint. A statement of this constraint that goes by the name 'half angle rule,' has been derived.

$$\begin{pmatrix} \cos^2\frac{\phi}{2} - \sin^2\frac{\phi}{2}(1 - 2\cos^2\alpha\cos^2\theta) & \sin^2\frac{\phi}{2}\cos^2\alpha\sin(2\theta) - \sin\phi\sin\alpha & \sin^2\frac{\phi}{2}\sin(2\alpha)\cos\theta + \sin\phi\cos\alpha\sin\theta \\ \sin^2\frac{\phi}{2}\cos^2\alpha\sin(2\theta) + \sin\phi\sin\alpha & \cos^2\frac{\phi}{2} - \sin^2\frac{\phi}{2}(1 - 2\cos^2\alpha\sin^2\theta) & \sin^2\frac{\phi}{2}\sin(2\alpha)\sin\theta - \sin\phi\cos\alpha\cos\theta \\ \sin^2\frac{\phi}{2}\sin(2\alpha)\cos\theta - \sin\phi\cos\alpha\sin\theta & \sin^2\frac{\phi}{2}\sin(2\alpha)\sin\theta + \sin\phi\cos\alpha\cos\theta & \cos^2\frac{\phi}{2} - \sin^2\frac{\phi}{2}\cos(2\alpha) \end{pmatrix} \tag{2.1}$$

2.1 Introduction

Modeling the dynamics of the eye and the head have been the research goals among neurologists, physiologists and engineers since 1845. Notable studies were conducted by Listing [35], Donders [16] and Helmholtz [59] and they claimed that the orientations of the eye and the head are completely determined as a function of the gaze and the heading directions, respectively. With the exception of occasional deviation, the eye follows what is known as the **Listing's Law** and likewise the head follows a generalization of the Listing's Law that goes by the name **Donders' Law.**

Eye movement and subsequently the head movement problem had found a renewed interest towards the later part of the 20^{th} century [36], [45], [46] and [53]. Initially, the implementation of Listing's Law had been the primary focus of interest [56], [57], [30], [31], [55], [29]. In spite of several notable modeling studies on Three Dimensional Eye and Head Movements (see [5], [24] and [14] for a detailed review), there has not been a rigorous treatment of the Three Dimensional Head Movement Problem, in the framework of mechanical control system and classical mechanics [1], [9], [40]. In this paper, we continue to extend the approach of 'Geometric Mechanics' presented in [43] to the dynamics of the head movement problems. Our motivation to study this problem is twofold. From the point of view of Biomechanics, we would like to understand how eye and head are controlled and coordinated while following the underlying Listing's and Donders' Laws. Our eventual goal is to focus on the combination of cost functions that are minimized while controlling gaze. Our second motivation is to control robotic head/eye (see Cannata [11]) that would follow these underlying principals. Understanding the principals of head/eye coordination would eventually help us build robotic head/eye that are human-like.

Most of the earlier studies in eye movement have assumed that the head remained fixed and the eye is allowed to move freely. It has been observed by Listing (see [57]), that in this situation the orientation of the eye is completely determined by its gaze direction. Under Listing's constraint, starting from a frontal gaze, any other gaze direction is obtained by a rotation matrix whose axis of rotation is constrained to lie on a plane, called the Listing's Plane. Consequently, the set of all orientations the eye can assume is a submanifold of $\mathbf{SO}(3)$ (see Boothby [6] for a definition) called **LIST**. Listing has shown that in a head fixed environment, eye orientations are restricted to

this specific submanifold **LIST** (see [43], [23]).

We study the dynamics, as the head moves spontaneously towards an object following a Listing like constraint that goes by the name Donders' constraint [36], [45] and [53]. Donders' law states that starting from a frontal head position, any other head orientation is obtained by a rotation matrix whose axis of rotation is constrained to lie on a two dimensional surface, called the Donders' Surface [53]. Consequently, the set of all orientations the head can assume spontaneously is a submanifold of $\mathbf{SO}(3)$ called **DOND**. Intuitively, Donders' surface is obtained by mildly perturbing the Listing's Plane along the torsional direction.

In a head free environment, the 'axis of eye rotation' often jumps out of the Listing's plane during a saccade. We consider the 'head free' case by introducing dynamics of eye-movement on the unconstrained orientation space $\mathbf{SO(3)}$. Even in this case, the orientation of the eye satisfies Listing's law, at the beginning and at the end point of a saccade.

The organization of this paper is as follows. In section 2.2 we introduce unit quaternions and motivate the operation of rotation using multiplication by unit quaternions (see [2], [34]). In section 2.3 Donders' constraint is parameterized (following Tweed [55]) and we observe that Listing's constraint can be recovered as a special case of this parametrization. The spaces **LIST** and **DOND** are defined as a submanifold of $\mathbf{SO(3)}$. We state and prove **Listing's Theorem** which asserts that for all but one specific gaze direction (viz. the backward gaze direction), orientation of the eye is completely specified by the gaze direction. In section 2.4 we introduce a Riemannian Metric for the associated spaces **LIST**, **DOND** and $\mathbf{SO(3)}$ and write down the associated geodesic equations. In section 2.5, we define a Lagrangian using the Riemannian Metric in section 2.4 and a suitable Potential Energy term, and write down the corresponding Euler Lagrange Equations (EL). We also add an external 'generalized torque' as inputs to the EL equations and this way we obtain a controlled dynamical system. In section 2.6, we illustrate the obtained geodesic equations and the controlled dynamical system equations by a set of simulations. In these simulations, the control is either set to zero (see Fig. 2.4) or chosen to simulate an appropriate damping (see Figs. 2.5 and 2.6). The control system is regulated by an appropriate choice of a Potential Energy term. Finally section 2.7 concludes the pa-

per. In Appendix I, we state and prove the **Donders' Theorem** for head movement which generalizes Listing's Theorem (see section 2.3) for eye movement. In Appendix II, we state and prove the half angle rule under Donders' constraint which generalizes the half angle rule for Listing's constraint. The half angle rule describes constraints on the angular velocity vectors and angular acceleration vectors, when the motion dynamics satisfy Listing's and Donders' laws.

2.2 Quaternionic Representations

Representation of 'eye orientations' using the quaternions has already been described in [43]. Likewise, the head orientations can also be described using quaternions. In order to set up the notation, we revisit some of the main ideas in this section. A quaternion is a four tuple of real numbers denoted by Q. The space of unit quaternion is identified with the unit sphere in $\mathbb{R}^4$ and denoted by S^3. Each $q \in S^3$ can be written as

$$q = \cos\frac{\phi}{2}\, 1 + \sin\frac{\phi}{2}\, n_1\, i + \sin\frac{\phi}{2}\, n_2\, j + \sin\frac{\phi}{2}\, n_3\, k, \tag{2.2}$$

where $\phi \in [0, 2\pi]$, and $n = (n_1, n_2, n_3)$ is a unit vector in $\mathbb{R}^3$. If q is an unit quaternion represented as in (2.2), using simple properties of quaternion multiplication, one can show the following ([2], [34]):

"The vector $vec[q \bullet (v_1\, i + v_2\, j + v_3\, k) \bullet q^{-1}]$ **is rotation of the vector** (v_1, v_2, v_3) **around the axis** n **by a counterclockwise angle** ϕ**."** The operator $vec[q]$ is defined to be the vector part of q and corresponds to the coefficients associated with i, j and k in (2.2).

To every unit quaternion in S^3, there corresponds a rotation matrix in $SO(3)$ (already introduced in [43]) and the correspondence is described by the map

$$rot : S^3 \to SO(3). \tag{2.3}$$

Note that the map 'rot' in (2.3) is surjective but not $1-1$. This is because both q and $-q$ in S^3 has the same image. We now write down a parametrization of the unit

vector 'n' in (2.2) as

$$n \;=\; (\cos\theta\ \cos\alpha \qquad \sin\theta\ \cos\alpha \qquad \sin\alpha)\,. \tag{2.4}$$

Combining (2.2) and (2.4), we have the following parametrization of unit quaternions

$$q \;=\; \left(\cos\frac{\phi}{2} \qquad \sin\frac{\phi}{2}\cos\theta\ \cos\alpha \qquad \sin\frac{\phi}{2}\sin\theta\ \cos\alpha \qquad \sin\frac{\phi}{2}\sin\alpha\right). \tag{2.5}$$

Using the coordinates (θ, ϕ, α) we have the following sequence of maps

$$[0,\pi] \;\times\; [0,2\pi] \;\times\; [-\frac{\pi}{2},\frac{\pi}{2}] \;\stackrel{\rho}{\longrightarrow}\; S^3 \;\stackrel{rot}{\longrightarrow}\; SO(3) \;\stackrel{proj}{\longrightarrow}\; S^2, \tag{2.6}$$

where $\rho((\theta,\phi,\alpha)) \;=\; q$ (in (2.5)), $rot(q) \;=\; W$ and

$$proj(W) \;=\; \begin{pmatrix} \sin\theta\ \sin\phi\ \cos\alpha \;+\; \cos\theta\ \sin^2\frac{\phi}{2}\ \sin 2\alpha \\ -\cos\theta\ \sin\phi\ \cos\alpha \;+\; \sin\theta\ \sin^2\frac{\phi}{2}\ \sin 2\alpha \\ \cos^2\frac{\phi}{2} \;-\; \sin^2\frac{\phi}{2}\ \cos 2\alpha \end{pmatrix}. \tag{2.7}$$

The matrix W in $SO(3)$ can be easily written from [43], and has been described in (2.1). The points in S^2 described by (2.7) provide a parameterization of the head (gaze) directions as a function of the coordinate angles θ, ϕ, α with respect to an initial head (gaze) direction of $(0,0,1)^T$, i.e. obtained by rotating the vector $(0,0,1)^T$ using the rotation matrix W.

2.3 Orientations Satisfying Donders' Constraint

Donders' law asserts that the axis of rotation 'n' in (2.4) is restricted to a surface. We shall describe this surface by restricting

$$\alpha \;=\; \epsilon\ \sin(2\theta) \tag{2.8}$$

and obtain the axis of rotation as

$$n \;=\; (\cos\theta\ \cos(\epsilon\ \sin(2\theta)),\ \sin\theta\ \cos(\epsilon\ \sin(2\theta)),\ \sin(\epsilon\ \sin(2\theta)))^T. \tag{2.9}$$

The parameter ϵ is assumed to be a small positive or negative constant. The choice of (2.8) as a description of the Donders' surface is dictated by the following observation made in [55] about head movement.

"When the axis of rotation is horizontal or vertical (i.e. when θ is a multiple of $\frac{\pi}{2}$), head moves without any torsion. At other angles of rotation, there is a gradual increase in torsion".

Note that the axis of rotation vector n lies on a surface given by

$$2\epsilon\, x\, y \;=\; \sin^{-1} z\,(1-z^2), \tag{2.10}$$

where (x, y, z) are the three coordinates of the axis of rotation given by $x \;=\; \cos\theta\;\cos\alpha,\; y \;=\; \sin\theta\;\cos\alpha,\; z \;=\; \sin\alpha$. The coordinate z is constrained by $|z| \;\leq\; |\sin\epsilon|$.

The Donders' law (2.8) constrains the rotation matrices W parameterized in (2.1). We define **DOND** to be the associated submanifold of $\mathbf{S}^3$ and $\mathbf{SO}_D(3)$ to be the associated submanifold of **SO(3)**. They are both two dimensional submanifolds parameterizing all possible rotations in $\mathbf{S}^3$ and $\mathbf{SO}(3)$ respectively that satisfy Donders' constraint (2.8). The heading direction $(0,\; 0,\; 1)^T$ is transformed to the direction

$$\begin{pmatrix} \sin\theta\;\sin\phi\;\cos(\epsilon\sin(2\theta)) \;+\; \cos\theta\;\sin^2\frac{\phi}{2}\;\sin(2\epsilon\sin(2\theta)) \\ -\cos\theta\;\sin\phi\;\cos(\epsilon\sin(2\theta)) \;+\; \sin\theta\;\sin^2\frac{\phi}{2}\;\sin(2\epsilon\sin(2\theta)) \\ \cos^2\frac{\phi}{2} \;-\; \sin^2\frac{\phi}{2}\;\cos(2\epsilon\sin(2\theta)) \end{pmatrix},$$

by the rotation matrix (2.1). Thus we obtain from (2.6) the following sequence of maps

$$[0, 2\pi] \;\times\; [0, 2\pi] \;\xrightarrow{\rho}\; \mathbf{DOND} \;\xrightarrow{rot}\; \mathbf{SO}_D(3) \;\xrightarrow{proj}\; \mathbf{S}^2, \tag{2.11}$$

where α has been restricted by the Donders' constraint (2.8). Note that the variable θ in (2.11) is restricted to the interval $[0, 2\pi]$, whereas in (2.6) it is restricted to $[0, \pi]$. This is because the images of (θ, ϕ, α) and $(\theta+\pi, -\phi, -\alpha)$ are the same under the map ρ in (2.6). Hence the domain of θ is chosen to be $[0, \pi]$ in (2.6). The points (θ, ϕ, α) and $(\theta+\pi, -\phi, -\alpha)$ cannot both satisfy the Donders' constraint unless $\epsilon \;=\; 0$. Hence

in (2.11) the domain has to be enlarged.

Listing's constraint is recovered from Donders' constraint by restricting ϵ to zero. Listing's law asserts that the axis of rotation 'n' defined in (2.4), is restricted to a plane, called the Listing's Plane. We shall describe this plane by restricting $\alpha = 0$ and obtain $n = (\cos\theta,\ \sin\theta,\ 0)^T$, $q = (\cos\frac{\phi}{2},\ \sin\frac{\phi}{2}\ \cos\theta,\ \sin\frac{\phi}{2}\ \sin\theta,\ 0)^T$ and the matrix W can be obtained from (2.1). Analogous to the Donders' constraint, under the Listing's constraint, we define **LIST** to be the associated submanifold of $\mathbf{S}^3$ and $\mathbf{SO}_L(3)$ to be the associated submanifold of $\mathbf{SO(3)}$. We have the following sequence of maps

$$[0,\pi]\ \times\ [0,2\pi]\ \xrightarrow{\rho}\ \mathbf{LIST}\ \xrightarrow{rot}\ \mathbf{SO}_L(3)\ \xrightarrow{proj}\ \mathbf{S}^2 \tag{2.12}$$

and the following theorem due to Listing.

Theorem 1 (Listing): Under the Listing's constraint, the map

$$\mathbf{SO}_L(3)\ -\ \left\{\begin{pmatrix} \cos 2\theta & \sin 2\theta & 0 \\ \sin 2\theta & -\cos 2\theta & 0 \\ 0 & 0 & -1 \end{pmatrix}\right\}\ \xrightarrow{\mathbf{proj}}\ \mathbf{S}^2\ -\ \left\{\begin{pmatrix} 0 \\ 0 \\ -1 \end{pmatrix}\right\}$$

described by (2.6) and (2.12) is one to one and onto.

Remark: Listing's Theorem 1 asserts that for all but perhaps one gaze direction given by $(0,\ 0,\ -1)^T$, which is opposite to the primary gaze direction $(0,\ 0,\ 1)^T$, every other gaze direction completely specifies the rotation matrix.

Proof of Listing's Theorem 1**:** Note that when $\phi \neq 0$ and $\phi \neq \pi$, it follows that if $\theta = \theta_0, \phi = \phi_0$ satisfies a suitable gaze direction, then $\theta = \theta_0 + \pi, \phi = 2\pi - \phi_0$ would also satisfy the same gaze direction. In the domain $\theta \in [0,\pi]$ and $\phi \in [0,2\pi]$ these are the only two choices for a specific gaze vector. It would follow that when $\phi \neq 0$, $\phi \neq \pi$, $\theta \neq 0$ and $\theta \neq \pi$ then the pair of angles θ, ϕ in the domain that satisfies a suitable gaze direction is unique. Hence these gaze directions correspond to an unique rotation matrix. It can be checked by direct calculations that for the pair $(\theta = 0, \phi = \phi_0)$ and $(\theta = \pi, \phi = -\phi_0)$ the corresponding rotation matrix and the gaze vector are identical. Finally for $\phi = 0$ or $\phi = 2\pi$, and θ is arbitrary, the rotation

matrix is the identity matrix and the gaze direction is the primary gaze direction $(0, 0, 1)^T$. It would follow that the only gaze direction for which the rotation matrix is not unique is when $\phi = \pi$. This would correspond to the gaze direction $(0, 0, -1)^T$, which has been excluded.

(Q.E.D)

Remark: In appendix I, we state and prove a generalization of the Listing's Theorem 1, for the head movement problem. We call this theorem the Donders' Theorem. The upshot of the theorem is that the number of orientations of the head for a specific pointing direction is 'not unique' when the head follows the Donders' Law. For most practical pointing directions of the head, which includes the frontal hemisphere, the number of allowed orientations is two (counting multiplicity). For a simply connected, closed and bounded set **S** of head directions around the 'backward direction' the number of orientations is four (counting multiplicity). When the parameter ϵ, in (2.8) approaches zero, the set **S** degenerates to a point, viz. the backward head direction and we recover the Listing's Theorem from Donders' Theorem. For a specific pointing direction in the frontal hemisphere, the two ambiguous head orientations merge to an unique orientation when ϵ approaches zero. The relative sizes of **S** as a function of ϵ has been illustrated in Fig. 2.9.

2.4 Riemannian Metric on $SO(3)$, DOND and LIST

It has been described in [43] that eye rotations are typically confined to a sub manifold **LIST** of **SO**(3) especially when the head is restrained to be fixed. Likewise, spontaneous head movements are typically confined to a sub manifold **DOND** of **SO**(3). In order to write down the equations of motion, one needs to know the kinetic and the potential energies of the head in motion. The kinetic energy is given by the induced Riemannian metric on **DOND**, induced from the Riemannian metric on **SO**(3).

The Riemannian metric (see [60]) is derived by assuming that the head is a perfect sphere and its inertia tensor is equal to the identity matrix $I_{3\times 3}$. This is associated with a left invariant Riemannian metric on **SO**(3), already described in [43]. An

easy way to carry out computation using this Riemannian metric is provided by the isometric submersion **rot** described in (2.3) and (2.6). In order to compute the Riemannian Metric on $\mathbf{SO}(3)$, we write

$$\rho_*\left(\frac{\partial}{\partial\theta}\right) = \begin{pmatrix} 0 \\ -\sin(\phi/2) & \sin(\theta) & \cos(\alpha) \\ \sin(\phi/2) & \cos(\theta) & \cos(\alpha) \\ 0 \end{pmatrix}, \; \rho_*\left(\frac{\partial}{\partial\alpha}\right) = \begin{pmatrix} 0 \\ -\sin(\phi/2) & \cos(\theta) & \sin(\alpha) \\ -\sin(\phi/2) & \sin(\theta) & \sin(\alpha) \\ \sin(\phi/2) & \cos(\alpha) \end{pmatrix}$$

$$\rho_*\left(\frac{\partial}{\partial\phi}\right) = \begin{pmatrix} -\frac{1}{2}\sin(\phi/2) \\ \frac{1}{2}\cos(\phi/2) & \cos(\theta) & \cos(\alpha) \\ \frac{1}{2}\cos(\phi/2) & \sin(\theta) & \cos(\alpha) \\ \frac{1}{2}\cos(\phi/2) & \sin(\alpha) \end{pmatrix}.$$

Then we obtain the inner products given by,

$$\begin{aligned} g_{11} &= \langle\frac{\partial}{\partial\theta}, \frac{\partial}{\partial\theta}\rangle = \sin^2(\phi/2)\cos^2(\alpha) \\ g_{22} &= \langle\frac{\partial}{\partial\alpha}, \frac{\partial}{\partial\alpha}\rangle = \sin^2(\phi/2) \\ g_{33} &= \langle\frac{\partial}{\partial\phi}, \frac{\partial}{\partial\phi}\rangle = \frac{1}{4} \\ \text{and } g_{ij} &= 0 \text{ for } i \neq j \text{ with } i, j = 1, 2, 3. \end{aligned}$$

The Riemannian metric on $\mathbf{SO}(3)$ is given by:

$$g = \sin^2(\phi/2)\cos^2(\alpha)\, d\theta^2 + \sin^2(\phi/2)\, d\alpha^2 + \frac{1}{4} d\phi^2. \tag{2.13}$$

Note that restricted to the Donders' surface, i.e. when (2.8) is satisfied, the Riemannian metric on **DOND** is given by

$$g = \sin^2(\phi/2)\left[\cos^2\alpha + \left(\frac{\partial\alpha}{\partial\theta}\right)^2\right] d\theta^2 + \frac{1}{4} d\phi^2. \tag{2.14}$$

Using the Riemannian metric (2.13) for $\mathbf{SO}(3)$, the associated geodesic equation is

given by

$$\begin{aligned} \ddot{\theta} + \dot{\theta}\dot{\phi}\cot(\phi/2) - 2\dot{\theta}\dot{\alpha}\tan(\alpha) &= 0 \\ \ddot{\phi} - \left(\dot{\theta}\right)^2 \sin(\phi)\cos^2(\alpha) - (\dot{\alpha})^2 \sin(\phi) &= 0 \\ \ddot{\alpha} + \frac{1}{2}\left(\dot{\theta}\right)^2 \sin(2\alpha) + \dot{\phi}\dot{\alpha}\cot(\phi/2) &= 0. \end{aligned} \tag{2.15}$$

Likewise, using the Riemannian metric (2.14) for **DOND**, the associated geodesic equation is given by

$$\begin{aligned} \frac{d}{dt}\left[\sin^2\frac{\phi}{2}\left(\cos^2\alpha + \left(\frac{\partial\alpha}{\partial\theta}\right)^2\right)\dot{\theta}\right] & \\ - \sin^2\frac{\phi}{2}\,\dot{\theta}^2\,\frac{\partial\alpha}{\partial\theta}\left[\frac{\partial^2\alpha}{\partial\theta^2} - \frac{1}{2}\sin(2\alpha)\right] &= 0 \\ \ddot{\phi} - \left[\cos^2\alpha + \left(\frac{\partial\alpha}{\partial\theta}\right)^2\right]\dot{\theta}^2\,\sin\phi &= 0. \end{aligned} \tag{2.16}$$

Restricted to the Listing's plane, i.e. when $\alpha = 0$, the Riemannian metric on **LIST** is given by

$$g = \sin^2(\phi/2)\,d\theta^2 + \frac{1}{4}d\phi^2 \tag{2.17}$$

and (2.15) reduces to the following pair of equations, already described in [43], given by

$$\ddot{\theta} + \dot{\theta}\dot{\phi}\cot(\phi/2) = 0, \quad \ddot{\phi} - \left(\dot{\theta}\right)^2 \sin(\phi) = 0. \tag{2.18}$$

We now state the following theorem, which demonstrates the geometric structure of the geodesic.

Theorem 2 **(Geodesic curves on SO(3) and $\mathbf{SO}_L(3)$):** The geodesic curves on $\mathbf{SO}(3)$, given by the integral curves of (2.15), projected on $\mathbf{S}^2$ via the mapping 'proj' described in (2.6) are circles. Furthermore, the geodesic curves on $\mathbf{SO}_L(3)$, given by the integral curves of (2.18), projected on $\mathbf{S}^2$ via the mapping 'proj' described in (2.12) are circles which always pass through a fixed vector $(0, 0, -1)^T$.

Proof of the Geodesic Theorem 2: If we define a new angle variable

$$\xi \;=\; \frac{\phi}{2},$$

the parametrization of $\mathbf{S}^3$ described in (2.5) would be given by

$$q \;=\; \Big(\; \cos\xi, \sin\xi\cos\theta\;\cos\alpha,\; \sin\xi\sin\theta\;\cos\alpha,\; \sin\xi\sin\alpha\;\Big). \tag{2.19}$$

Using the angle variables (ξ, θ, α), it is easy to see using the Riemannian metric (2.13) on $\mathbf{S}^3$, that the geodesics are great circles on $\mathbf{S}^3$. What we need to show is that, under the composition map 'proj $\circ$ rot', described by

$$\begin{pmatrix} \delta_0 \\ \delta_1 \\ \delta_2 \\ \delta_3 \end{pmatrix} \longmapsto \begin{pmatrix} 2(\delta_1\delta_3 + \delta_0\delta_2) \\ 2(\delta_2\delta_3 - \delta_0\delta_1) \\ \delta_0^2 + \delta_3^2 - \delta_1^2 - \delta_2^2 \end{pmatrix},$$

'generically the great circles on $\mathbf{S}^3$ are projected as circles on $\mathbf{S}^2$.' We omit the details of the proof but the essential point is that the great circles on $\mathbf{S}^3$ project as planar curves on $\mathbf{S}^2$ and hence generically they are circles (unless the circle degenerates to a point). When the Listing's constraint is satisfied, we have $\alpha \;=\; 0$. The parametrization (2.19) would reduce to

$$q \;=\; \Big(\; \cos\xi,\;\; \sin\xi\cos\theta,\;\; \sin\xi\sin\theta,\;\; 0\;\Big).$$

It would follow that great circles on $\mathbf{S}^3$ are in fact great circles on $\mathbf{S}^2$, where $\mathbf{S}^2$ is parameterized as

$$\Big(\; \cos\xi,\;\; \sin\xi\cos\theta,\;\; \sin\xi\sin\theta\;\Big).$$

Since, every great circle on $\mathbf{S}^2$ passes through the point $\xi = \frac{\pi}{2}$, the circle on the gaze space $\mathbf{S}^2$ passes through the point $\phi = \pi$. The gaze corresponding to the point $\phi = \pi$ is precisely $(0, 0, -1)$.

(Q.E.D)

Remark: If we make the convention that the gaze direction vector $(0, 0, 1)^T$ is the frontal gaze direction, it would follow that the vector $(0, 0, -1)^T$ is the backward gaze direction. Listing's Theorem 1 would then assert that for all gazes other than the backward gaze, orientation of the eye, restricted to the Listing's submanifold of $\mathbf{SO}(3)$, is completely specified by the gaze. It may be inferred from the above geodesic Theorem 2 that the projections of the geodesic curves on the gaze space, $\mathbf{S}^2$, are circles that always pass through the backward gaze direction.

Remark: Geodesic curves on $\mathbf{SO}_D(3)$ are in general not periodic and does not appear to have a regular geometric shape. When the initial condition on $\dot{\theta}$ is assumed to be 0, the projection of the integral curves of (2.16) on $\mathbf{S}^2$ are circles (shown in Fig. 2.3). Interestingly, these circles always pass through the frontal pointing direction.

2.5 General Equation of Motion on $SO(3)$ and its Two Submanifolds

The Riemannian Metric that we have obtained in (2.14) enables us to write down an expression for the kinetic energy KE given by

$$KE \;=\; \frac{1}{2}[\sin^2(\phi/2)\,[\cos^2\alpha \;+\; (\frac{\partial\alpha}{\partial\theta})^2]\dot{\theta}^2 + \frac{1}{4}\dot{\phi}^2]. \tag{2.20}$$

Remark: In writing the expression (2.20) for kinetic energy, we need to assume that the moment of inertia matrix is an identity matrix, as would be the case if the eye/head is a perfect sphere and all rotations are about its center.

In general, the dynamics is affected by an additional potential energy and an external input torque. Let us consider a general form of the potential function given by

$$V(\theta, \phi) \;=\; A\,\sin^2\frac{\phi - \phi_0}{2} \;+\; B\,\sin^2\frac{\theta - \theta_0}{2}, \tag{2.21}$$

which attains a minimum value at a specific pointing direction (θ_0, ϕ_0).

Remark: Human eye and head orientations have a natural domain and they are not allowed to move outside this domain. In an uncontrolled system, one way to implement this would be to include a potential term V to the Lagrangian, with the property that the potential function is large at points that are disallowed. Our choice

of the term (2.21) is arbitrary, except that it vanishes at $(\theta_0,\ \phi_0)$ and takes large values when the eye and the head are pointed backwards. An interesting question that we have not answered in this paper is "Does there exist a potential function that would match observed human eye and head movements?"

The expression for the Lagrangian is given by $L\ =\ KE\ -\ V$, and the equation of motion is described by

$$\frac{d}{dt}\left(\frac{\partial L}{\partial \dot{\beta}}\right)\ -\ \left(\frac{\partial L}{\partial \beta}\right)\ =\ \tau_\beta,$$

where β is the angle variable. Assuming $\phi_0\ =\ \theta_0\ =\ 0$ in (2.21), the Euler Lagrange's equation on **DOND** is given by

$$\begin{aligned}\frac{d}{dt}\left[\sin^2\frac{\phi}{2}\left(\cos^2\alpha+\left(\frac{\partial\alpha}{\partial\theta}\right)^2\right)\dot{\theta}\right]\ -\ \sin^2\frac{\phi}{2}\,\dot{\theta}^2\,\frac{\partial\alpha}{\partial\theta}\,\left[\frac{\partial^2\alpha}{\partial\theta^2}\ -\ \frac{1}{2}\,\sin(2\alpha)\right]&\\ =\ -\frac{1}{2}\,B\,\sin\theta\ +\ \tau_\theta,&\\ \ddot{\phi}\ -\ \left[\cos^2\alpha\ +\ \left(\frac{\partial\alpha}{\partial\theta}\right)^2\right]\dot{\theta}^2\ \sin\phi = -\ 2A\sin\phi\ +\ 4\ \tau_\phi,&\end{aligned}$$

where, as in section 2.3, we continue to assume that α satisfies the Donders' constraint (2.8). In order to describe (2.22) in a compact notation, we define the following set of variables:

$$\begin{aligned}&\alpha(\theta)\ =\ \epsilon\ \sin(2\theta),\ \nu(\theta)\ =\ \epsilon\ \cos(2\theta),\\ &\sigma(\theta,\phi)\ =\ \sin^2\frac{\phi}{2}\ \left[\cos^2\alpha\ +\ 4\nu^2\right].\end{aligned}\tag{2.22}$$

We also define

$$\Lambda(\theta)\ =\ \frac{\nu(8\alpha\ +\ \sin(2\alpha))}{\cos^2\alpha\ +\ 4\nu^2},$$

and rewrite (2.22) as follows:

$$\begin{aligned}\ddot{\theta}\ &=\ -\frac{\dot{\sigma}}{\sigma}\,\dot{\theta}\ -\ \Lambda(\theta)\,\dot{\theta}^2\ -\ \frac{B}{2\sigma}\ \sin\theta\ +\ \frac{1}{\sigma}\,\tau_\theta\\ \ddot{\phi}\ &=\ (\cos^2\alpha\ +\ 4\nu^2)\ \sin\phi\,\dot{\theta}^2\ -\ 2A\sin\phi\ +\ 4\tau_\phi,\end{aligned}\tag{2.23}$$

where

$$\dot{\sigma} \;=\; \frac{d}{dt}\left[\sigma(\theta,\phi)\right].$$

In order to write (2.23) using state variables, we write

$$z_1 \;=\; \theta,\; z_2 \;=\; \dot{\theta},\; z_3 \;=\; \phi,\; z_4 \;=\; \dot{\phi},$$

and the corresponding state variable equation on **DOND** is given by

$$\begin{aligned}
\dot{z}_1 \;&=\; z_2 \\
\dot{z}_2 \;&=\; -\frac{\dot{\sigma}}{\sigma}\, z_2 \;-\; \Lambda(z_1)\, z_2^2 \;-\; \frac{B}{2\sigma}\, \sin(z_1) \;+\; \frac{1}{\sigma}\, \tau_\theta \\
\dot{z}_3 \;&=\; z_4 \\
\dot{z}_4 \;&=\; (\cos^2\alpha \;+\; 4\nu^2)\,(\sin z_3)\, z_2^2 \;-\; 2\,A\, \sin(z_3) \;+\; 4\tau_\phi,
\end{aligned} \tag{2.24}$$

where $\alpha(z_1)$, $\nu(z_1)$ and $\sigma(z_1, z_3)$ can be defined from (2.22) and where the details of $\dot{\sigma}$ has been omitted.

Remark: The underlying control system that governs head movement satisfying Donder's constraint is given by (2.24). τ_θ and τ_ϕ are generalized torques that are generated by neck muscle forces acting on the head. For the eye movement problem, muscle forces generating these torques were modeled in [43]. For the head movement problem, modeling the muscle generated forces of the neck muscles, is a subject of future research.

The state variable equation on **LIST** can be obtained by considering $\alpha \;=\; 0$ and the Riemannian Metric given by (2.17). Assuming $\phi_0 \;=\; \theta_0 \;=\; 0$ in (2.21), the Euler Lagrange's Equation on **LIST** is given by

$$\begin{aligned}
\ddot{\theta} + \dot{\theta}\dot{\phi}\cot(\phi/2) \;+\; \frac{B}{2}\, \csc^2(\phi/2)\, \sin(\theta) \;&=\; \csc^2(\phi/2)\, \tau_\theta \\
\ddot{\phi} - \left(\dot{\theta}\right)^2 \sin(\phi) \;+\; 2\mathrm{A}\sin(\phi) \;&=\; 4\tau_\phi.
\end{aligned} \tag{2.25}$$

The state variable equation on **SO(3)** can be obtained by considering the Riemannian Metric given by (2.13). These have not been written down in this paper, since we do not study control of motion dynamics on **SO(3)**.

2.6 Simulations on Geodesic and Control Using Potential Function

In this section, our first goal is to show, using simulation, the shape of the geodesic trajectories on $\mathbf{SO}_L(3)$, $\mathbf{SO(3)}$ and $\mathbf{SO}_D(3)$. To display the shape, we plot the projection of the trajectories on $\mathbf{S}^2$.

2.6.1 Geodesic Trajectories

Example 1.1 (Geodesic curves for eye movement satisfying Listing): In this example we solve (2.18) (corresponds to eye rotation that satisfy the Listing's constraint). In Fig. 2.1 we have plotted the eye directions as a function of time starting from one suitably chosen initial condition. In plotting the figure, we have chosen the convention that the identity rotation matrix corresponds to the frontal gaze. Our simulation shows that the projection of the geodesic curve on the gaze space $\mathbf{S}^2$ is a circle that always passes through the backward gaze direction.

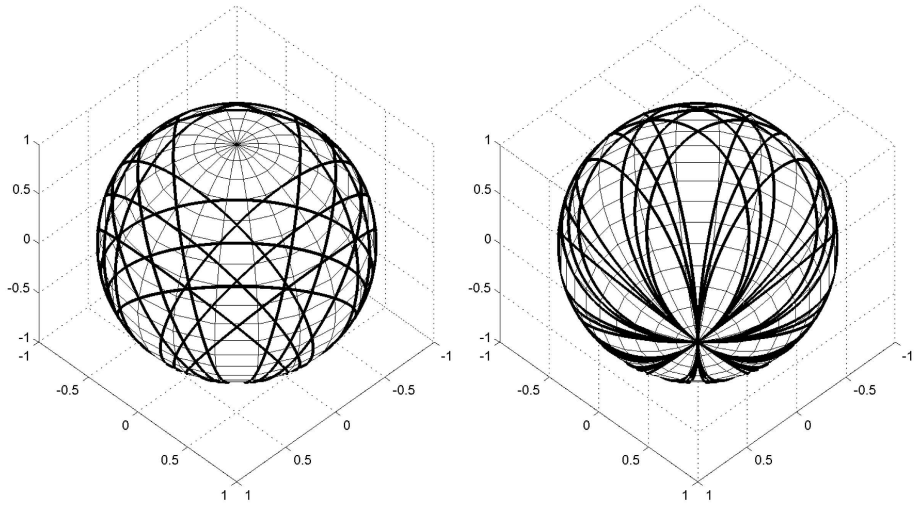

(a) Front (b) Back

Figure 2.1: Projection of the geodesic curves from (2.18) on **LIST** plotted on the gaze space $\mathbf{S}^2$. The left figure shows the north pole which is the frontal gaze direction. The right figure shows the south pole which is the backward gaze direction. The projections are circular passing through the backward gaze.

Example 1.2 (Geodesic curves for eye movement not satisfying Listing): In this example we solve (2.15) (corresponds to eye rotation that does not satisfy the

Listing's constraint). We show in Fig. 2.2 that the projection of the geodesic curves on the gaze space are circles that do not necessarily pass through a fixed point. Fig. 2.2a and Fig. 2.2b are two cases of the simulation assuming different initial conditions for $\dot{\alpha}$. Each figure consists of curves with different initial choices of θ and ϕ.

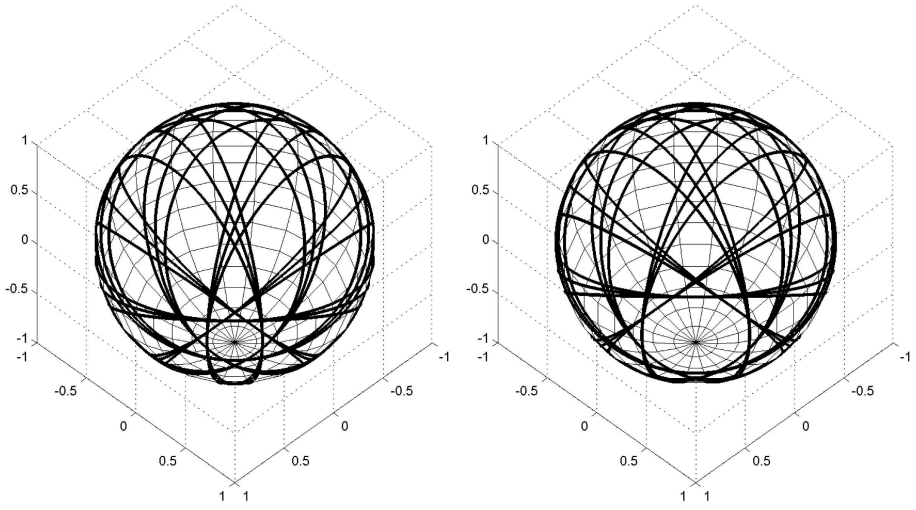

(a) (b)

Figure 2.2: Projection of the geodesic curves from (2.15) on **SO(3)** plotted on the gaze space $\mathbf{S}^2$. Both the left and the right figure show the south pole which is the backward gaze direction. As opposed to what we found in Fig. 2.1, each projection is a circle that do not pass through one fixed gaze and in particular through the backward gaze.

Remark: We have seen in Theorem 2 of section 2.3, that the geodesics on $\mathbf{SO}_L(3)$ and **SO(3)** are projections of great circles on $\mathbf{S}^3$. Their projections on the gaze space $\mathbf{S}^2$ are also circles that are plotted in Figs. 2.1 and 2.2.

Example 1.3 (Geodesic curves for head movement satisfying Donders): In this example, we solve (2.16) (corresponds to head rotation that satisfy the Donders' constraint). We assume that the initial condition on $\dot{\theta}$ is 0. In Fig. 2.3, we have plotted the pointing directions of the head as a function of time, starting from one suitably chosen initial head position, viz. 'pointing straight with no tilt.' The plot in Fig. 2.3 is shown for three different initial conditions on θ. The trajectories

obtained in Fig. 2.3 are circles passing through the frontal pointing direction. For initial conditions on θ equals 0 or $\frac{\pi}{2}$, the axis of rotation is on the Listing's plane and the head rotates without any torsion, shown in Figs. 2.3a, 2.3b, 2.3c, 2.3d. For other initial conditions, viz. $\theta = \frac{\pi}{3}$, the axis has torsional component provided by the Donder's Law (2.8), shown in Figs. 2.3e, 2.3f. In this simulation, ϵ is chosen as 0.5.

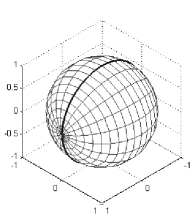

(a) Head trajectory when $\theta = 0$.

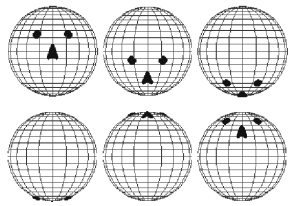

(b) For $\theta = 0$, head moves top to bottom without any torsion.

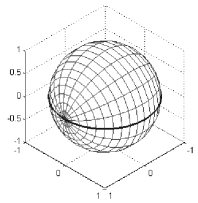

(c) Head trajectory when $\theta = \frac{\pi}{2}$.

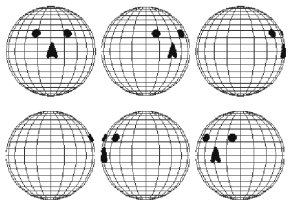

(d) For $\theta = \frac{\pi}{2}$ head moves right to left without any torsion.

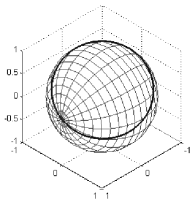

(e) Head trajectory when $\theta = \frac{\pi}{3}$.

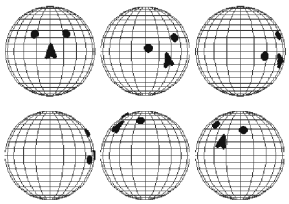

(f) For $\theta = \frac{\pi}{3}$ head moves left/bottom to right/up with torsion.

Figure 2.3: Projection of the geodesic curves (2.16) on **DOND** plotted on the space $\mathbf{S}^2$ of pointing directions of the head. When the initial condition on $\dot{\theta}$ is zero, the axis of rotation does not change along the integral curves of (2.16) on **DOND**. For different initial conditions on θ the pointing directions of the head rotate in a circle.

Our next goal is to show that by tuning the parameters ϕ_0 and θ_0 in (2.21), we can drive the eye or the head to a suitable end position and orientation. This has been illustrated in the next three examples.

2.6.2 Eye/Head trajectories with a potential function

The purpose of this subsection is to demonstrate via simulation that by adding a potential term, one is able to push the trajectories of the eye or head toward the frontal gaze direction.

Example 2.1 (Eye motion with a Potential Function but no Damping): In this example we solve (2.25) on **LIST** and display the gaze trajectories in Fig. 2.4. We have assumed $\tau_\theta = \tau_\phi = 0$, $\theta_0 = \phi_0 = 0$ and $B = 0$ in (2.21). Increasing magnitudes of A has been chosen in Figs. 2.4a, 2.4b, 2.4c, 2.4d. Our simulations show that with increasing magnitude of the potential function, the gaze trajectories are restricted to a smaller neighborhood of the frontal gaze. However, the trajectories are oscillatory.

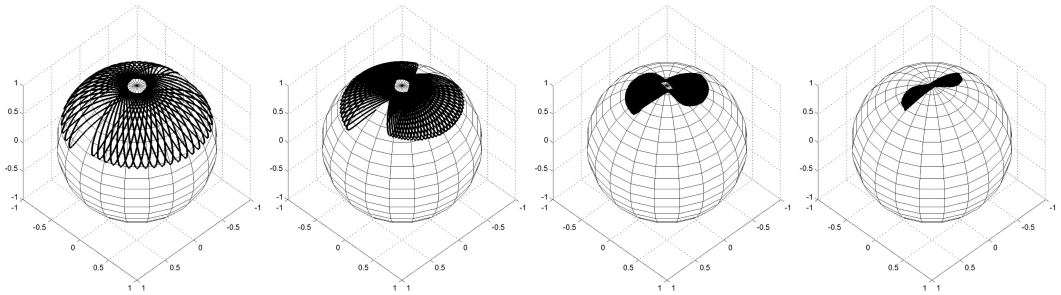

(a) A = 0.5 (b) A = 1 (c) A = 5 (d) A = 50

Figure 2.4: Gaze motion from (2.25) for increasing values of the parameter A, with the external control set to zero, i.e. $\tau_\theta = \tau_\phi = 0$, and the motion is purely due to the potential function (2.21), which has a minimum at the frontal gaze.

We now proceed to add a damping term to the motion equations.

Example 2.2 (Eye regulation toward frontal gaze direction using a Potential Function and Damping): We repeat Example 2.1 but choose $\tau_\theta = -.1\ \dot{\theta}$ and $\tau_\phi = -.1\ \dot{\phi}$ in (2.25), in order to dampen the fluctuations in the trajectories. The results are plotted in Fig. 2.5. We observe that the state settles down to the point of minimum potential, the frontal gaze.

Remark: Eye and Head movements are damped in real system, through the actuating muscles. While modeling muscles, such as in [32] (see also [63]), a passive damping term is added to the model, which in turn damps the movement. In this paper we have not modeled damping of the real system, but introduced a damping term to study the effect of damping on the trajectories.

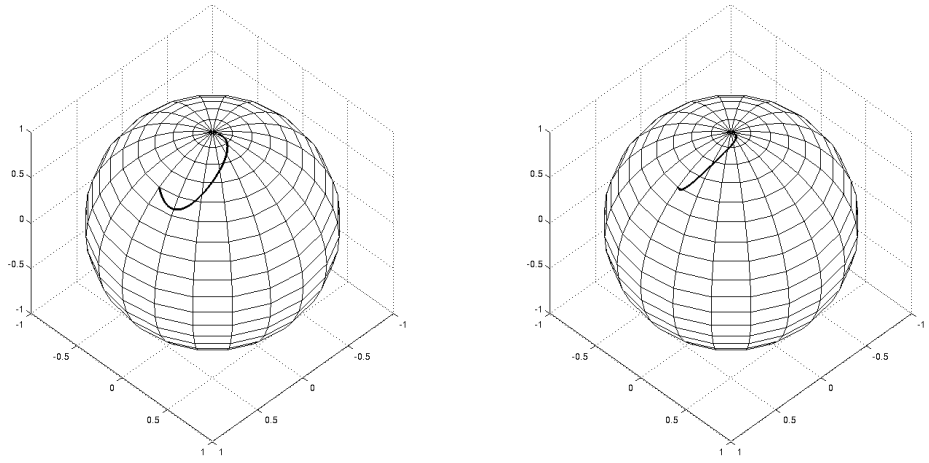

(a) A = 5 (b) A = 50

Figure 2.5: Gaze motion under the influence of a potential function and a constant damping term using (2.25) with $\tau_\theta = -k\,\dot{\theta}$ and $\tau_\phi = -k\,\dot{\phi}$. The value of k is chosen to be 0.1.

Example 2.3 (Head regulation toward an arbitrary heading direction with two distinct orientations): In this example we have two head trajectories going to the same pointing direction but with two distinct orientations while satisfying the Donders' constraint. Possibility of two orientations for a given pointing direction is prescribed by the Donders' Theorem 3 in Appendix I. We have used the potential function (2.21) with $A = B = 1$ and $\tau_\theta = -1\,\dot{\theta}$ and $\tau_\phi = -1\,\dot{\phi}$. The parameters $\theta_0 = 5.5528$, $\phi_0 = -0.8026$ is chosen for the top trajectory in Fig. 2.6a and $\theta_0 = 2.3012$, $\phi_0 = 0.8026$ is chosen for the bottom trajectory in Fig. 2.6a. The value of ϵ for the Donders' constraint is chosen as -0.1309. Fig. 2.6a show the head direction trajectories for the two paths. Fig. 2.6b shows the actual head orientations at initial, final and some intermediate points.

2.6.3 Effect of Donders' torsional component on Head Movement

Example 3 (How does the parameter ϵ affect TIME and DISTANCE?): In Fig. 2.7, we have sketched the head movements between two specific directions, that are kept fixed for this example. In Fig. 2.7a, head movements are shown for

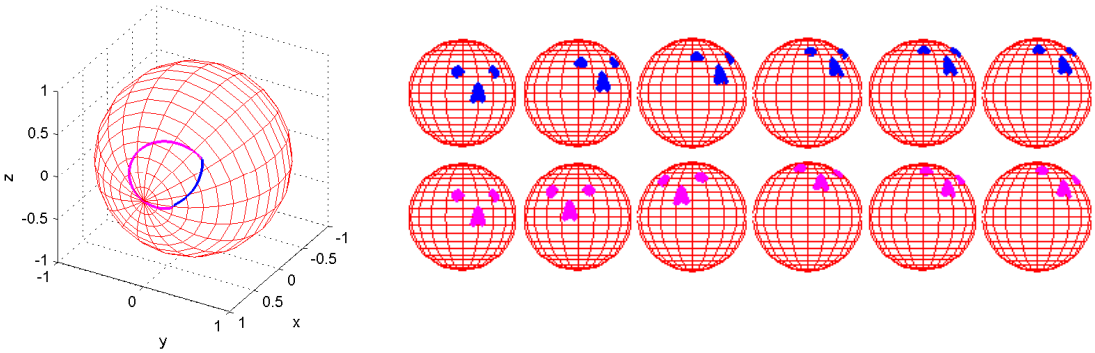

(a) Two trajectories of head movement from A to B

(b) Head orientations are shown for two trajectories. The top sequence is for the bottom trajectory in Fig. 2.6a. The bottom sequence is for the top trajectory in Fig. 2.6a.

Figure 2.6: Trajectories of the pointing directions with same initial head orientation and final head pointing direction. However, the final head orientations for the two trajectories are different.

different values of ϵ in the Donders' constraint (2.8). The values of A, B in (2.21) are chosen to be 1. We choose $\tau_\theta = -1\ \dot{\theta}$ and $\tau_\phi = -1\ \dot{\phi}$. Although the paths appear to follow similar profile, in Fig. 2.7b, we show that the total distance, computed using the Riemannian metric (2.14), increases with increasing values of ϵ. This is understandable since there is an extra head rotation for the same head direction. We also make a surprising observation in Fig. 2.7b that the time to complete the trajectories fall, as a function of ϵ, indicating that perhaps *with higher levels of torsion, provided by increasing ϵ, the head is able to move rapidly a larger distance in a shorter time.*

2.7 Conclusion

In this paper we study the problem of modeling the rotation of human head, when the head shifts its orientation between two pointing directions, as a simple mechanical system. The human eye is a special case of this class of problem. Head movements obey Donders' constraint (a generalization of the Listing's constraint for eye movement), which states that the allowed orientations of the head are obtained by rotating a fixed 'primary heading direction' by a subclass of rotation matrices. These rotation matrices have their axes of rotation restricted to a fixed surface, called the Donders' surface. Defining a suitable Riemannian metric, we obtain dynamic model of head

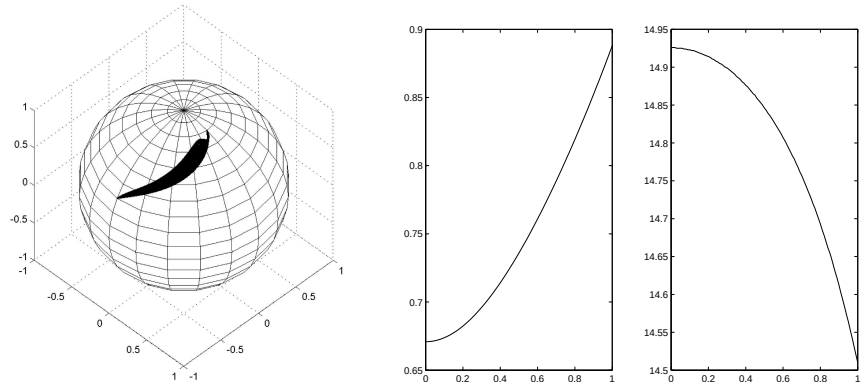

(a) Trajectories of the head direction as ϵ varies from 0 to 1.

(b) (Left) Distance as a function of ϵ. (Right) Time as a function of ϵ

Figure 2.7: For increasing values of ϵ, the head moves a longer distance in a shorter time.

movement when the head orientations satisfy the Donders' constraint throughout its entire trajectory. Head movements are actuated by choosing a suitable potential function and the oscillations are damped by adding a suitable damping term. A similar study for the eye movement is reported in this paper assuming that the eye moves while Listing's constraint is always satisfied. For the head movement, an important result of this paper is to show the effect of the torsional component ϵ as head is allowed to move between two 'pointing directions'.

Among somewhat more theoretical results, we generalize the well known Listing's Theorem 1 which states that for all gaze directions, 'other than one specific backward gaze', the orientation of the eye is a fixed function of gaze. For the head movement problem, a corresponding Donders' Theorem has been stated and proved in appendix I. The Donders' theorem states that for all pointing directions of the head 'other than a closed and bounded region **S**' that contains the backward head direction, the orientation of the head for a specific 'head direction' is ambiguous up to two alternative orientations (shown in Appendix I). Additionally – "within the closed and bounded region **S**, the orientations of the head for a specific gaze direction is not unique but can have up to four distinct choices." A sketch of the set **S** for different values of ϵ has been shown in Fig. 2.9. Finally, in Appendix II, we obtain a suitable generalization of the half angle rule for head movement satisfying the Donders' constraint.

Research presented in this paper can be extended along the following three areas. Alternative forms of the potential function (22), chosen somewhat arbitrarily in this paper, can be explored to match recorded data from eye/head movement trajectories. Using τ_θ and τ_ϕ as the control variables for the dynamical system (25) describing head movements, one can solve minimum energy and minimum time optimal control problems. Finally, the same dynamical system (25) can also be used to study tracking problems, especially to track trajectories of recorded eye and head movement data.

2.8 Appendix I: Donders' Theorem

The question we ask in this appendix is the following:

Given a specific head direction, how many orientations of the head are allowed while satisfying the Donders' constraint? Equivalently, **For the map (2.11), how many pre-images does 'proj' have?**

We now discuss this question as follows:

For a specific pointing direction $(a, b, c)^T$, where $a^2+b^2+c^2 = 1$, what are the possible values of θ and ϕ that will solve the set of equations

$$\begin{aligned} \sin\theta\ \sin\phi\ \cos\alpha\ +\ \cos\theta\ \sin^2\tfrac{\phi}{2}\ \sin 2\alpha\ &=\ a, \\ -\cos\theta\ \sin\phi\ \cos\alpha\ +\ \sin\theta\ \sin^2\tfrac{\phi}{2}\ \sin 2\alpha\ &= b, \\ \cos^2\tfrac{\phi}{2}\ -\ \sin^2\tfrac{\phi}{2}\ \cos 2\alpha\ &=\ c\ ? \end{aligned} \tag{2.26}$$

(Generic Case when $\alpha \neq 0$ and $c \neq 1$) : Multiplying the first equation by $\cos\theta$ and the second equation by $\sin\theta$ in (2.26), we obtain the following pair of equations

$$\begin{aligned} \sin^2\tfrac{\phi}{2}\ \sin 2\alpha\ &=\ a\ \cos\theta\ +\ b\ \sin\theta, \\ \cos^2\tfrac{\phi}{2}\ -\ \sin^2\tfrac{\phi}{2}\ \cos 2\alpha\ &=\ c. \end{aligned} \tag{2.27}$$

From (2.27) we obtain the following

$$\begin{aligned} \sin^2 \frac{\phi}{2} &= \frac{a \cos\theta + b \sin\theta}{\sin 2\alpha}, \\ \cos^2 \frac{\phi}{2} &= \frac{c \sin 2\alpha + (a \cos\theta + b \sin\theta) \cos 2\alpha}{\sin 2\alpha}. \end{aligned} \tag{2.28}$$

Eliminating ϕ from (2.28), we obtain

$$\frac{a}{1-c} \cos\theta + \frac{b}{1-c} \sin\theta = \frac{\sin 2\alpha}{1 + \cos 2\alpha}, \tag{2.29}$$

where α is given by (2.8), and ϵ is assumed small enough such that $\alpha \neq \pi$. If θ_0 is the angle the vector $(a, b)^T$ makes with respect to the positive x-axis, we can rewrite (2.29) as

$$\sqrt{\frac{1+c}{1-c}} \cos(\theta - \theta_0) = \frac{\sin 2\alpha}{1 + \cos 2\alpha}. \tag{2.30}$$

We solve (2.30) by plotting the right hand side in red and the left hand side in blue as has been shown in Fig. 2.8. The x-coordinate is the θ-axis. The points of intersections are the values of θ that solve (2.30). We have chosen $\epsilon = 0.5$, $a = r \cos\gamma$, $b = +r \sin\gamma$ and $c = \pm\sqrt{1-(a^2+b^2)}$. The parameter r is varied from .1 to .9. In the top three subfigures of Fig. 2.8, the parameter c is chosen to be negative, i.e. the head direction is in the backward hemisphere; for smaller values of r (curves with smaller amplitude) there are four points of intersections; for larger values of r (curves with larger amplitude) there are two points of intersections. In the bottom three figures of Fig. 2.8, the parameter c is chosen to be positive, i.e. the head direction is in the frontal hemisphere; for every value of r, the number of intersection points is two. For each possible choice of θ, we can use (2.28) to calculate the rotation angle ϕ.

Theorem 3 **(Donders):** For a specific pointing direction, (2.30) can be solved for θ up to 2 or 4 alternative solutions, counting multiplicities. Hence the number of orientations for a given pointing directions of the head is either 2 or 4 counting multiplicities.

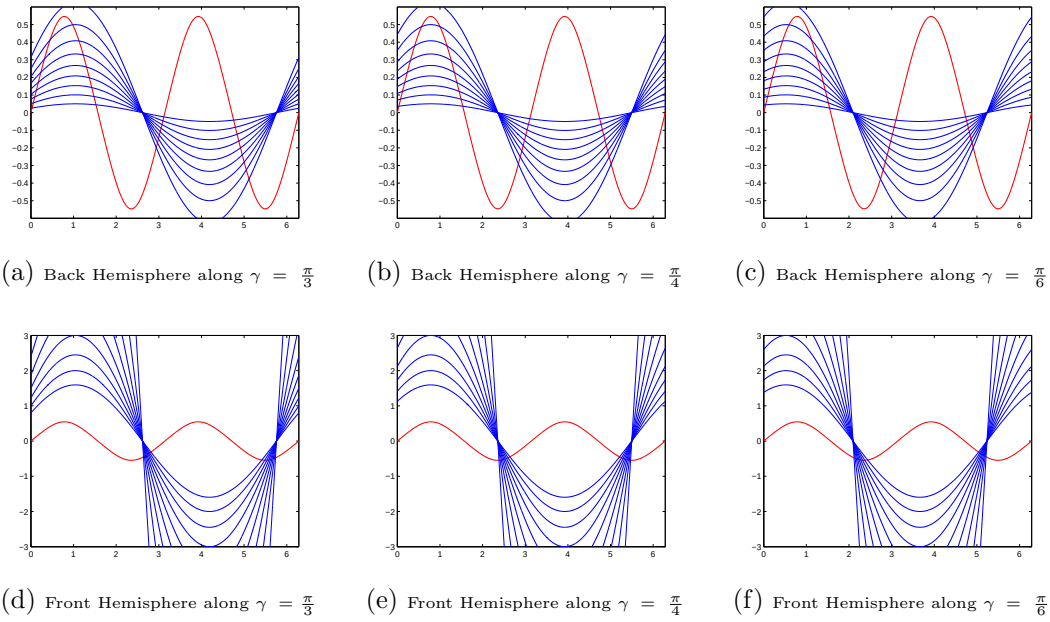

(a) Back Hemisphere along $\gamma = \frac{\pi}{3}$ (b) Back Hemisphere along $\gamma = \frac{\pi}{4}$ (c) Back Hemisphere along $\gamma = \frac{\pi}{6}$

(d) Front Hemisphere along $\gamma = \frac{\pi}{3}$ (e) Front Hemisphere along $\gamma = \frac{\pi}{4}$ (f) Front Hemisphere along $\gamma = \frac{\pi}{6}$

Figure 2.8: In this figure we show that θ can be solved up to two or four alternative choices.

Proof of Theorem 3**:** The generic case when $\alpha \neq 0$ and $c \neq 1$, has already been discussed before. The non generic special cases are discussed below:

(Special Case when $\alpha = 0$**) :** In this case, θ is either 0, $\frac{\pi}{2}$, π or $\frac{3\pi}{2}$. When $\theta = 0$, we have $a = 0$, $b = -\sin\phi$ and $c = \cos\phi$; when $\theta = \pi$, we have $a = 0$, $b = \sin\phi$ and $c = \cos\phi$. Finally when $\theta = \frac{\pi}{2}$ we have $b = 0$, $a = \sin\phi$ and $c = \cos\phi$ and when $\theta = \frac{3\pi}{2}$ we have $b = 0$, $a = -\sin\phi$ and $c = \cos\phi$. The rotation matrix (2.1) is uniquely given by

$$\begin{pmatrix} 1 & 0 & 0 \\ 0 & c & b \\ 0 & -b & c \end{pmatrix}, \text{ when } \theta = 0 \text{ or } \pi \tag{2.31}$$

and

$$\begin{pmatrix} c & 0 & a \\ 0 & 1 & 0 \\ -a & 0 & c \end{pmatrix}, \text{ when } \theta = \frac{\pi}{2} \text{ or } \frac{3\pi}{2}. \tag{2.32}$$

From (2.31) we infer that when $a = b = 0$ and $c = -1$, the gaze direction is precisely backwards. There are exactly two distinct preimages of the mapping 'proj' given by

$$\begin{pmatrix} 1 & 0 & 0 \\ 0 & -1 & 0 \\ 0 & 0 & -1 \end{pmatrix} \text{ and } \begin{pmatrix} -1 & 0 & 0 \\ 0 & 1 & 0 \\ 0 & 0 & -1 \end{pmatrix}. \tag{2.33}$$

(Special Case when $c = 1$) : In this case, it would follow that $a = b = 0$. From (2.27) we would infer that

$$\sin^2 \frac{\phi}{2} \sin 2\alpha = 0; \;\; \cos^2 \frac{\phi}{2} - \sin^2 \frac{\phi}{2} \cos 2\alpha = 1. \tag{2.34}$$

We deduce from (2.34) that $\phi = 0$ and θ is arbitrary. The rotation matrix W, given by (2.1), is trivially the identity matrix.

(Q.E.D)

The main result of Appendix I can be summarized as follows: For head rotation satisfying Donders' Law, for a specific head direction, the head orientation matrix is not necessarily unique but can be ambiguous up to two or four choices. If ϵ is chosen to be 0.5, we observe graphically in Figs. 2.8d, 2.8e, 2.8f that for head direction in the front hemisphere, the head orientation is unique up to two choices. For head direction in the back hemisphere, the head orientation is ambiguous up to two choices, until a threshold, as evidenced by Figs. 2.8a, 2.8b, 2.8c. Closer to the backward head direction, the number of possible head orientations, for a specific head direction, splits up to four. This is also evident in Figs. 2.8a, 2.8b, 2.8c where we notice that blue curves of lower amplitude intersect the red curve at four distinct points.

For different values of ϵ in the Donders' constraint (2.8), the threshold has been computed where the number of solutions of (2.30) jump from 2 to 4, and has been sketched in Fig. 2.9. Outside the shaded region **S** in Fig. 2.9, the number of solutions of (2.30) is precisely 2, counting multiplicity. Inside the shaded region **S** in Fig. 2.9, the number of solutions of (2.30) is no more than 4, and is precisely 4 almost everywhere.

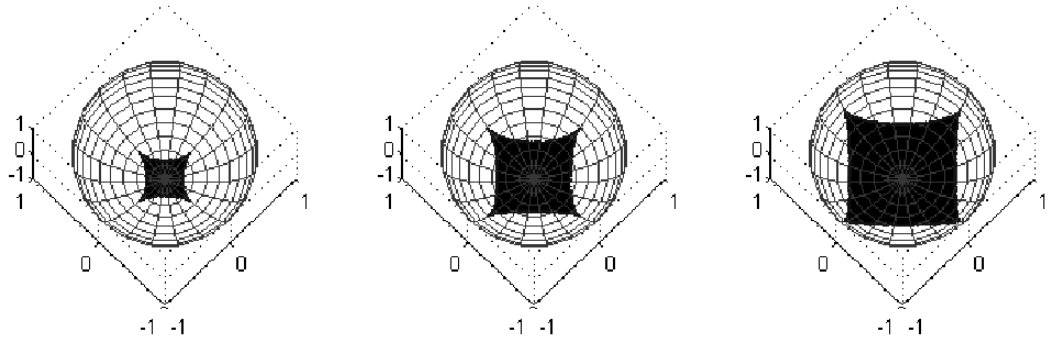

(a) $\epsilon = 0.1$ (b) $\epsilon = 0.2$ (c) $\epsilon = 0.3$

Figure 2.9: Backward pointing direction of the head is shown as the south pole. The shaded regions **S** around the south pole has been sketched for different values of ϵ.

Example I.1 (Example indicating two alternative solutions under Donders' Law): In this example we consider Donders' constraint (2.8) by selecting $\epsilon = 0.5$. For a specific head direction vector $(0.4330 \quad -0.2500 \quad 0.8660)$, we solve (2.30) and obtain $\theta = .9053$ and $\theta = 4.2934$ to be the two distinct solutions. The corresponding values of ϕ are given by $\phi = .5940$ and $\theta = -.5630$. The corresponding orthogonal matrices (2.1) are given by

$$\begin{pmatrix} +0.8798 & -0.1962 & +0.4330 \\ +0.3264 & +0.9116 & -0.2500 \\ -0.3457 & +0.3613 & +0.8660 \end{pmatrix} \text{ and } \begin{pmatrix} +0.8678 & +0.2436 & +0.4330 \\ -0.1440 & +0.9575 & -0.2500 \\ -0.4755 & +0.1546 & +0.8660 \end{pmatrix}. \tag{2.35}$$

Note that the last column of the above two matrices are the same indicating the pointing direction. The first two columns are the orientations of the head. The example shows two distinct orientations for the same head direction. Pointing directions for which the number of distinct solutions of θ is 4 has not been considered in this example.

Example I.2 (Potential control that transfers between two orientations of the head at a given fixed pointing direction): In this example, we construct trajectories on the space $\mathbf{S}^2$ of pointing directions of the head that start and end at the same point. However, the initial and the final point do not correspond to the same

orientation of the head. The trajectories are constructed using the potential function (2.21) assuming $A = B = 1.0$, together with a suitable damping control $\tau_\theta = -1\,\dot{\theta}$ and $\tau_\phi = -1\,\dot{\phi}$. Starting from a fixed pointing direction, two trajectories have been constructed that start and end at the two corresponding head orientations. The results have been displayed in Fig. 2.10. In Fig. 2.10a the blue trajectory is clockwise from left to right as shown in Fig. 2.10b. Correspondingly the black trajectory is anti clockwise from left to right. The extreme left and right orientations correspond to the same pointing direction of the head. In this simulation, ϵ has been chosen as -0.1309.

Remark: One can conclude from the simulation result displayed in Fig. 2.10 that if Donders' constraint has to be satisfied throughout the trajectory of head movement, 'orientation flipping' would require the head to move along a cycle. It is unclear, if such 'head movement gaits' have any functional significance.

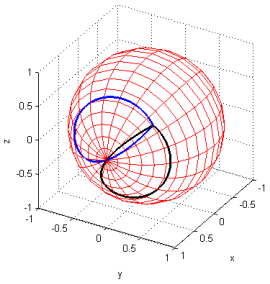

(a) Two trajectories on the space $\mathbf{S}^2$ of pointing directions of the head.

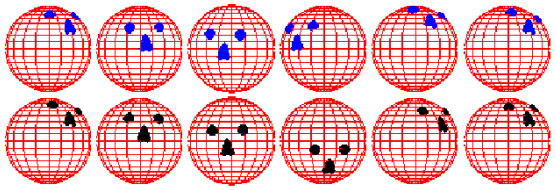

(b) Each of the two trajectories are displayed from left to right showing the head orientations.

Figure 2.10: Orientation flipping head movement using potential control and satisfying Donders' constraint.

2.9 Appendix II: Half Angle Rule

Starting from a specific orientation, in order for the head to move satisfying the Donders' constraint (2.8), the angular velocity and acceleration vectors have to satisfy a constraint. In fact these vectors have to lie in a plane that changes with the moving head. The 'half angle rule,' we consider in this appendix, describes this moving plane. For the eye movement problem satisfying Listing's law such a half angle rule is already

known (see [11]). We obtain a generalization of the half angle rule that would apply to the head movement problem satisfying Donders' constraint. Clearly, half angle rule would be an important constraint to be satisfied in order for the head orientations to satisfy Donders' constraint.

Let us rewrite the unit quaternion (2.2) as

$$q(t) \;=\; \begin{pmatrix} \cos\frac{\phi(t)}{2} \\ \sin\frac{\phi(t)}{2}\; n(t) \end{pmatrix}, \tag{2.36}$$

where $n(t)$ is the axis of rotation given by (2.9). The time derivative of q can be expressed as (see [41])

$$\dot{q}(t) \;=\; \frac{1}{2}\,\tilde{\omega}(t) \;\bullet\; q(t), \tag{2.37}$$

where $\tilde{\omega} \;=\; (0,\omega)$ is a quaternion whose vector part ω is the angular velocity of the 'head' with respect to a fixed universal coordinate attached to the 'body'. (In case of eye movement, ω is the angular velocity of the 'eye' with respect to a coordinate fixed to the 'head'.) The formula (2.37) can be rewritten as

$$\dot{q}(t) \;=\; \frac{1}{2}\begin{pmatrix} -(\omega \,.\, n)\;\sin\frac{\phi}{2} \\ \omega\cos\frac{\phi}{2} \;+\; (\omega\times n)\;\sin\frac{\phi}{2} \end{pmatrix}. \tag{2.38}$$

By computing the derivative of (2.36), we obtain

$$\dot{q}(t) \;=\; \frac{1}{2}\begin{pmatrix} -\sin\frac{\phi}{2}\,\dot{\phi} \\ 2\;\sin\frac{\phi}{2}\,\dot{n} \;+\; \cos\frac{\phi}{2}\,\dot{\phi}\,n \end{pmatrix}. \tag{2.39}$$

Comparing (2.38) and (2.39) we obtain

$$\dot{\phi} \;=\; \omega \,.\, n \tag{2.40}$$

and

$$\sin\frac{\phi}{2}\,\dot{n} \;=\; \frac{1}{2}\;\cos\frac{\phi}{2}\,\omega \;+\; \frac{1}{2}\;\sin\frac{\phi}{2}\,(\omega\times n) \;-\; (\frac{1}{2}\;\cos\frac{\phi}{2}\,\dot{\phi})\,n. \tag{2.41}$$

Let h_D be a vector perpendicular to the Donders' surface at θ. We have

$$\begin{aligned} & h_D \,.\, \dot{n} \; = 0 \Rightarrow \\ & (h_D \,.\, \omega) \, \cos\frac{\phi}{2} \; + \; h_D \,.\, (\omega \times n) \, \sin\frac{\phi}{2} \; - \; (\omega \,.\, n) \, (h_D \,.\, n) \, \cos\frac{\phi}{2} \; = \; 0 \;\; \Rightarrow \\ & \left(h_D \, \cos\frac{\phi}{2} \; - \; (h_D \times n) \, \sin\frac{\phi}{2} \; - \; (h_D \,.\, n) \, \cos\frac{\phi}{2} \, n \right) . \, \omega \; = \; 0. \end{aligned} \tag{2.42}$$

Writing

$$h'_D \; = \; h_D \; - \; (h_D \,.\, n) \, n,$$

we obtain

$$\left(h'_D \, \cos\frac{\phi}{2} \; - \; (h'_D \times n) \, \sin\frac{\phi}{2} \right) . \, \omega \; = \; 0. \tag{2.43}$$

Note that h'_D is an orthogonalization of h_D with respect to the unit 'axis of rotation' vector n. It follows from (2.43) that –

"The angular velocity vector must belong to a plane P_ω passing through n whose normal forms an angle $\frac{\phi}{2}$ with respect to the orthogonalized h'_D".

Remark: One way to think about generating the plane P_ω is to start from h_D and obtain h'_D by orthogonalization. Subsequently rotate using the right hand rule the vector h'_D along the axis n by an angle $\frac{\phi}{2}$. The obtained vector n_ω is orthogonal to the plane P_ω (see Fig. 2.11a for an illustration).

Remark: For the case of eye movement satisfying Listing's Law, the vectors h_D and h'_D are the same vectors and they are equal to $(0, 0, 1)^T$. It is straightforward to verify that the angular velocity vector $(\omega_1, \omega_2, \omega_3)^T$ is given by

$$\begin{pmatrix} \omega_1 \\ \omega_2 \\ \omega_3 \end{pmatrix} \; = \; \begin{pmatrix} \cos\theta \\ \sin\theta \\ 0 \end{pmatrix} \; \dot{\phi} \; + \; \begin{pmatrix} -\cos\frac{\phi}{2} \, \sin\theta \\ \cos\frac{\phi}{2} \, \cos\theta \\ \sin\frac{\phi}{2} \end{pmatrix} \; 2\sin\frac{\phi}{2} \; \dot{\theta}.$$

So in the case of 'Listing', the vector n_ω is explicitly given by

$$\begin{pmatrix} \sin\theta \, \sin\frac{\phi}{2} & -\cos\theta \, \sin\frac{\phi}{2} & \cos\frac{\phi}{2} \end{pmatrix}^T,$$

which clearly has an angle $\frac{\phi}{2}$ with respect to the vector $(0,0,1)^T$. We now state the following theorem.

Theorem 4 **(Half Angle Rule):** A necessary condition for the axis of rotation vector

$$n(\theta) \;=\; \Big(\; \cos\theta\cos\alpha,\;\; \sin\theta\cos\alpha,\;\; \sin\alpha \;\Big)^T,\; \alpha \;=\; \epsilon\sin(2\theta)$$

to remain inside the Donders' surface (2.10) is described as follows. For each value of θ, the angular velocity vector must be confined to a plane P_ω passing through n whose normal forms an angle $\frac{\phi}{2}$ with respect to the vector h'_D, where h'_D is the orthogonalization of h_D with respect to n. Finally, when $\phi \neq 0$ the above necessary condition is also sufficient.

Proof of Theorem 4**:** The necessity of the half angle rule has already been sketched in (2.41), (2.42) and (2.43). When $\phi \neq 0$, using (2.41), it would follow that the implications in (2.42) can be reversed. Thus the half angle rule is also sufficient.

(Q.E.D)

In closing this appendix, we would like to claim that in order for the Donders' constraint to be satisfied, the angular acceleration vector must be constrained to an affine plane parallel to P_ω. Let us define

$$\bar{n}_\omega \;=\; \frac{n_\omega}{\|n_\omega\|},$$

where we have $\bar{n}_\omega \centerdot \omega \;=\; 0$. It follows that the angular acceleration vector $\dot{\omega}$ satisfies $\bar{n}_\omega \centerdot \dot{\omega} \;=\; -\dot{\bar{n}}_\omega \centerdot \omega$. Note that $\bar{n}_\omega \centerdot \dot{\omega}$ is the scalar projection of the vector $\dot{\omega}$ on the vector n_ω normal to the plane P_ω. The acceleration vectors are thus confined to a plane $P_{\dot{\omega}}$ with the property that its scalar projection on n_ω is given by $-\dot{\bar{n}}_\omega \centerdot \omega$. It follows that the acceleration vectors lie in a plane $P_{\dot{\omega}}$ parallel to the plane P_ω at a distance $-\dot{\bar{n}}_\omega \centerdot \omega$ (see Fig. 2.11b for an illustration).

We remark that the vector $\dot{\bar{n}}_\omega$ is perpendicular to n_ω and hence it belongs to the plane P_ω. Under the Listing's constraint, it has been shown in [11] that the vector

$\dot{\bar{n}}_\omega$ is perpendicular to ω. It would therefore follow that for this case, P_ω and $P_{\dot{\omega}}$ are the same plane, as already claimed in [11].

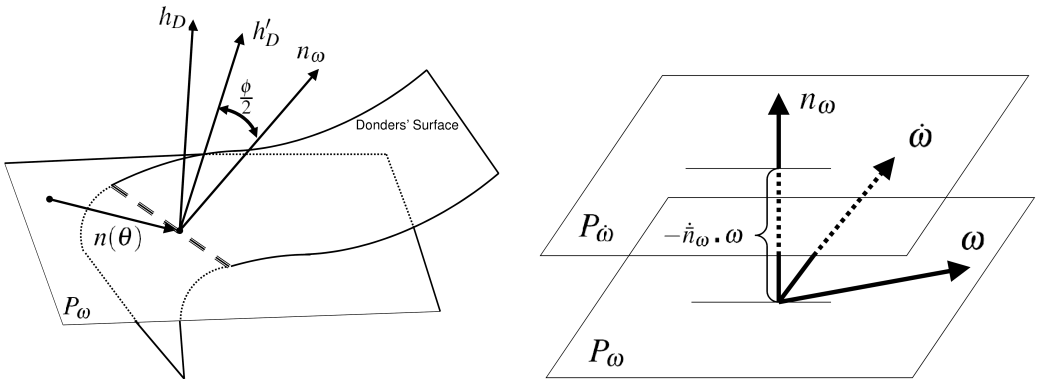

(a) Plane P_ω containing the angular velocity vectors.

(b) Planes P_ω and $P_{\dot{\omega}}$ are parallel.

Figure 2.11: Figure illustrates the construction of P_ω and $P_{\dot{\omega}}$.

Acknowledgement

A good part of this paper was completed when the first author was visiting the 'Cognition for Technical Systems' cluster (CoTeSys) at the Technical University of Munich, Germany during May 2010. Hospitality of Profs. Martin Buss and Sandra Hirche is gratefully acknowledged. Discussions with Dr. Erich Schneider and Dr. Stefan Glasauer, from Ludwig Maximilians University, Munich, on various aspects of the eye and the head movement problem also helped in shaping this paper.

CHAPTER 3
POTENTIAL AND OPTIMAL CONTROL OF HUMAN HEAD MOVEMENT USING TAIT-BRYAN PARAMETRIZATION

Abstract: Human head movement can be looked at, as a rotational dynamics on the space **SO(3)** with constraints that have to do with the axis of rotation. Typically the axis vector, after a suitable scaling, is assumed to lie in a surface called Donders' surface. Various descriptions of the Donders' surface are in the literature and in this paper we assume that the surface is described by a quadratic form. We propose a Tait Bryan parametrization of **SO(3)**, that is new in the head movement literature and describe Donders' constraint in these parameters. Assuming that the head is a perfect sphere with its mass distributed uniformly and rotating about its own center, head movement models are constructed using classical mechanics. A new potential control method is described to regulate the head to a desired final orientation. Optimal head movement trajectories are constructed using a pseudospectral method, where the goal is to minimize a quadratic cost function on the energy of the applied control torques. The model trajectories are compared with observed trajectories of human head movement.

3.1 Introduction

Neurologists, physiologists and engineers have been interested in modeling and control of the eye since 1845 with notable studies conducted by Listing [35], Donders [16] and Helmholtz [59]. Specifically, it has been observed that the oculomotor system chooses just one angle of ocular torsion for any one gaze direction (see Donders [16]). Since its discovery, the Donders' law has also been applied to the head (see Ceylan et al. [13]), which is mechanically able to rotate torsionally, but which normally adopts just one torsional angle for any one facing direction, see Straumann et. al. [51], Glenn and Vilis [26]. A geometric consequence of the Donders' Law is that the three dimensional vectors that represent the 'rotation vectors' of the head are not spread out in a 3-D volume but instead fall in a single two-dimensional surface known as the Donders' surface. It has been further proposed, see Glenn and Vilis [26], Theeuwen et. al. [52], Radau et. al. [45], Tweed et. al. [54], Medendorp et. al. [37], Misslisch et.

al. [39], that Donders' Law follows what is known as the Fick's strategy. According to this strategy, Donders' surface is a saddle-shaped surface, with non-zero torsional components at oblique facing directions, obtained by mildly twisting a plane. Donders' surfaces of various shapes are shown in Fig. 3.1, obtained from experimentally recorded head movement data.

We revisit Donders' Law following the Fick gimbal strategy (see Fick [20]). The Fick strategy of human head movement is to rotate the head in such a way that the line joining the center of the two eyes remain horizontal at all times, assuming that the head orientation initially satisfies this constraint. A typical gimbal system has two axes of rotations, where the assumption is that the first axis is fixed and the second axis rotates with the head, when the head rotates about the first axis. Subsequently, the head also rotates about the second axis. We assume that the fixed axis is the vertical axis, which is perpendicular to the ground and passes through the center of the head. The initial orientation of the second axis is horizontal and is parallel to the line joining the two eyes, also passing through the center of the head. We denote the anticlockwise rotation angle about the fixed (yaw) axis by ϕ_1, and the anticlockwise rotation angle about the nested horizontal (pitch) axis by ϕ_2. The roll is assumed to be zero and the final orientation of the head is a combination of the two rotations, yaw and pitch.

In this paper the Fick gimbal strategy is modified by introducing a non zero roll as a function of yaw and pitch. Let us consider a third axis, initially along the line of gaze perpendicular to the vertical and horizontal axes. We assume that the third axis rotates with respect to the first two axes by angles ϕ_1 and ϕ_2 respectively. Finally, we assume that the head rotates anticlockwise by an angle ϕ_3 with respect to the nested third (roll) axis. A specific rotation in $SO(3)$ can be parameterized by the three angles ϕ_1, ϕ_2 and ϕ_3, and these are called the Tait Bryan angles. Donders' surface is implemented as a constraint on the three angles, to be described later in this paper.

We present the study of head movement using two control strategies, *potential* and *optimal* control. The potential control strategy assumes that the muscles actuating the head movement are guided by an 'artificial' potential term, the minimum of which is adjusted by the final orientation of the specific head movement manoeuvre. Likewise, the optimal control strategy assumes that the three generalized torques

on the model of the head are chosen to minimize a suitably defined quadratic cost function.

Using the Tait-Bryan parametrization we simulate head movement trajectories using potential control, the main idea of which has already been introduced by Ghosh and Wijayasinghe [22]. A new form of the potential function is introduced in this paper that has the advantage of being describable using a form independent of the choice of the coordinates. We also augment the associated Euler Lagrange's equation (see [21]) by adding an appropriate damping term, and the simulated head movements are compared with recorded head movement data.

The optimal control problem of human head movement, employing the dynamics on the Donders' surface and minimizing a quadratic cost function on the control torque input in the Euler Lagrange's equation, is nonlinear and high-dimensional. As a result, they are exceedingly difficult to solve analytically, and we implement a pseudospectral method to transform this optimal control problem into a nonlinear programming problem. This choice of discretization has many advantages (see [18], [50]). As a spectral method using orthogonal functions, the order of approximation (discretization) necessary to capture the dynamics is significantly smaller than conventional finite differences or Runge-Kutta techniques. As a direct collocation method, we can include arbitrary constraints and bounds to restrict both the controls and trajectories of the system. We use this ability to formulate the dynamics on $SO(3)$ and add a separate constraint to impose the Donders' surface. We compare the optimal trajectories with those using potential control, and the shape of the experimental trajectories to find significant agreement.

The choice of the potential function and the cost function are arbitrary. No claim is made that the human brain chooses one strategy or the other. The resulting model head trajectories obtained by simulation are compared with experimental head movement trajectories. Improved error performances are certainly possible if the potential and optimal cost functions are matched to the observed trajectories – a subject of future research.

3.2 Donders' surface described by the Fick gimbal

Head movements can be described as a trajectory in $SO(3)$, the space of rotations. Parametrization of points in $SO(3)$ can be easily obtained from a parametrization of S^3, the unit sphere in $\mathbb{R}^4$. As described in [43], let us assume that the points in S^3 are unit quaternions with a coordinate map given by:

$$\rho \ : \ [0, 2\pi] \ \times [0, \pi] \ \times \ \left[-\frac{\pi}{2}, \frac{\pi}{2}\right] \rightarrow S^3 \tag{3.1}$$

where

$$\rho(\theta, \phi, \alpha) \ = \ \begin{pmatrix} \cos\frac{\phi}{2} \\ \sin\frac{\phi}{2} \ \cos\theta \ \cos\alpha \\ \sin\frac{\phi}{2} \ \sin\theta \ \cos\alpha \\ \sin\frac{\phi}{2} \ \sin\alpha \end{pmatrix}. \tag{3.2}$$

Next we consider the surjective $2-1$ map **rot** from [43], between S^3 and $SO(3)$ given by

$$\text{rot} \ : \ S^3 \rightarrow SO(3). \tag{3.3}$$

The image of the composite map "rot $\circ\, \rho(\theta, \phi, \alpha)$" is a rotation matrix which rotates a vector in $\mathbb{R}^3$ around the axis

$$(\cos\theta \ \cos\alpha, \ \ \sin\theta \ \cos\alpha, \ \ \sin\alpha)^T \tag{3.4}$$

by a counterclockwise angle ϕ. Note that when $\alpha = 0$, the axis (3.4) lies in a plane called the Listing's plane. It follows that α is the angle between the axis of rotation and the Listing's plane and θ is the angle between the projection of the axis of rotation on the Listing's plane and the positive x-axis.

Going back to the Fick strategy for head movements, we can represent the horizontal rotation about the fixed vertical axis, by the quaternion

$$\rho_1 = \rho\left(\frac{\pi}{2}, \phi_1, 0\right).$$

We can also represent the vertical rotation about the nested horizontal axis, by the quaternion

$$\rho_2 = \rho\left(0, \phi_2, \phi_1\right).$$

The resultant quaternion ρ_{fick} is obtained as a quaternion product (see [2]) $\rho_{fick} = \rho_2 * *\rho_1$ given by

$$\rho_{fick}(\phi_1, \phi_2) \;=\; \begin{pmatrix} \cos\frac{\phi_1}{2}\ \cos\frac{\phi_2}{2} \\ \cos\frac{\phi_1}{2}\ \sin\frac{\phi_2}{2} \\ \sin\frac{\phi_1}{2}\ \cos\frac{\phi_2}{2} \\ -\sin\frac{\phi_1}{2}\ \sin\frac{\phi_2}{2} \end{pmatrix}. \tag{3.5}$$

The two parameter family of quaternions (3.5), parameterize the set of all rotation matrices allowed by Fick Gimbals. If we denote

$$\rho_{fick}(\phi_1, \phi_2) \;=\; (q_0, q_1, q_2, q_3)^T \tag{3.6}$$

the Fick strategy implies that the q_i-s satisfy the relation

$$q_0 q_3 \;=\; -q_1 q_2, \tag{3.7}$$

and this Donders' surface has already been introduced in the literature earlier (see for example [26] and [13]).

3.3 Donders' surfaces from human head movement data

We now briefly describe an experimental procedure to collect human head movement data recorded in conjunction with eye movement. For complete details on these experiments, we would refer to Glasauer et. al. [25] and Kremmyda et. al. [33]. Data was recorded from 6 subjects, aged 25 to 38 years with no known neurological or orthopedic disorders. For $3D$ eye movement recordings, a dual search coil was used on the left eye (Skalar, Delft, The Netherlands) and for the 3D head movements, two coils mounted on a head ring at 90° angle between them was used. Both head and eye coil measured absolute position in space. Therefore, when the head was allowed to move, the eye coil recorded gaze (combined eye and head) movements. When the head was fixed, gaze and eye movements were identical. Signals were sampled at 1 KHz. The subjects were seated in complete darkness inside a magnetic field (Remmel Labs) and were instructed to follow a laser dot (size 0.1 deg, distance 145 cm). Details on the calibration method are given elsewhere (Glasauer et. al. [25]). Subjects had to follow the target with a combination of natural eye and head (gaze) movements.

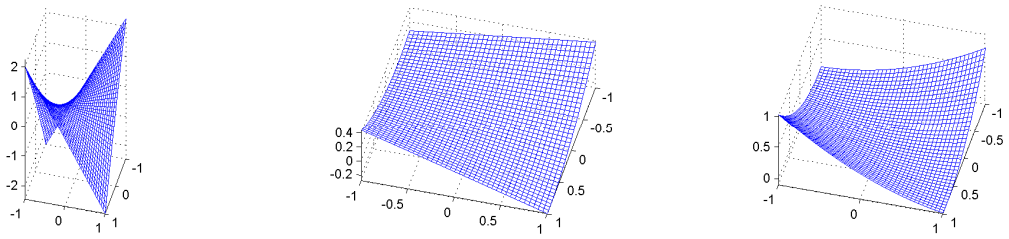

(a) Surface 2 (b) Surface 3 (c) Surface 4

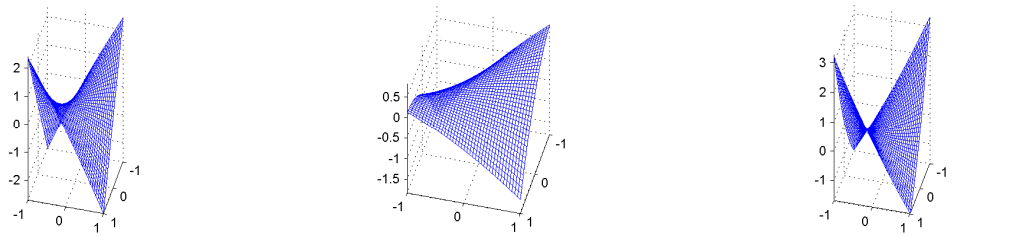

(d) Surface 6 (e) Surface 8 (f) Surface 13

Figure 3.1: Using collected data on human head orientations, six Donders' surfaces displayed in this figure are obtained by regressing the head orientation points represented as unit quaternions. The three coordinates are the scaled coordinates $\bar{q}_1$, $\bar{q}_2$ and $\bar{q}_3$.

The laser dot jumped randomly between the center and eight peripheral positions by 28°, so that each final position is reached from a different initial position four times (maximum target jump is 56° horizontally and vertically). In each position the dot was first visible for 1000ms, then disappeared for 2500ms and appeared again in the same position.

The head movement data had been recorded as a temporal sequence of orientation points, each point represented as a unit quaternion. A second order Donders' surface is obtained by least squares regression [1] using the data points. We obtain six Donders' surfaces (sketched in Fig. 3.1) of the form

$$\bar{q}_3 = h_0 + 2h_1\bar{q}_1 + 2h_2\bar{q}_2 + h_{11}\bar{q}_1^2 + h_{22}\bar{q}_2^2 + 2h_{12}\bar{q}_1\bar{q}_2, \tag{3.8}$$

whose parameters are displayed in Table 3.1.

[1] A system of linear equation is written on the coefficient space of (3.8) using the recorded data $\bar{q}_i$. The coefficients are now calculated using matrix pseudoinverse [10].

Table 3.1: For each of the 6 Donders' surfaces in Fig. 3.1, the parameters from equation (3.8) have been displayed.

Data set	h_0	$2h_1$	$2h_2$	h_{11}	h_{22}	$2h_{12}$
2	-0.0087	-0.0611	+0.0628	-0.1434	-0.0067	-2.2738
3	-0.0129	-0.0680	-0.1032	+0.1626	-0.0015	-0.2548
4	+0.0036	+0.0274	-0.0919	+0.2691	+0.1695	-0.4636
6	-0.0010	-0.0201	+0.0148	+0.0151	-0.1667	-2.5346
8	-0.0062	-0.0912	+0.2553	-0.4585	-0.1278	-1.0661
13	+0.0094	-0.0312	+0.0262	+0.5694	+0.1996	-2.4467

3.4 Tait-Bryan parametrization of the Donders' surface

In this section, we introduce the Tait-Bryan angles [17], [42], given by ϕ_1, ϕ_2, ϕ_3 that generalize the gimbal coordinates. The first two angles are defined as before (see sections 3.1 and 3.2) for the Fick gimbal. An additional third angle ϕ_3 measures rotation with respect to a third axis which is initially orthogonal to the first two axes of head rotation. The instantaneous direction of this third axis is obtained by rotating it by ϕ_1 with respect to the first axis and by ϕ_2 with respect to the rotated second axis. Analogous to (3.5), it turns out that the resultant quaternion is given by

$$\rho_{TaBr}(\phi_1,\phi_2,\phi_3) \;=\; \begin{pmatrix} \sin\frac{\phi_1}{2}\,\sin\frac{\phi_2}{2}\,\sin\frac{\phi_3}{2} \;+\; \cos\frac{\phi_1}{2}\,\cos\frac{\phi_2}{2}\,\cos\frac{\phi_3}{2} \\ \cos\frac{\phi_1}{2}\,\sin\frac{\phi_2}{2}\,\cos\frac{\phi_3}{2} \;+\; \sin\frac{\phi_1}{2}\,\cos\frac{\phi_2}{2}\,\sin\frac{\phi_3}{2} \\ \sin\frac{\phi_1}{2}\,\cos\frac{\phi_2}{2}\,\cos\frac{\phi_3}{2} \;-\; \cos\frac{\phi_1}{2}\,\sin\frac{\phi_2}{2}\,\sin\frac{\phi_3}{2} \\ \cos\frac{\phi_1}{2}\,\cos\frac{\phi_2}{2}\,\sin\frac{\phi_3}{2} \;-\; \sin\frac{\phi_1}{2}\,\sin\frac{\phi_2}{2}\,\cos\frac{\phi_3}{2} \end{pmatrix}. \tag{3.9}$$

In the above representation, $\phi_3 = 0$ reduces to (3.5). In order to impose Donders' constraint, we allow ϕ_3 as a function of ϕ_1 and ϕ_2 in (3.9). Such a parametrization of the Donders' surface would be called the Tait-Bryan parametrization.

We now normalize the above quaternion (3.9) by dividing each term by $\cos\frac{\phi_3}{2}$ and substitute the coordinates in the Donders' surface (3.8). This way, we obtain a quadratic equation in $\tan\frac{\phi_3}{2}$ given by

$$t\,\tan^2\frac{\phi_3}{2} \;+\; s\,\tan\frac{\phi_3}{2} \;+\; r \;=0, \tag{3.10}$$

where t, s and r are functions of ϕ_1 and ϕ_2, details of which are omitted. For those angle variables ϕ_1, ϕ_2 for which $s^2 \;-\; 4\,t\,r \;\geq\; 0$, we solve ϕ_3 as a function of ϕ_1 and

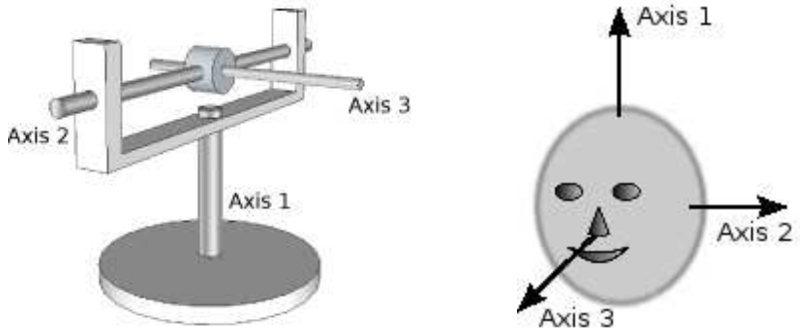

(a) Generalized gimbal frame

(b) Head showing gimbal axes

Figure 3.2: Tait-Bryan angles are ϕ_1, ϕ_2, ϕ_3 where ϕ_i is counterclockwise head rotation, with respect to Axis i.

ϕ_2.

When the discriminant is strictly positive, one can solve (3.10) for ϕ_3 up to two distinct choices. Since, specifying the angles ϕ_1 and ϕ_2 completely specifies the heading direction of the head given by

$$\rho_1 \;=\; \Big(\; \sin\phi_1\;\cos\phi_2 \qquad -\sin\phi_2 \qquad \cos\phi_1\;\cos\phi_2 \;\Big)^T \tag{3.11}$$

the two choices of ϕ_3 for a given heading direction would correspond to two distinct orientations. The following proposition completely summarizes the picture (see [61] for proof).

Proposition: For the angle variables ϕ_1 and ϕ_2 for which the discriminant $s^2 - 4\,t\,r > 0$ there exist precisely two distinct orientations that satisfy the Donders' constraint (3.8) while corresponding to the specific heading direction (3.11). These two orientations are given by two distinct values of ϕ_3. On the other hand, when the discriminant $s^2 - 4\,t\,r < 0$, no orientation would satisfy both the specific heading direction (3.11) and the Donders' constraint (3.8).

3.5 Potentially driven head movement with damping

Our goal in this section is to simulate head movement using the Tait-Bryan parametrization introduced in section 3.4. The head movement trajectories are simulated using an appropriate Lagrangian formulation, the main ideas of which are already sketched in [22], [43]. For the purpose of setting up the notation, we rewrite the main steps as follows.

Let $q(\phi_1, \phi_2)$ be a parametrization[2], of points in S^3 that satisfy the Donders' constraint (3.10). We label this space **DOND** and define Riemannian metric on this space by

$$G \;=\; \begin{pmatrix} q_{\phi_1}.q_{\phi_1} & q_{\phi_1}.q_{\phi_2} \\ q_{\phi_2}.q_{\phi_1} & q_{\phi_2}.q_{\phi_2} \end{pmatrix}, \tag{3.12}$$

where $q_\gamma \;=\; \frac{\partial q}{\partial \gamma}$. Let $X \;=\; (\phi_1, \phi_2)^T$ be the vector of angle variables. As in [43], we would define the Kinetic Energy[3] KE as

$$KE \;=\; \frac{1}{2}\, \dot{X}^T G \dot{X}. \tag{3.13}$$

If the potential energy is represented by V, the Lagrangian of the head movement system can be written as

$$L \;=\; KE \;-\; V. \tag{3.14}$$

The equation of motion on the Donders' surface, using the Euler Lagrange equation can now be described as

$$\frac{d}{dt}\frac{\partial L}{\partial \dot{\gamma}} \;-\; \frac{\partial L}{\partial \gamma} \;=\; \tau_\gamma \tag{3.15}$$

where γ can be the angle variable ϕ_1 and ϕ_2 and where τ_γ is the generalized torque input to the system. The resulting equations of motion can be expressed as

$$G\ddot{X} \;+\; \dot{G}\dot{X} \;-\; \nabla_X L \;=\; \Gamma, \tag{3.16}$$

where $\Gamma \;=\; (\tau_{\phi_1} \quad \tau_{\phi_2})^T$ and where ∇_X is the gradient operator with respect to X

[2] We obtain this parametrization from (3.9) by writing ϕ_3 as a function of ϕ_1 and ϕ_2 given by (3.10)

[3] The head is assumed to be a perfect sphere with mass distributed uniformly. The rotation is assumed to be about the center of the sphere.

defined as

$$\nabla_X \;=\; \left(\frac{\partial}{\partial\phi_1}, \frac{\partial}{\partial\phi_2}\right)^T. \tag{3.17}$$

3.5.1 Choice of a potential function

Potential functions are added to the Lagrangian so that the head movement trajectory can move towards points of least potential[4]. Eye movement to the frontal gaze direction, has been studied in [43] under the influence of the potential function $V(\phi) = \frac{1}{4}\sin^2(\frac{\phi}{2})$, which had a minimum at $\phi = 0$. Eye and head movements are also studied in [22] under the influence of the potential function

$$V(\theta, \phi) \;=\; A\sin^2\frac{\phi - \phi_0}{2} \;+\; B\sin^2\frac{\theta - \theta_0}{2}.$$

The minimum of this potential occurs at $\phi = \phi_0$ and $\theta = \theta_0$. We assume that the pair of angles ϕ_0, θ_0 define a final gaze direction of the eye or pointing direction of the head. We argue in this section that the structure of these potential function are not "coordinate free". It is a priori unclear what the corresponding potential function would be, when the coordinates of the parametrization are altered.

We now propose a new potential function described as follows

$$V(\phi_1, \phi_2) \;=\; A\,(1 - |q(\phi_1, \phi_2).q_0|) \tag{3.18}$$

where q_0 is a fixed unit quaternion on the Donders' surface, and $q(\phi_1, \phi_2).q_0$ represent the dot product of two vectors in $\mathbb{R}^4$. It can be observed that the minima occurs at $q = q_0$ or $q = -q_0$. Both of these minima correspond to a unique point on $SO(3)$ via the map "rot" introduced in (3.3).

3.5.2 Selection of a damping term

A damping term is added externally using the generalized torque input Γ, the goal of which is to dampen the movement of the head so that it comes to a rest at the desired pointing direction and orientation. An earlier paper [22], had considered the

[4] We are not claiming that the brain actually controls the head using a potential function. Instead, we argue that the potential functions generate control signals that actuate the head orientations close to the observed data.

following form of damping:

$$\Gamma \;=\; -K\,\dot{X},$$

where $K \;=\; diag(k_1 \quad k_2)$. This choice of the damping term is coordinate dependent and we modify the choice of damping to the following form:

$$\Gamma \;=\; -c\,G\,\dot{X}, \tag{3.19}$$

where c is an arbitrary constant and G is the Riemannian metric defined in (3.12). With the choice of damping (3.19), the EL equation (3.16) reduces to

$$G\,\ddot{X} \;+\; (\dot{G} \;+\; cG)\,\dot{X} \;=\; \nabla_X\,L. \tag{3.20}$$

Assuming $V \equiv 0$, it has been shown in [61] that for different values of the parameter c, the integral curves of (3.20) follow portion of the geodesic curve. This fact has been further illustrated in [61].

3.6 Head movement as a potential control problem

Consider the head movement dynamics on **DOND**, described by the EL equation (3.20). The potential function (3.18) drives the state of the head from an initial to a final orientation. One can separate the contribution of the potential and the damping term and rewrite (3.20) as

$$G\,\ddot{X} \;+\; \dot{G}\,\dot{X} \;-\; \frac{1}{2}\,\dot{X}^T\,\nabla_X G\,\dot{X} \;=\tilde{\Gamma} \tag{3.21}$$

where we write $\tilde{\Gamma}$ as

$$\tilde{\Gamma} \;=\; -\nabla_X V \;-c\,G\,\dot{X}. \tag{3.22}$$

The head movement dynamical system can now be viewed as being controlled by $\tilde{\Gamma}$ where the contributions of the potential and the damping terms can be implemented by a controller. This, in essence, is the **Potential Control Problem**. We now propose to extend the potential control formulation (3.21), (3.22) as a dynamical system on $\mathbf{S}^3$ (instead of **DOND**). The Donders' constraint is additionally imposed using Lagrange multiplier. The details are described as follows.

Let $q(\phi_1, \phi_2, \phi_3)$ be a parametrization of points in S^3 given by (3.9). We define Riemannian metric on S^3 given by a 3×3 matrix G, analogous to (3.12), where $q_\gamma = \frac{\partial q}{\partial \gamma}$. Let $X = (\phi_1, \phi_2, \phi_3)^T$ be the vector of angle variables. As in [43], we would define the Kinetic Energy KE as

$$KE = \frac{1}{2} \dot{X}^T G \dot{X}. \tag{3.23}$$

As in (3.18), if the potential energy V is chosen as

$$V(\phi_1, \phi_2, \phi_3) = A\,(1 - |q(\phi_1, \phi_2, \phi_3).q_0|), \tag{3.24}$$

where q_0 is a fixed unit quaternion in **DOND** and $q(\phi_1, \phi_2, \phi_3).q_0$ represent the dot product of two vectors in $\mathbb{R}^4$, the Lagrangian of the head movement system can be written as

$$L = KE - V. \tag{3.25}$$

We can impose the Donders' constraint at this point by defining

$$\tilde{L} = L + \lambda F = KE - V + \lambda F, \tag{3.26}$$

where $F \equiv 0$ is the Donders' constraint (of the kind described in (3.10)) and λ is the Lagrange multiplier. The equations of motion in S^3 subjected to the Donders' constraint can then be derived by using the Euler Lagrange equations which can be described as

$$\frac{d}{dt}\frac{\partial \tilde{L}}{\partial \dot{\gamma}} - \frac{\partial \tilde{L}}{\partial \gamma} = \tau_\gamma, \tag{3.27}$$

where γ is the angle variables ϕ_1, ϕ_2, ϕ_3 and λ; and where τ_γ is the generalized torque input to the system and $\tau_\lambda = 0$. The resulting equations of motion can be expressed as

$$G\,\ddot{X} + \dot{G}\,\dot{X} - \frac{1}{2}\,\dot{X}^T\,\nabla_X G\,\dot{X} + \nabla_X V - \lambda\,\nabla_X F = \Gamma, \tag{3.28}$$

where $\Gamma = (\tau_{\phi_1}, \tau_{\phi_2}, \tau_{\phi_3})^T$ and ∇_X is the gradient operator with respect to X. The definition of the gradient operator is similar to (3.17). Equation (3.28) can be written in a reduced form as

$$G\,\ddot{X} + \dot{G}\,\dot{X} - \nabla_X \tilde{L} = \Gamma. \tag{3.29}$$

As in section 3.5.2, we would add a damping term of the form (3.19) and write (3.29) as (3.21), where we define a new torque $\tilde{\Gamma}$ as

$$\tilde{\Gamma} = \lambda \nabla_X F - \nabla_X V - c\, G\, \dot{X}. \tag{3.30}$$

The system of equations (3.21), (3.30) together with the Donders' constraint $F \equiv 0$ provide a description of a controlled dynamical system for which the Lagrange multiplier $\lambda(t)$ can be computed implicitly[5].

3.7 Optimal control using pseudospectral method

In this section, we reconsider the head movement dynamics (3.21), without the assumption that the control $\tilde{\Gamma}$ is generated from (3.22), using a potential function V and a damping term. The potential and the damping terms are assumed to be absent from the head movement dynamics and the control $\tilde{\Gamma}$ is written as $(\tau_{\phi_1}, \tau_{\phi_2}, \tau_{\phi_3})^T$. As before, the state vector X is given by $(\phi_1, \phi_2, \phi_3)^T$.

For a given T, the optimal control problem we propose to consider is to drive the state $(X, \dot{X})$ from a given initial value $(X(0), 0)$ to a given final value $(X(T), 0)$ while minimizing the cost function

$$\int_0^T \left[\tau_{\phi_1}^2(t) + \tau_{\phi_2}^2(t) + \tau_{\phi_3}^2(t)\right] dt. \tag{3.31}$$

The initial and the final values of the state are assumed to lie on the Donders' surface (3.10) and the control torques are computed so that the states evolve on this Donders' surface as well [6].

Redefining the state variables as $\xi_1 = (\phi_1, \phi_2, \phi_3)^T$ and $\xi_2 = (\dot{\phi}_1, \dot{\phi}_2, \dot{\phi}_3)^T$, the EL equation (3.28) is written as

$$\dot{\xi}_1 = \xi_2; \;\; G\,\dot{\xi}_2 + \dot{G}\,\xi_2 - \frac{1}{2}\,\xi_2^T\,\nabla_{\xi_1} G\,\xi_2 = \tau_\phi. \tag{3.32}$$

[5] The Potential Control approach introduced, shares the same framework with Equilibrium Point Hypothesis (EPH), used by a lot of researchers in human motor control (see for example [27] and [19]).

[6] We remark that the Donders' constraint is implemented directly during solving the optimal control problem numerically, and not with the aid of a Lagrange's multiplier, as has been the case in (3.26). The Lagrange multiplier is assumed to be 0.

The Donders' constraint (3.10) is given by $F(\xi_1) = 0$, where

$$F(\xi_1) = t(\phi_1, \phi_2) \tan^2 \frac{\phi_3}{2} + s(\phi_1, \phi_2) \tan \frac{\phi_3}{2} + r(\phi_1, \phi_2),$$

and t, s, r are defined in (3.10). The boundary conditions are given by

$$\begin{aligned} \xi_1(0) &= (\phi_{10}, \phi_{20}, *), \ \ \xi_1(T) = (\phi_{1T}, \phi_{2T}, *), \\ \dot{\xi}_1(0) &= \dot{\xi}_1(T) = (0, 0, 0), \ \ \forall\, t \in [0, T]. \end{aligned}$$

The control τ_ϕ is described by the vector $(\tau_{\phi_1}, \tau_{\phi_2}, \tau_{\phi_3})$ of generalized torques and $*$ denotes a free parameter so that the initial and final states lie on the Donders' surface (3.10).

Taken together, the preceding cost function (3.31), dynamics (3.32), and Donders' state-constraint (3.10) form an optimal control problem. While analytical methods (i.e., the maximum principle) exist to solve such problems, systems of this size and complexity are typically intractable and, therefore, require computational methods to solve them [44]. A variety of numerical methods exist for solving optimal control problems and can generally be classified as either direct or indirect. An indirect method finds approximate solutions to the two point boundary value problem given by the necessary conditions of the maximum principle. Applying an indirect method requires first solving for this set of coupled state and adjoint equations. When working with complex nonlinear systems, especially those employing nonlinear constraints, this can be both difficult and tedious. A direct method avoids these issues by directly discretizing the original problem into a nonlinear programming problem. Since all variables are physically relevant to the problem (contrast this with adjoint variables in indirect methods), this facilitates adding additional constraints as needed. For these reasons, we use a direct method to solve for the optimal torques.

We implement a pseudospectral method to solve the optimal control problem described above. This method relies on approximation by orthogonal polynomials (in our case we use the Legendre polynomials), which admits spectral accuracy, similar to a Fourier approximation for periodic functions [7]. This type of approach has been used effectively to solve problems in Fluid Dynamics, and since then the related concepts have been successfully applied in a wide variety of domains, including satellite

motion [18] and quantum mechanics [50]. The pseudospectral method uses orthogonal polynomial expansion to approximate the states and controls of the system and thereby inherit the spectral accuracy characteristic of such expansions [47] (the k^{th} coefficient of the expansion decreases faster than any inverse power of k) [12]). Using recursive properties unique to certain classes of orthogonal polynomials, e.g. Legendre and Chebyshev, derivatives of the states can again be expressed in terms of the orthogonal polynomial expansions, making it possible to accurately approximate the differential equation that describes the dynamics with an algebraic relation imposed at a small number of discretization points.

The pseudospectral method discretizes the continuous cost, dynamics, and constraints using interpolation on a set of Gauss-Lobatto nodes specially selected for near-optimal convergence in terms of the approximation [49]. Using an expression that relates the $k+1$ and k terms of the interpolation functions, we can rewrite the dynamics as an algebraic relation. Leveraging the interpolation on the selected nodes in a different way permits a highly accurate approximation of the integrated cost, using Gaussian quadrature [12]. For additional details on the computational method, see [7, 12].

3.8 Results

Important results of this paper are displayed in the form of trajectories sketched in Figs. 3.3, 3.4, 3.5 using scaled coordinates $\bar{q}_i = \frac{q_i}{q_0}$ for $i = 1, 2, 3$ (see equation (3.6)). For each of the six subjects, from which the head movement data has been collected, the figures display how the trajectories generated by the potential and the optimal controller compare with the recorded head movement data. Recall that, during data collection, the human subjects directly moved their head between two pointing directions.

The optimal control torques and trajectories are obtained over a fixed duration $T = 1$ with initial and final conditions for (ϕ_1, ϕ_2) taken from recorded head movement trajectories. The optimal controller is computed ensuring that the state remains sufficiently close to the Donders' surface. For the purpose of comparison, the parameters in the potential control are adjusted so that the final time is approximately $T = 1$. This is achieved by choosing the potential control coefficient A in (3.24) to

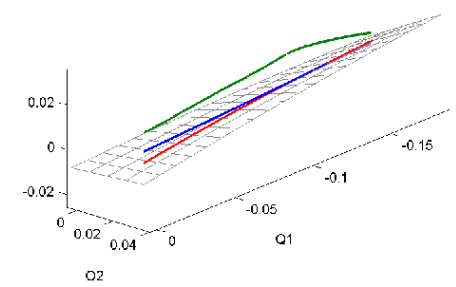

(a) Trajectory from surface 2

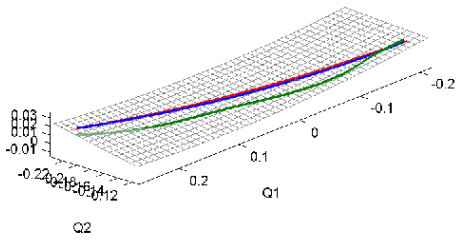

(b) Trajectory from surface 3

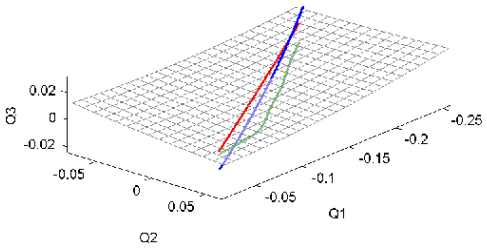

(c) Trajectory from surface 4

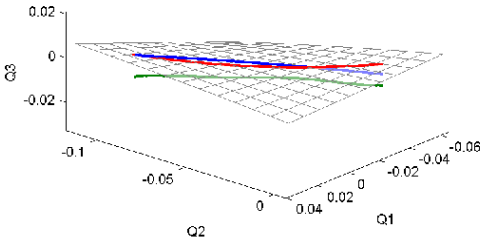

(d) Trajectory from surface 6

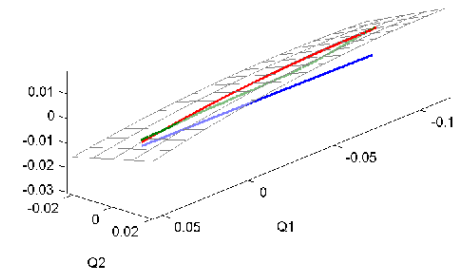

(e) Trajectory from surface 8

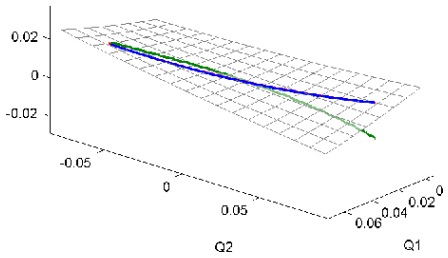

(f) Trajectory from surface 13

Figure 3.3: One specific head movement trajectory is shown for each of the six Donders' surfaces in Fig. 3.1 on the coordinate space $\bar{q}_1$, $\bar{q}_2$ and $\bar{q}_3$. Green lines are from the experimentally collected head movement data. Red lines are from the simulated trajectories using potential control (3.29), (3.30), where V is described in (3.24). Blue lines are from the simulated trajectories using optimal control minimizing (3.31). Parameters A and c are chosen as 35 and 10, respectively.

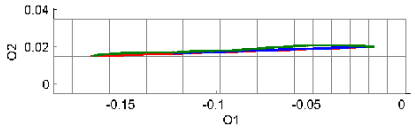

(a) Projected from Fig. 3.3a

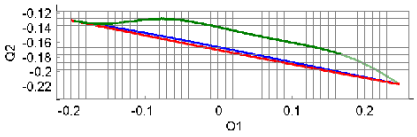

(b) Projected from Fig. 3.3b

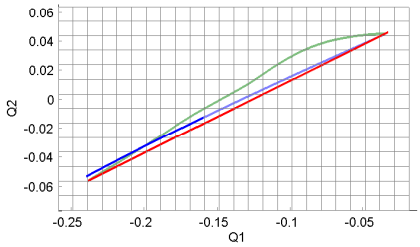

(c) Projected from Fig. 3.3c

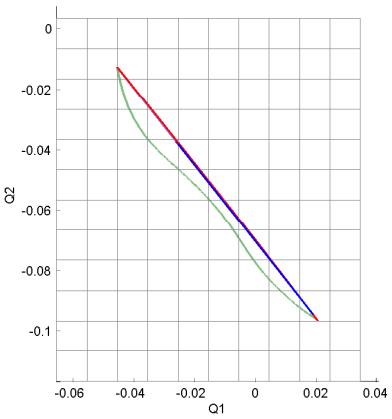

(d) Projected from Fig. 3.3d

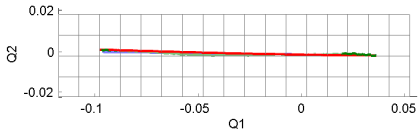

(e) Projected from Fig. 3.3e

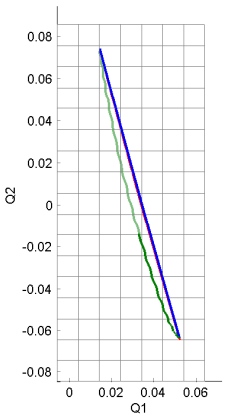

(f) Projected from Fig. 3.3f

Figure 3.4: Head movement trajectories from Fig. 3.3 are projected on the plane $\bar{q}_1$, $\bar{q}_2$. The projected trajectories indicate that the simulated trajectories are linear on the plane and does not capture fluctuations of the recorded head movement trajectories from a line. Potential and optimal trajectories overlap sometimes, and in those cases all three colors are not visible.

be 35 and the friction coefficient c in (3.19) to be 10.

The recorded and the simulated head movement data are points on the unit quaternion S^3. We display the trajectory of data points on a coordinate chart defined by $(\bar{q}_1, \bar{q}_2, \bar{q}_3)$ in Fig. 3.3. Ideally, since the head orientations satisfy Donders' constraint (3.8), it would follow that $\bar{q}_3$ depends completely on $\bar{q}_1$ and $\bar{q}_2$. Hence the head movement trajectories can also be plotted on the $(\bar{q}_1, \bar{q}_2)$ plane, as shown in Fig. 3.4. For each of the six subjects, multiple trajectories have been picked and the corresponding trajectories are displayed in Fig. 3.5, together with the simulated potential and optimal trajectories. Out of the multitude of trajectories, one specific trajectory has been picked for each of the six subjects, and displayed in Fig. 3.3. The initial and final points of the simulated trajectories do not match with the recorded trajectories because simulations are carried out by projecting the recorded points on the Donders' surface. Whereas the recorded trajectories are not precisely on the Donders' surface, the simulated trajectories are sufficiently close to the surface. In Table 3.2 we display the maximum error percentage between the simulated and the recorded trajectories for each of the trajectories in Fig. 3.5. The error is computed as an angle between the corresponding unit quaternion vectors after we have reparameterized each point of a trajectory as a function of the arc length. Finally, the error is represented as a percentage of the angle between the initial and final unit quaternion vector. From this table, we observe that the percentage of maximum error between simulated and recorded trajectories vary, roughly between 3% and 23%, where the percentage is calculated with respect to the total angular deviation between the initial and final point of the trajectory[7]. By and large, the maximum error is observed to be less than 2°.

For each of the six cases displayed in Fig. 3.3, the potential and the optimal control torques are displayed in Figs. 3.6 and 3.7. The three components of the torques are displayed in three different colors. The costs of potential and optimal controls are computed, using (3.31), for each of the six subjects undergoing ten different head movement maneuvers, shown in Fig. 3.5. These results, displayed in Fig. 3.8, show that by and large the cost of potential control is about five times more than the cost of optimal control.

[7] Note that while calculating the errors, the temporal dependance of the trajectories are not looked into. Also higher percentage errors are for shorter trajectories.

On viewing the controllers sketched in Fig. 3.6, 3.7 we observe that the potential controller takes a relatively large value during the initial phase of the control action. The magnitude of the control tapers off subsequently, receding to the value 0 at the final time $T = 1$. The optimal controller, on the other hand, remains relatively active throughout the time interval $[0, 1]$ and does not approach 0 at the final time. In practice this would imply that the optimal controller has a discontinuity at $T = 1$. In view of its structure, we comment that the potential controller mimics a PD (proportional - derivative) controller [3].

The simulated trajectories arising from potential and optimal controllers differ from the corresponding trajectories recorded from the head movement data in essentially two ways. First of all, the simulated trajectories are closely restricted to the constraint imposed by Donders, whereas the recorded trajectories are not entirely restricted by the Donders' surface, i.e. there are small deviations away from the surface. This is evident in Fig. 3.3. Secondly, restricted to the Donders' surface, the simulated data differs from the recorded data essentially by virtue of the fact that simulated head movements do not allow for 'excursions' during the transition between initial and final orientations. This is evident when the trajectories are projected on the $(\bar{q}_1, \bar{q}_2)$ plane (see Fig. 3.4, where the simulated trajectories are linear whereas the recorded trajectories do have some amount of curvature). The curvature may have been introduced artificially when the recorded movement data was split up into a cascade of trajectories, with initial and final pointing directions recognized when the head is observed to stop momentarily. The curvature may be a result of the subject hesitating, before settling on a final head pointing direction. The potential or the optimal trajectories do not capture these effects.

In the head movement experiments that generated the data, the generalized torques applied to the head are not directly measured. Hence it is not possible to compare the actual cost of control with the cost of controls recorded in Fig. 3.8. It is however possible to estimate the generalized torques τ_{ϕ_1}, τ_{ϕ_2}, τ_{ϕ_3}, using the recorded trajectories of the head orientations and the model (3.32). For the trajectories displayed as green lines in Fig. 3.3, the generalized torques are computed and plotted in Fig. 3.9. One should compare the estimates of the generalized torques in Fig. 3.9 with the torques obtained in Figs. 3.6, 3.7 for the Potential and Optimal control tasks. The following

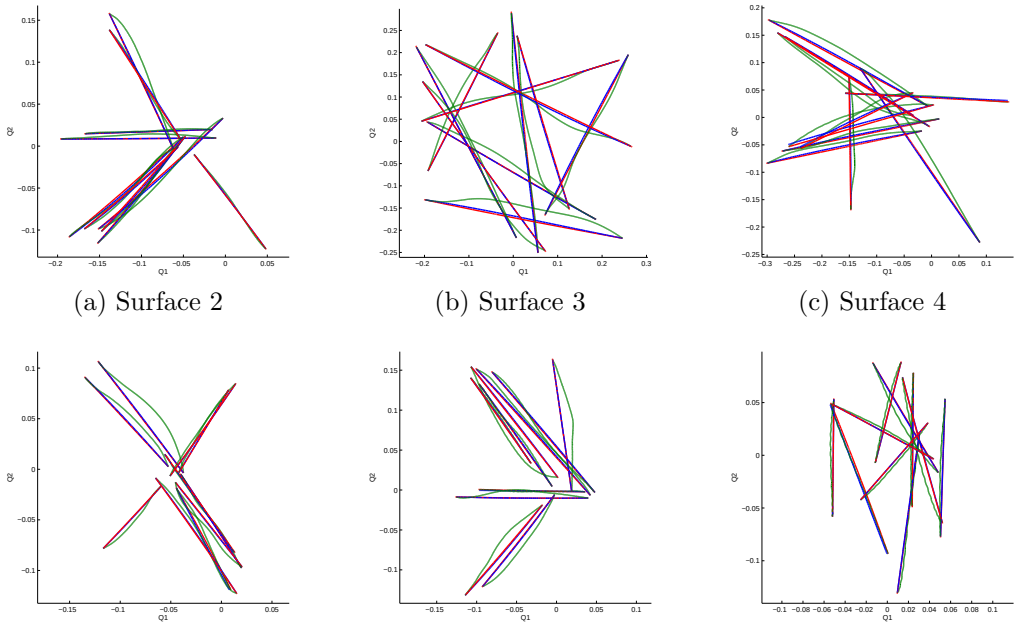

(a) Surface 2 (b) Surface 3 (c) Surface 4

(d) Surface 6 (e) Surface 8 (f) Surface 13

Figure 3.5: Head movement trajectories are shown for six surfaces in Fig. 3.1. Green lines are the trajectories from the experimentally collected head movement data. Red lines are the head movement trajectories using potential control with parameters chosen as in Fig. 3.3. Blue lines are the head movement trajectories generated using optimal control minimizing (3.31). All trajectories are displayed by projecting on to the $\bar{q}_1$ $\bar{q}_2$ plane where $\bar{q}_1 = \frac{q_1}{q_0}$ and $\bar{q}_2 = \frac{q_2}{q_0}$.

points are noted.

Qualitatively, the estimated torques (in Fig. 3.9) do not asymptotically approach zero[8], i.e. the controls remain active throughout the time interval as is the case with optimal torques and unlike the potential torques (in Figs. 3.6, 3.7). The costs of the estimated torques, measured by (3.31), show that their values are close to the optimal torques described in Fig. 3.8 (see Table 3.3). In some cases the cost of the estimated torques are less than what is computed for the optimal torques. This is possibly because the optimal control is derived for a trajectory restricted entirely on the Donders' surface, whereas the estimated torques are derived on a trajectory that often deviates out of the Donders' surface (see Fig. 3.3).

[8] Although in some cases they veer close to zero.

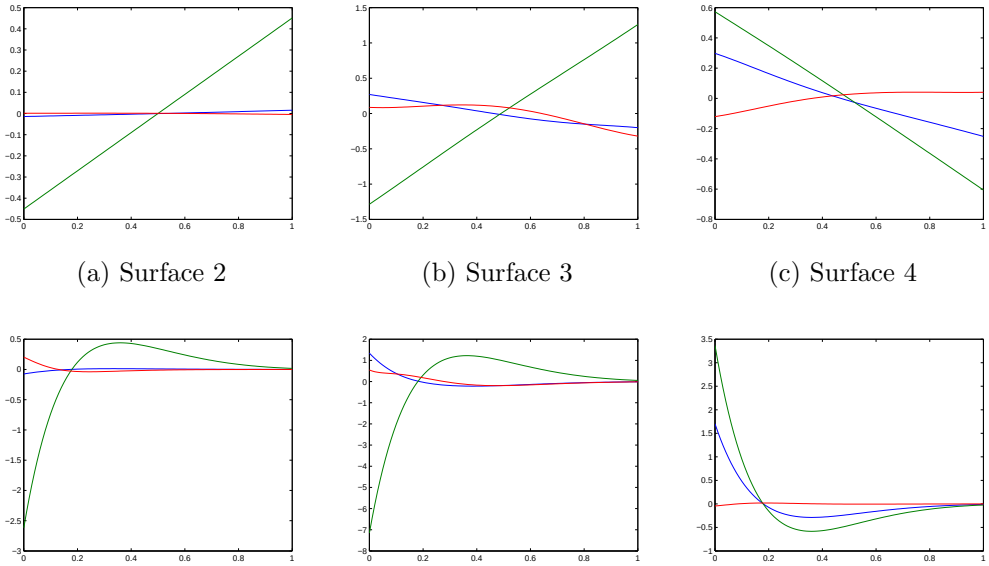

(a) Surface 2 (b) Surface 3 (c) Surface 4

(d) Surface 2 (e) Surface 3 (f) Surface 4

Figure 3.6: Comparison of torques from the optimal control vs torques from the potential control for Donders' surfaces 2, 3 and 4. Blue is τ_{ϕ_1}, Green is τ_{ϕ_2} and Red is τ_{ϕ_3}. Top figures, left to right are optimal torques from Figs 3.3a, 3.3b and 3.3c. Bottom figures, left to right are potential torques from Figs 3.3a, 3.3b and 3.3c.

3.9 Conclusion

This paper introduces a dynamic model of human head rotation, using a newly introduced Tait Bryan parametrization. The space of head orientations is viewed as a (Donders') submanifold of unit quaternions, endowed with a Riemannian metric. The movement dynamics is derived by writing the associated Euler Lagrange's equation, with a generalized torque as control. The control problem, we consider, is to drive the orientation vector from a given initial value to a given final value, staying within the Donders' submanifold, while maintaining the time derivative to be zero at the two boundaries. Two different control strategies are introduced. In the *Potential Control* strategy, the orientation vector is driven by a gradually reducing potential function, attaining the zero value at the end point. In the *Optimal Control* strategy, the orientation vector is transferred between the two boundary points by a minimum energy controller. A direct, pseudospectral method is introduced to derive the optimal

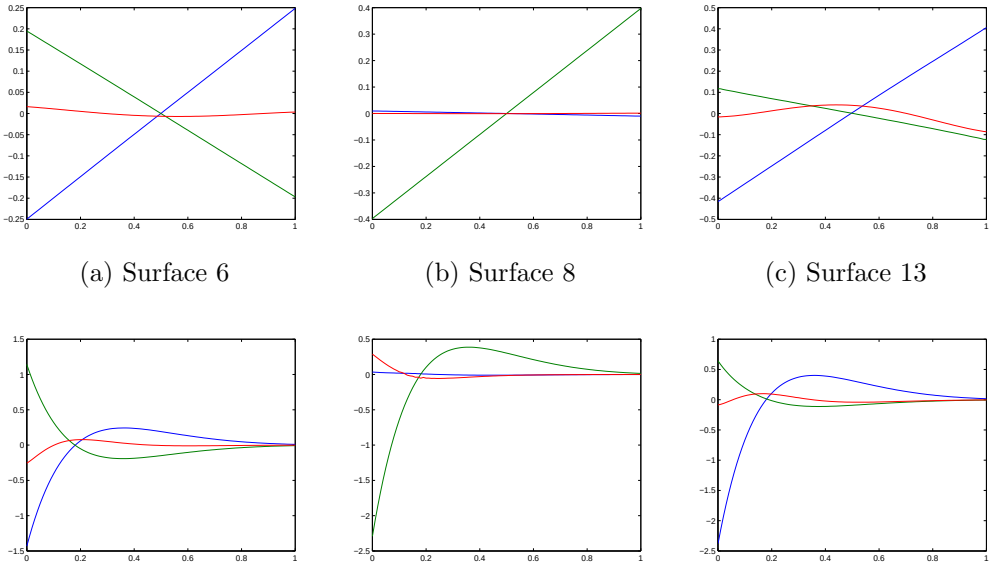

(a) Surface 6 (b) Surface 8 (c) Surface 13

(d) Surface 6 (e) Surface 8 (f) Surface 13

Figure 3.7: Comparison of torques from the optimal control vs torques from the potential control for Donders' surfaces 6, 8 and 13. Blue is τ_{ϕ_1}, Green is τ_{ϕ_2} and Red is τ_{ϕ_3}. Top figures, left to right are optimal torques from Figs 3.3d, 3.3e and 3.3f. Bottom figures, left to right are potential torques from Figs 3.3d, 3.3e and 3.3f.

controller.

Recorded head movement trajectories are compared with simulated trajectories from potential and optimal strategies. In an appropriately chosen coordinate plane, the simulated trajectories are approximately linear, lying sufficiently close to the Donders' surface, whereas this is not the case with the recorded data. The control actions between potential and optimal controller are also different. A potential controller is strong initially and gradually tapers off towards the end. An optimal controller, on the other hand, remains active throughout the entire time interval and its value goes to zero discontinuously at the final time. For each of the six subjects, we have made some observations as to what extent the estimated control action is 'potentially' or 'optimally' driven. The estimated control does not taper off to zero, an indication of the fact that perhaps the final head orientation is not of any major concern to the subject.

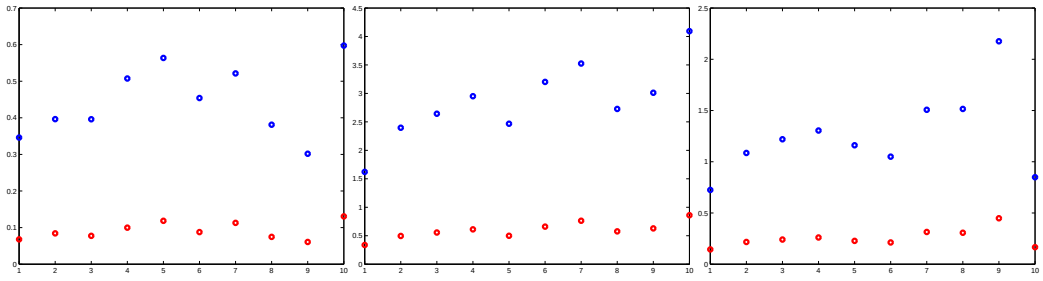

(a) Surface 2 (b) Surface 3 (c) Surface 4

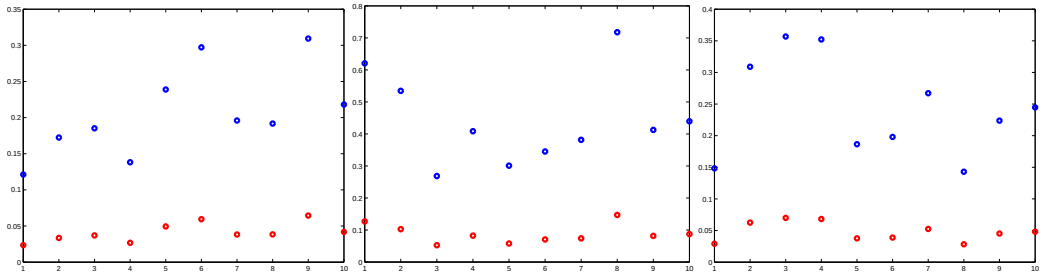

(d) Surface 6 (e) Surface 8 (f) Surface 13

Figure 3.8: Values of the cost function (3.31) for the potential and optimal control are plotted in the y-axis. In the x-axis we have the trajectory index for each of the 10 trajectories in Fig. 3.5. The optimal control has been plotted in red whereas the potential control is shown in blue.

None of the six subjects in this paper used potential based control as evident from the cost of the control signals, which was found to be close to that of the proposed optimal control. While subjects used a control that generated head movement trajectories close to both the potential and optimal trajectories, the estimated control functions differ not only from the predictions of potential control, but also from those of the optimal control. It is unclear (and a good question for future research) whether the differences between the estimated actual control strategy used by the subjects and the proposed optimal control are due to, for example, differences in head dynamics or cost function used.

Acknowledgement

The paper is based upon work supported in part by the National Science Foundation under Grant No. 1029178. Any opinions, findings, and conclusions or recommendations expressed in this material are those of the author(s) and do not necessarily

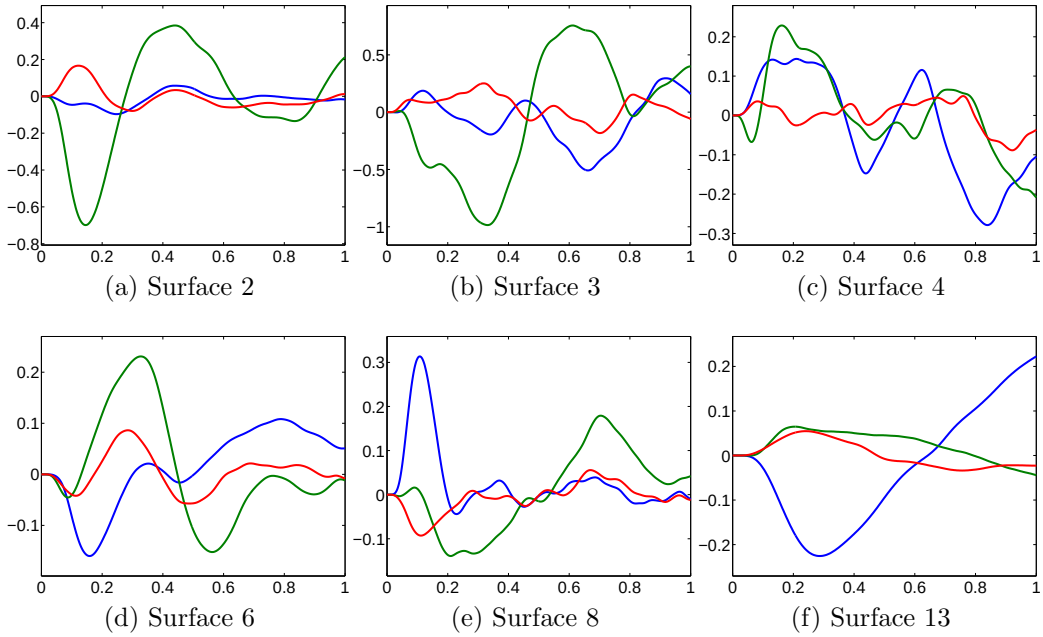

(a) Surface 2 (b) Surface 3 (c) Surface 4

(d) Surface 6 (e) Surface 8 (f) Surface 13

Figure 3.9: Torques computed from recorded head movement data (displayed as green lines in Fig. 3.3), and the model (3.32). Blue is τ_{ϕ_1}, Green is τ_{ϕ_2} and Red is τ_{ϕ_3}.

reflect the views of the National Science Foundation. Part of this research is also supported by BMBF Grant No. 01E00901.

Table 3.2: Maximum error between simulated and recorded trajectories have been displayed for each of the trajectories in Fig. 3.5. P and O stand for the trajectories using potential and optimal control respectively. T is the total angular displacement of a trajectory, the angle between initial and final orientation represented as a unit quaternion. Error between two trajectories is calculated as the maximum angle between corresponding quaternion vectors and tabulated as a percentage of T.

Surfaces / Trajectories	2			3			4			6			8			13		
	P (%)	O (%)	T (°)	P (%)	O (%)	T (°)	P (%)	O (%)	T (°)	P (%)	O (%)	T (°)	P (%)	O (%)	T (°)	P (%)	O (%)	T (°)
1	9.59	9.10	8.61	7.62	7.73	19.81	7.20	12.06	12.79	15.85	15.73	4.81	10.84	10.60	11.44	23.12	23.16	5.72
2	7.12	6.80	9.04	10.35	10.06	23.39	7.87	8.22	15.18	11.20	10.22	6.06	12.14	12.63	10.59	12.75	12.78	8.30
3	3.13	2.62	8.73	5.69	5.76	24.64	3.90	2.48	16.32	7.29	7.29	6.32	3.41	8.64	7.60	6.77	6.71	8.78
4	3.71	6.66	10.47	8.43	8.42	25.94	5.22	5.93	16.92	4.52	4.31	5.45	11.86	11.64	9.10	9.22	13.72	8.77
5	9.77	9.74	10.97	7.11	7.14	22.67	7.23	7.06	16.02	14.22	14.12	7.25	4.62	4.37	7.73	12.40	12.37	6.32
6	8.53	8.47	9.46	6.58	6.58	27.09	10.59	11.09	15.38	6.51	6.30	7.93	11.72	11.93	8.99	6.49	3.25	6.39
7	7.53	7.20	10.34	8.24	7.90	28.77	5.34	4.49	18.33	14.71	10.26	6.51	9.34	9.62	9.00	4.09	4.00	7.47
8	5.28	5.74	8.59	6.93	6.10	25.08	7.52	8.14	18.03	10.69	10.72	6.40	8.47	8.47	12.36	12.58	12.68	5.58
9	5.13	5.15	8.05	6.95	6.97	26.41	7.29	7.52	21.92	10.59	10.22	8.30	10.26	10.25	9.48	9.27	9.08	6.97
10	13.01	12.76	11.46	6.47	6.37	30.49	5.65	5.43	13.60	4.28	9.30	6.80	12.05	11.99	9.71	6.23	6.23	7.24

Table 3.3: The table shows costs of estimated torques from Fig. 3.9. The trajectory numbers correspond to the indices displayed in Fig. 3.8. Only one trajectory out of ten has been chosen for each of the six surfaces, as displayed in Fig. 3.3.

Surface #	2	3	4	6	8	13
Trajectory #	1	8	1	2	3	2
Cost from (3.31)	0.0937	0.3820	0.0473	0.0247	0.0176	0.0180

CHAPTER 4
POTENTIAL AND OPTIMAL CONTROL OF THE HUMAN HEAD/EYE COMPLEX

Abstract: Human head and eye rotate in coordination to rapidly project images of targets from the visual space. Once a target is fixated, the head/eye complex maintains the stability of the image, even while the head continues to move. The orientation of the head is constrained by Donders' Law whereas the final orientation of the eye satisfies Listing's constraint with respect to the final orientation of the head. The vestibuloocular reflex rotates the eye opposite to the forward movement of the head in order to compensate and maintain image stability. This paper investigates the underlying control mechanisms behind the head and eye movements. Using dynamic models for the head and eye, their movements are simulated using potential and optimal control strategies. Simulated model responses are compared with experimentally recorded head and eye movement trajectories. Simulated torques are computed separately using potential and optimal control methods and compared with computed torques from the experimental data.

4.1 Introduction

Neurologists, physiologists and engineers have been interested in modeling and control of the human eye since 1845 with notable studies conducted by Listing [35], Donders [16] and Helmholtz [59]. Specifically, it has been observed that, when the head coordinates are fixed, the oculomotor system chooses just one angle of ocular torsion for any one gaze direction (see Donders [16]). In fact, the axes of rotations of the eye, away from the primary gaze direction, always lie on a fixed plane called the Listing's plane. Since its discovery, the so called Donders' law, has also been applied to the head (see Ceylan et al. [13]), which is mechanically able to rotate torsionally, but which normally adopts just one torsional angle for any one facing direction, see Straumann et. al. [51], Glenn and Vilis [26], Tweed and Vilis [58]. A geometric consequence of the Donders' Law is that the three dimensional vectors that represent the 'rotational vectors'[1] of the head are not spread out in a 3-D volume but instead

[1] See later part of the paper for a precise definition of the 'rotational vector'.

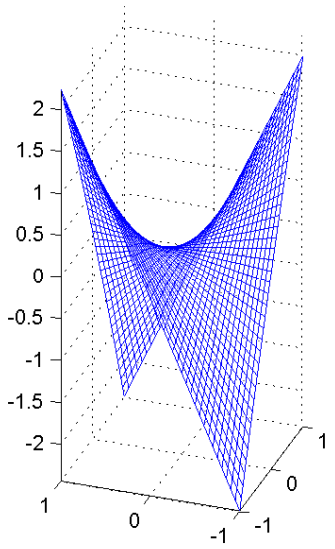

Figure 4.1: One of the six Donders' surfaces introduced in [62] plotted using coordinates from the 'rotational vectors'. The surface is described in (4.7) after scaling m_0 to 1. The three coordinates in the figure are the scaled coordinates $\bar{m}_i = \frac{m_i}{m_0}$ for $i = 1, 2, 3$, where $[m_0, m_1, m_2, m_3]^T$ is the quaternion. The coordinate $\bar{m}_3$ along the vertical line shows the nonzero torsion.

fall in a single two-dimensional surface known as the Donders' surface (see Fig. 4.1). When the head and eye are both allowed to move freely, the situation is a bit more complicated (see [55]). In an attempt to capture a target, the eye violates the Listing's constraint and locks on to the target. In so doing the eye saccades and may move on to an eccentric position, ahead of the head. The eye does not stay in that position but rotates backwards, while the head moves forward, satisfying Donders' constraint, towards the target. As the eye recovers from its initial surge, the vestibulo-ocular reflex guarantees that the image on the retina remains invariant. In other words, the head movements are precisely compensated by the backward movement of the eye. Additionally it has been observed that, in the steady state, when both the head and the eye have momentarily reached a point of immobility, the ocular torsion is once again close to zero. It indicates that at the point of immobility Listing's constraint is satisfied.

During the process of acquiring a target, the head closely follows the eye, while

moving towards the target, and settles on points that satisfy the Donders' constraint. The eye on the other hand settles down (with gaze on the target) satisfying the Listing's constraint relative to the final position of the head. It would appear from Fig. 4.3 that, the eye hops unrestricted to acquire a target and the head follows the eye. In reality, however, the eye moves backwards (with respect to the head coordinate) after acquiring a target, to compensate for the forward movement of the head. In this paper, eye movement is modeled as a tracking problem, where the eye is made to 'backtrack' the forward movement of the head. Tracking is carried out separately using potential and optimal control methods (already introduced in [62] for head movement problems). Application of these methods to the eye tracking problem is new.

Starting from a head trajectory and a stationary point target, we simulate an eye trajectory that captures the target[2] followed by a backward eye movement that compensates for the forward head motion. The head movement trajectory assumes that the Donders' constraint is satisfied for all points on the trajectory. Likewise, the eye movement trajectory is computed assuming that Listing's constraint is satisfied when both eye and the head have reached their terminal points. This trajectory is computed ensuring that, subsequent to the target capture, the orientation of the eye remains invariant with respect to a fixed global coordinate system[3]. The invariance constraint, together with the Listing's constraint to be satisfied at the final time, uniquely fixes the trajectory that the eye needs to track.

Thus, it is easy to see that the problem of acquiring a target fixed in space with respect to a global coordinate system, is equivalent to the problem of trajectory tracking that the eye control system has to satisfy with respect to the moving coordinate system attached to the head. Subsequent to target acquisition, the tracking controls are generated by vestibulo-ocular reflex (VOR) [4], which ensures that the eye is rotated backwards to compensate for the head movement. The effect of VOR on the eye is modeled as an open loop tracking controller (see [38]). In this paper, the head and the eye movements are simulated in three ways (shown as a chart in Fig. 4.2). In the Ist **simulation**, we start with a trajectory of the human head, constructed out of experimentally measured data. The simulated head trajectories are obtained

[2] 'Capturing' ensures that the gaze direction of the eye is pointing towards the target.

[3] A coordinate system attached to the torso.

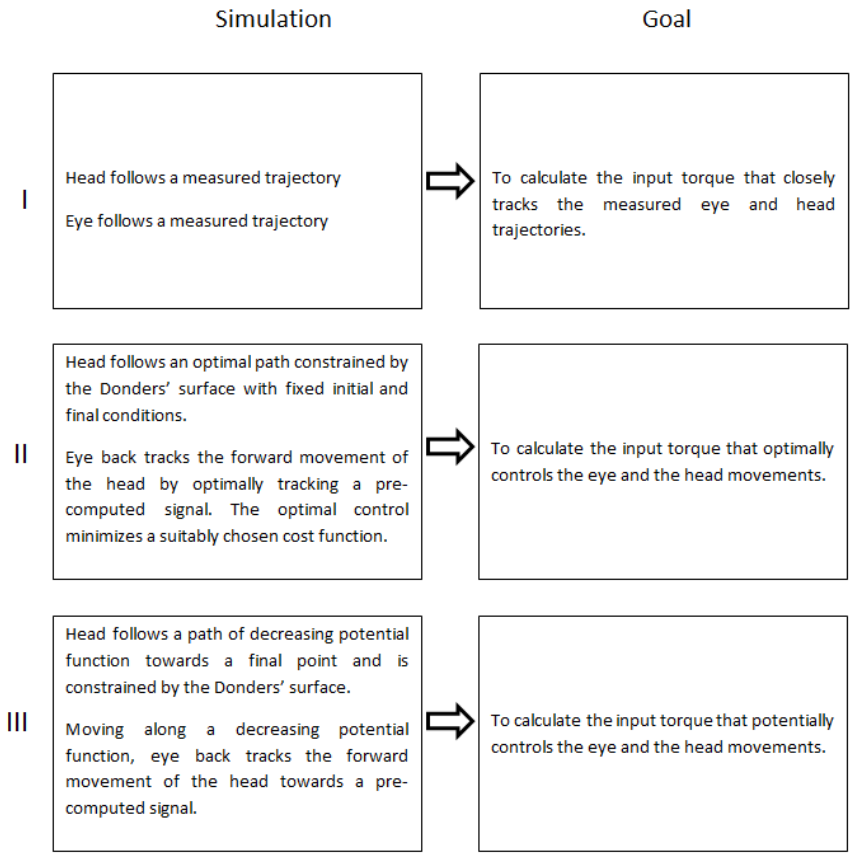

Figure 4.2: Description of the three simulations and their goals

by making the head movement model track this trajectory. In the IInd **simulation**, the trajectory considered in the first simulation, is projected onto the corresponding Donders' surface[4]. We only consider the initial and the final point of the projected trajectory. The simulated head trajectories are obtained by requiring that the model head starts and ends precisely at the prescribed boundary points at a prescribed fixed time, while the control torque applied to the model head, minimizes a cost function. In the IIIrd **simulation**, we choose the boundary points as in the second simulation. We construct a potential function that has its minimum at the terminal point. The control torque applied to the model head is generated using this potential

[4] The Donders' surface parameters of the subjects have been reported in [62].

function. The head rotates along a trajectory that reduces the potential. Adding a suitable damping term, the head is made to settle down at the terminal point. Once

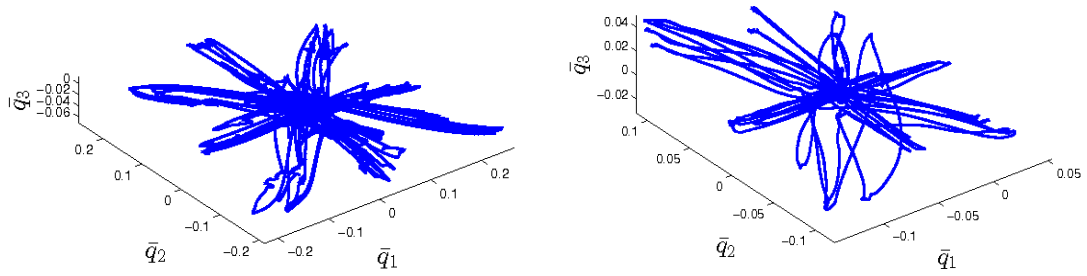

(a) Eye trajectory in head coordinates as recorded experimentally by the laser dots.

(b) Head trajectory in torso coordinates as recorded experimentally by the laser dots.

Figure 4.3: Eye and Head movement manoeuvres for the subject with Donders' surface shown in Fig. 4.1.

the head trajectory is computed, it is easy for the eye movement control system to compute the trajectory it needs to track. For each of the three simulations used to compute the head movement trajectory, we have a corresponding simulation for the eye tracking problem. In the Ist **simulation**, we consider the trajectory of the human eye (corresponding to the head movement trajectory), constructed out of experimentally measured data. The simulated eye trajectories are obtained by making the eye movement model track this trajectory. In the IInd **simulation**, we only consider the final point of the eye movement trajectory from the first method. Preserving the gaze direction, we modify the final point so that the new point satisfies Listing's constraint with respect to the final head position. Using the modified final point and the head trajectory, a new trajectory is calculated for the eye movement control system to track. Eye movement trajectories are simulated by solving an optimal tracking problem, where we minimize a cost function which penalizes for deviations from the required tracking signal. In the IIIrd **simulation**, we construct a tracking signal as we did in the second simulation. The tracking control is simulated by introducing a potential function whose minimum changes in time along the tracking trajectory. We also introduce a suitable damping term into the eye dynamics similar to what was done for the head dynamics.

We end this section discussing the main points of this paper. It is a priori puzzling,

how the final orientation of the eye satisfies Listing's constraint with respect to the final orientation of the head, while maintaining image stability of the target at the same time. This is because, once the target is acquired, eye is not free to move but remains constrained by the head motion. We conjecture in this paper that the eye tracks a computed signal, that depends on the head trajectory and the final target location. We verify this conjecture using experimentally observed data as well as simulating the head/eye complex with optimal and potential control.

An additional goal of this paper is to ascertain if the head/eye complex is primarily controlled as an optimal control problem or the 'brain' uses an underlying potential function in deriving the required control. We choose a specific optimal control problem, and a specific potential function and **compare the simulated head/eye trajectories** with the trajectories constructed from observed experimental data. We also **compare the associated torques** required for the head/eye complex to move along their respective trajectories. The observed features of the head/eye complex fall somewhere in between the optimal and potential control strategies. The details are elaborated in section 4.8.

4.2 Listing's and Donders' Constraints

We assume a global coordinate system fixed with respect to the torso and that the head and eye rotate about the center of this system. Furthermore assume that the head and eye orientations are measured with respect to this coordinate system and that every orientation is a point in **SO(3)**. Without any loss of generality, the head is assumed to be initially located at the identity matrix **I**. Following [22], [43], we describe an 'Axis Angle' coordinate system[5] on **SO(3)** using a coordinate map on $\mathbf{S}^3$ as follows:

$$\rho \; : \; [0, 2\pi] \; \times [0, \pi] \; \times \; \left[-\frac{\pi}{2}, \frac{\pi}{2}\right] \rightarrow \mathbf{S}^3, \tag{4.1}$$

where

$$\rho(\theta, \phi, \alpha) \; = \; \begin{pmatrix} \cos\frac{\phi}{2} \\ \sin\frac{\phi}{2} \; \cos\theta \; \cos\alpha \\ \sin\frac{\phi}{2} \; \sin\theta \; \cos\alpha \\ \sin\frac{\phi}{2} \; \sin\alpha \end{pmatrix}. \tag{4.2}$$

[5] Other choices of coordinate systems are possible. For example in [62], we have used Tait Bryan coordinates.

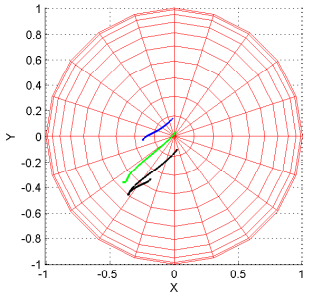

(a) Actual trajectories of head and eye using measured data from one human subject, performing one specific manoeuvre.

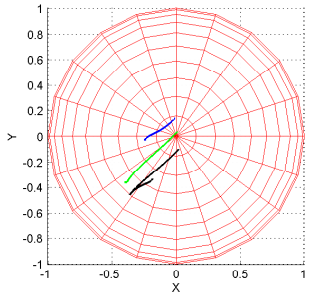

(b) Head and eye are tracking a known signal shown in Fig. 4.4a (Simulation I).

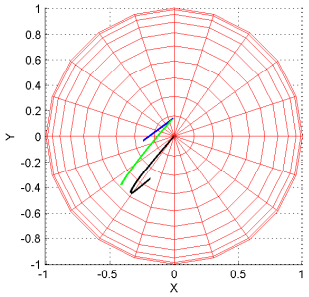

(c) Head moves optimally satisfying boundary constraints, while eye backtracking the head movement (Simulation II).

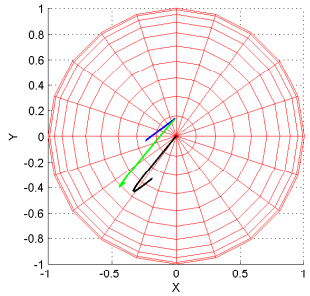

(d) Head moves potentially satisfying boundary constraints, while eye backtracking the head movement (Simulation III).

Figure 4.4: Trajectories of head and eye projected on the gaze (heading) space. Figs. 4.4c and 4.4d show simulated trajectories from dynamic models. Fig. 4.4a shows actual trajectories from experimentally measured data. Fig. 4.4b shows simulated trajectories when the eye and head closely tracks the experimentally measured data. The purpose of computing this simulated trajectory is to estimate the control torque that produces the actual trajectory. The torques on the eye and head are not directly measured. The short (blue) trajectory on top is the head movement. The green trajectory in the middle is the eye movement with respect to a fixed global coordinate. The bottom (black) trajectory corresponds to the eye movement with respect to the moving head coordinates. All three black trajectories clearly show the backward movement of the eye corresponding to the forward movement of the head.

Next we consider the map **rot** from [43], between $\mathbf{S}^3$ and $\mathbf{SO(3)}$ given by

$$\text{rot} \ : \ \mathbf{S}^3 \rightarrow \mathbf{SO(3)}. \tag{4.3}$$

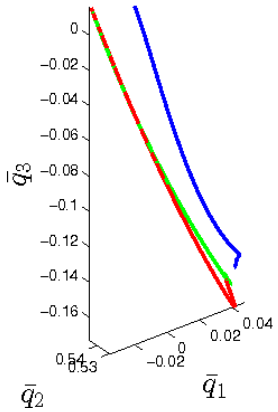

(a) Eye movement trajectories with respect to the torso.

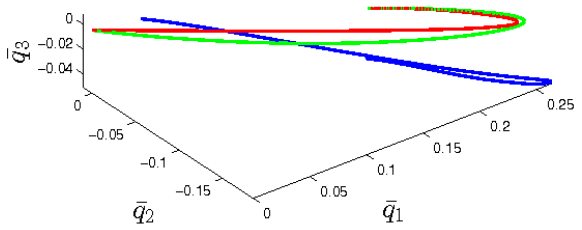

(b) Eye movement trajectories with respect to the head.

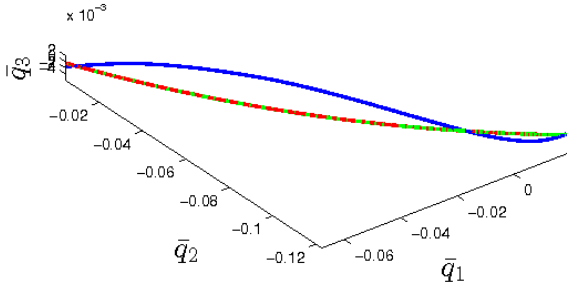

(c) Head movement trajectories with respect to the torso.

Figure 4.5: Actual and simulated head and eye trajectories using scaled coordinates $\bar{q}_i = \frac{q_i}{q_0}$ for $i = 1, 2, 3$, where $[q_0, q_1, q_2, q_3]^T$ is the unit quaternion. These coordinates are precisely the coordinates of the 'rotational vector'. The blue lines are the actual trajectories. The red and the green lines are trajectories from the 'Simulation II' (optimal) and 'Simulation III' (potential) respectively. Note that the head movement trajectories under the influence of optimal and potential control are surprisingly close, but differs from the actual trajectory which satisfies the Donders' constraint, only approximately.

The image of the composite map "rot $\circ\, \rho(\theta, \phi, \alpha)$" is a rotation matrix which rotates a vector in $\mathbf{R}^3$ around the axis

$$\tan\frac{\phi}{2}\ (\cos\theta\ \cos\alpha,\ \ \sin\theta\ \cos\alpha,\ \ \sin\alpha)^T \tag{4.4}$$

by a counterclockwise angle ϕ. Every point in $\mathbf{S}^3$ is considered as a unit quaternion [48]. The map **rot** is a $2-1$ map and every quaternion q and $-q$ are mapped to the same rotation matrix in $\mathbf{SO(3)}$. The angle parameter vector (θ, ϕ, α) can therefore

be viewed as a coordinate on **SO(3)**. The vector (4.4) is called the *'rotational vector'*.

Donders' law states that for head rotation, the axes of rotations (4.4), lie in a surface that goes by the name **Donders' Surface** [22]. In order to describe this surface, the **torsion** angle parameter α is often written as a function of the other two parameters θ and ϕ. When the torsion is zero, i.e. when $\alpha = 0$, the Donders' surface reduces to a plane that goes by the name **Listing's Plane** [43]. When the head is restricted to be fixed, orientations of the eye of an individual lie on the Listing's plane. When head is free to move, which is the case described in this paper, eye orientations are not constrained by the Listing's plane. However when the eye has fixated on a target and when both eye and head reaches a point of immobility, Listing's constraint is once again satisfied.

When a point target is introduced in the visual space, eye rotates to fixate on the target as quickly as possible. We assume that this motion takes place in $\mathbf{S}^3$. Let $e = [e_0, e_1, e_2, e_3]^T$ be the coordinates (unit quaternion coordinates) of the target with respect to a fixed global coordinate system (assumed attached to the torso in this paper). Furthermore, we assume that $m(t) = [m_0(t), m_1(t), m_2(t), m_3(t)]^T$ are the unit quaternion coordinates of the moving head, with respect to the same global coordinate system. Finally, we assume that at $t = 1$, the head comes to a stop and the eye is fixated on the target. At this time, the eye satisfies Listing's constraint with respect to the head. The following Lemma describes the constraint between $m(1)$ and e dictated by the Listing's constraint:

Lemma I: A necessary and sufficient condition for the eye to satisfy Listing's constraint with respect to the head is

$$e_0 m_3(1) + e_2 m_1(1) = e_1 m_2(1) + e_3 m_0(1). \tag{4.5}$$

Proof of lemma I: The unit quaternion coordinates of the eye with respect to the moving head coordinates is given by

$$[m_0(t), -m_1(t), -m_2(t), -m_3(t)] \bullet [e_0, e_1, e_2, e_3] \tag{4.6}$$

where $\bullet$ denotes quaternion multiplication (see [2] for a definition). For the eye to

satisfy Listing's constraint with respect to the head, the last coordinate of the product in (4.6) must be zero at $t = 1$. The condition (4.5) easily follows. □

Of course, at all time 't', the head coordinates satisfy an additional constraint imposed by Donders' law. In this paper we assume that the Donders' surface is quadratic[6] and is of the form

$$m_3 m_0 \;=\; h_0 m_0^2 + 2h_1 m_1 m_0 + 2h_2 m_2 m_0 + h_{11} m_1^2 + h_{22} m_2^2 + 2h_{12} m_1 m_2, \tag{4.7}$$

where the parameters h_* have been pre computed and are assumed known.

Remark I: We would assume that as soon as the presence of a target is detected, the final head orientation is anticipated (and this information is available to both the 'head' and 'eye' controllers.). The coordinates $e \;=\; [e_0, e_1, e_2, e_3]$ satisfying the target gaze direction and the Listing's constraint (4.5) are easily computed. If the head follows a trajectory $m(t)$, the eye has to follow the trajectory $\xi(t) \;=\; m(t)^{-1} \bullet e$ in order to maintain 'orientation stability' of image. It would imply that the eye controller has to track the signal $\xi(t)$[7].

Remark II: Eye movement data (see Fig. 4.3a) was recorded in conjunction with head movement (see Fig. 4.3b) and for complete details we would refer to Glasauer et. al. [25] and Kremmyda et. al. [33]. Data was recorded from 6 subjects, aged 25 to 38 years with no known neurological or orthopedic disorders. For $3D$ eye movement recordings, a dual search coil was used on the left eye (Skalar, Delft, The Netherlands) and for the 3D head movements, two coils mounted on a head ring at 90 degrees angle between them was used. Both head and eye coil measured absolute position in space. Therefore, when the head was allowed to move, the eye coil recorded gaze (combined eye and head) movements. The subjects were seated in complete darkness inside a magnetic field and were instructed to follow a laser dot. Subjects had to follow the target with a combination of natural eye and head movements. The laser dot jumped randomly between the center and eight peripheral positions, so that each final position is reached from a different initial position (See Fig. 4.3 for the laser dot

[6] These surfaces were already introduced in [62]. There are a total of six surfaces coming from six different subjects.

[7] The black trajectory in Figs. 4.6b, 4.6d, 4.6f is the signal $\xi(t)$. The figure illustrates alternate control strategies employed by the eye controller to track this signal

Table 4.1: For each subject, maximum absolute value of the Donders' error, in radians, are displayed by taking average over all the head trajectories.

subjects	actual	optimal	potential
1	0.0226	0.0000	0.0001
2	0.0177	0.0000	0.0002
3	0.0217	0.0000	0.0010
4	0.0150	0.0000	0.0008
5	0.0270	0.0000	0.0001
6	0.0093	0.0000	0.0000

movements corresponding to the eye and head. The subject in this figure has the Donders' surface sketched in Fig. 4.1).

For the Head and Eye movement data from six subjects, we display in Table 4.1 the extent to which Donders' law is satisfied by the actual head movement trajectories, (see the first column of the Table), and in Table 4.2 the extent to which Listing's law is satisfied by the final eye orientation, (see the first column of the Table), when the subject has acquired the target and the eye and the head have come to rest. The point of showing the two tables is to emphasize that the two physiological constraints stemming from Donders and Listing are closely supported by observed data. In the other columns of the two tables, we show that the optimal and the potential controllers that we have implemented for the Head/Eye complex (to be described later), the two physiological constraints are closely enforced.

4.3 Head/Eye Movement Dynamics

The head and eye movement trajectories are simulated using a dynamical system, constructed from an appropriate Lagrangian formulation, the main ideas of which are already sketched in [22], [43]. We rewrite the main steps using coordinates (θ, ϕ, α) from section 4.2.

Let $q(\theta, \phi, \alpha)$ be a parametrization of the manifold $\mathbf{S}^3$. We define Riemannian

Table 4.2: For each subject, absolute value of the final Listing's error, in radians, are displayed by taking average over all the eye trajectories.

subjects	actual	optimal	potential
1	0.0826	0.0000	0.0007
2	0.0200	0.0000	0.0003
3	0.0497	0.0000	0.0010
4	0.0533	0.0000	0.0012
5	0.0478	0.0000	0.0006
6	0.0366	0.0000	0.0001

metric on $\mathbf{S}^3$ given by

$$G \;=\; \begin{pmatrix} q_\theta \cdot q_\theta & q_\theta \cdot q_\phi & q_\theta \cdot q_\alpha \\ q_\phi \cdot q_\theta & q_\phi \cdot q_\phi & q_\phi \cdot q_\alpha \\ q_\alpha \cdot q_\theta & q_\alpha \cdot q_\phi & q_\alpha \cdot q_\alpha \end{pmatrix}, \tag{4.8}$$

where $q_\gamma \;=\; \frac{\partial q}{\partial \gamma}$ and 'dot' in (4.8) is the vector dot product. Let us define $X \;=\; (\theta, \phi, \alpha)^T$ to be the vector of angle variables. As in [43], we would define the Kinetic Energy[8] KE as

$$KE \;=\; \frac{1}{2}\, \dot{X}^T G \dot{X}. \tag{4.9}$$

If the potential energy is represented by V, the Lagrangian of the head movement system can be written as

$$L \;=\; KE \;-\; V. \tag{4.10}$$

The equation of motion on the Donders' surface, using the Euler Lagrange equation can now be described as

$$\frac{d}{dt}\frac{\partial L}{\partial \dot{\gamma}} \;-\; \frac{\partial L}{\partial \gamma} \;=\; \tau_\gamma \tag{4.11}$$

where γ can be the angle variable θ, ϕ or α and where τ_γ is the generalized torque

[8] The head is assumed to be a perfect sphere with mass distributed uniformly. The rotation is assumed to be about the center of the sphere. In this case, the usual definition of KE = $\omega^T\, I\, \omega$, documented in Physics (see [15]), differs from the definition (4.9) by a constant scale factor, where ω is the angular velocity vector and I is the diagonal moment of inertia matrix. The parameter I for eye and head are chosen to be different.

input (to be viewed as the control input) to the system. The resulting equations of motion can be expressed as

$$G\ddot{X} \ + \ \dot{G}\dot{X} \ - \ \frac{1}{2}\dot{X}^T\nabla_X G\,\dot{X} \ + \nabla_X V \ = \ \Gamma \tag{4.12}$$

where $\Gamma \ = \ (\tau_\theta \quad \tau_\phi \quad \tau_\alpha)^T$ and where ∇_X is the gradient operator with respect to X defined as

$$\nabla_X \ = \ \left(\frac{\partial}{\partial\theta}, \frac{\partial}{\partial\phi}, \frac{\partial}{\partial\alpha}\right). \tag{4.13}$$

Remark III: In this paper, the potential energy term V is assumed to be identically zero, when we are looking at optimal control problems. On the other hand, when the control is potentially driven (as in section 4.5), the potential energy term V is present. We also add a suitable damping term to the equations of motion (4.12), in order to stabilize the state vector at the point where V is minimum.

4.4 Tracking and Optimal Rotation of Human Head and Eye

We begin this section, recalling the Remark I made in section 4.2. We had remarked that in order for the 'eye orientation' to satisfy Listing's constraint when the head and eye comes to a stop while the eye is stably gazing at the target, the eye has to track a pre-computed trajectory (denoted by $\xi(t)$ in the remark). We now describe three simulation scenarios, already introduced in Fig. 4.2, with the goal of computing the head and eye controllers using optimal and potential control. The first simulation is meant to estimate the control signals (torques) for the measured head and eye movements, which we subsequently compare with the optimal and potential control.

4.4.1 Simulation I: Head and Eye Tracking an observed trajectory

Assume that the dynamics of the head and eye are given by

$$G\ddot{X} \ + \ \dot{G}\dot{X} \ - \ \frac{1}{2}\dot{X}^T\nabla_X G\,\dot{X} \ = \ \Gamma. \tag{4.14}$$

We would like to rewrite the dynamics (4.14) as

$$\ddot{X} \ + \ G^{-1}\dot{G}\dot{X} \ - \ \frac{1}{2}G^{-1}\dot{X}^T\nabla_X G\,\dot{X} \ = \ \Gamma_1, \tag{4.15}$$

where

$$\Gamma_1 \;=\; G^{-1}\Gamma. \tag{4.16}$$

For both, the head and the eye, we consider a cost function given by

$$J = \int_0^1 \frac{\alpha}{2}\,\Gamma_1^T\Gamma_1 + \frac{\beta}{2}\,C^TC + p^T\left(F - \ddot{X}\right)\,dt \tag{4.17}$$

where $\ddot{X} = F$ is the equations of motion (4.15), $C = (A(t) - X)$ and $A(t)$ is the trajectory to track. The trajectory $A(t)$ has been obtained from measured head and eye trajectory data. The parameters for the cost function (4.17) are chosen as follows: $\alpha = 2,\ \beta = 2 \times 10^6$ (for the head and the eye dynamics). They are chosen to obtain a near perfect tracking. The initial and final orientations of the head and eye are chosen to match the corresponding measured orientations. Boundary conditions are prescribed by choosing the vector $(X(0), \dot{X}(0), X(1), \dot{X}(1))$.

The Hamiltonian [43] for this problem is defined as

$$H = \frac{\alpha}{2}\,\Gamma_1^T\Gamma_1 + \frac{\beta}{2}\,C^TC + p^TF. \tag{4.18}$$

Using this notation, we write

$$J = \int_0^1 \left[H - p^T\ddot{X}\right]\,dt. \tag{4.19}$$

Applying the principle of variation, we obtain the following set of Hamilton's equations.

$$\ddot{X} = \frac{\partial H}{\partial p} = F;\;\; \ddot{p} = \frac{\partial H}{\partial X} - \frac{d}{dt}\left(\frac{\partial H}{\partial \dot{X}}\right);\;\; \Gamma_1 = -\frac{1}{\alpha}p, \tag{4.20}$$

where Γ_1 is obtained by setting $\frac{\partial H}{\partial \Gamma_1} = 0$ and the optimal control Γ is obtained from (4.16) as

$$\Gamma \;=\; -\frac{1}{\alpha}Gp. \tag{4.21}$$

Remark IV: We would like to remark that the optimal control problem (4.15), (4.17)

is scale invariant, in the sense that if G is scaled by a constant scale factor υ, the dynamics (4.15) and the cost function (4.17) remain unaltered. Hence the relative weights of control energy and tracking error in the cost function (4.17) does not change, as well. The model can therefore be used for both, the eye and the head, which differ from each other by a scale factor in G.

Remark V: In our experiments, the eye and head trajectories are measured but the torque inputs are not measured. Via this simulation, we synthesize the control input using our dynamic model, that closely tracks the measured trajectories.

4.4.2 Simulation II: Head and Eye are optimally controlled, eye reverse tracking the head movement

As in Simulation I, we continue to assume that the dynamics of the head and eye are given by (4.15). The cost function for the head is given by

$$J_H = \int_0^1 \frac{\alpha}{2}\,\Gamma_1^T\Gamma_1 + p^T\left(F - \ddot{X}\right) + \lambda^T D + \frac{1}{2}\,\dot{\lambda}^T\epsilon\,\dot{\lambda}\;dt, \tag{4.22}$$

and for the eye is given by

$$J_E = \int_0^1 \frac{\alpha}{2}\,\Gamma_1^T\Gamma_1 + \frac{\beta}{2}\,C^TC + p^T\left(F - \ddot{X}\right)\;dt, \tag{4.23}$$

where $\ddot{X} = F$ is the equations of motion (4.15), $C = (A(t) - X)$ and $A(t)$ is the trajectory to track[9]. $D(X) = 0$ constrains the state X to stay on the Donders' surface [62], [22] and the parameter λ is the Lagrange multiplier. Finally, the parameter ϵ decides on the level of smoothness of the Lagrange multiplier. The parameters for the cost functions (4.22), (4.23) are chosen as follows: $\alpha = 2$, $\epsilon = 2 \times 10^{-8}$ (for the head dynamics); $\alpha = 2$, $\beta = 20,000$ (for the eye dynamics). Although the choice of the parameter α does not affect the head dynamics, the ratio of α and β affects the eye dynamics and emphasizes the relative importance between the tracking error in comparison to the magnitude of the torque.

The initial and final orientations of the head and eye are chosen as follows. For

[9] See Remark I where $A(t)$ has been calculated using 'head trajectory' and the 'target position'.

the head, the measured orientations at the end points are projected onto the Donders' surface. The projected end points are chosen as the boundary conditions for our simulation. For the eye, the initial orientation coincides with the 'straight gaze direction', i.e. the eye looking straight with respect to the head coordinates. The final orientation of the eye satisfies Listing's constraint with respect to the final orientation of the head while gazing directly at the target. Boundary conditions are prescribed by choosing the vector $(X(0), \dot{X}(0), X(1), \dot{X}(1))$.

The Hamiltonian [43] for the head is defined as

$$H_H = \frac{\alpha}{2}\,\Gamma_1^T\Gamma_1 + p^T F + \lambda^T D. \tag{4.24}$$

Using this notation, we write

$$J = \int_0^1 \left[H_H - p^T\ddot{X} + \frac{1}{2}\,\dot{\lambda}^T\epsilon\,\dot{\lambda} \right]\, dt. \tag{4.25}$$

Applying the principle of variation, we obtain the following set of Hamilton's equations.

$$\begin{aligned} \ddot{X} &= \frac{\partial H_H}{\partial p} = F;\;\; \ddot{p} = \frac{\partial H_H}{\partial X} - \frac{d}{dt}\left(\frac{\partial H_H}{\partial \dot{X}}\right) \\ \ddot{\lambda} &= \epsilon^{-1}\frac{\partial H_H}{\partial \lambda};\;\; \Gamma_1 = -\frac{1}{\alpha}\,p, \end{aligned} \tag{4.26}$$

where the optimal control Γ_1 is obtained by setting $\frac{\partial H_H}{\partial \Gamma_1} = 0$. As before, the optimal control Γ is obtained from (4.16) and is given by (4.21).

The Hamiltonian [43] for the eye is same as (4.18) and the corresponding Hamilton's equations are given by (4.20). Finally, the optimal control Γ is given by (4.21).

4.5 Tracking with Potential Control in Human Head and Eye

Instead of minimizing a cost function (4.17), (4.22), (4.23), we show in this section that the head and the eye rotations can be controlled using a potential function and an added damping term. The potential function is described (see [62]) as follows

$$V(\theta, \phi, \alpha) \;=\; A\,(1 - |\rho(\theta, \phi, \alpha).\rho_0|) \tag{4.27}$$

where A is a constant parameter, ρ_0 is a fixed unit quaternion, and $\rho(\theta, \phi, \alpha).\rho_0$ represent the dot product of two vectors in $\mathbb{R}^4$. It can be observed that the minima occurs at $\rho = \rho_0$ or $\rho = -\rho_0$. Both of these minima correspond to a unique point on $SO(3)$ via the map 'rot' introduced in (4.3). The parameter ρ_0 can be constant or can vary in time.

A damping term is added externally using the generalized torque input Γ, the goal of which is to dampen the movement so that it comes to a rest at the desired pointing direction and orientation, described by ρ_0. We consider a damping term described by:

$$\Gamma_1 \;=\; -c\,\dot{X}, \tag{4.28}$$

where c is an arbitrary constant. The obtained motion equation (4.12) is given by

$$\ddot{X} \;+\; (G^{-1}\dot{G} \;+\; c)\,\dot{X} \;-\; \frac{1}{2}G^{-1}\dot{X}^T\nabla_X G\,\dot{X} \;+G^{-1}\nabla_X V \;= 0, \tag{4.29}$$

which is of the form (4.15), where

$$\Gamma_1 \;=\; -c\dot{X} - G^{-1}\nabla_X V. \tag{4.30}$$

The generalized torque vector $\Gamma = G\Gamma_1$, where Γ_1 is of the form (4.30), has already been introduced in [62], and would be called 'Potential Control'.

Remark VI: As already observed in Remark IV, we note that the motion equation (4.29) remains unchanged when G and V are both scaled by a fixed scale factor. Thus, the motion equation (4.29) can be used for both, the eye and the head, which only differ from each other by a scale factor in G. The two systems can, therefore be identically controlled by scaling V by the same scale factor.

4.5.1 Simulation III: Head and Eye are potentially controlled, eye reverse tracking the head movement

The dynamics of the head and the eye are given by (4.29), where the chosen potential function is of the form (4.27). As in Simulation II, the goal of the head control system is to drive the head from an initial orientation to a final orientation. However, as opposed to minimizing a cost function, the control drives the state towards

smaller values of the potential function (4.27). We choose ρ_0 to coincide with the final orientation of the head.

The goal of the eye controller is to track a signal $A(t)$, which was introduced in Simulation II. It was described in Remark I that the tracking signal is derived from the head movement trajectory and from the location of the target. In order to track a signal $A(t)$ using a potential function, we choose $\rho_0(t) = A(t)$ and the potential function is given by

$$V(\theta, \phi, \alpha, t) \;=\; A\,(1 - |\rho(\theta, \phi, \alpha).\rho_0(t)|). \tag{4.31}$$

It is easy to see that with the choice of the potential function (4.31), the orientation of the eye tracks the given target signal $A(t)$, provided that the constant A is chosen sufficiently large. In our simulation the parameters for the head system are chosen as $A = 40$, $c = 12$, and the parameters for the eye system are chosen as $A = 500$, $c = 26$.

4.6 Simulation Details

In order to carry out the simulations, the recorded data displayed in Figs. 4.3a and 4.3b have to be split into trajectories. The raw data set consist of many head/eye movements between 9 target points. In order to isolate trajectory segments from the observed raw data, we proceed as follows.

4.6.1 Isolation of trajectory segments

The first step of the data analysis is to low-pass filter the data set to reduce the sampling noise. Since the data has a sampling rate of 1024Hz, the low pass filter is chosen to have a cut-off frequency of 10Hz (for the 6 dB point below the pass band value) with a filter order of 1000. We now require to identify the initial and final positions for the potential trajectory segments. This is done by considering both, the eye and the head data. We start the trajectory segment from a position where the eye is closest to gazing straight with respect to the head fixed coordinate system and end at a position where the head shows maximum deviation from the straight heading with no torsion with respect to the torso fixed coordinate system. In order to achieve this while making sure that the trajectory segments chosen actually represent

the required characteristics and not noise, the segmentation process starts at points where the eye data crosses a certain deviation threshold, indicated by a rectangular red box in Fig. 4.11, with respect to the head fixed coordinate system. The size of the box depends on the data set and is manually determined. For each of the threshold crossing time points, we move back in time on the eye data to arrive at the point where the eye first shows a local minimum deviation with respect to the head. This point represents the initial position for the eye trajectory segment and the corresponding head position represent the initial position for the head trajectory segment. In order to get the final position for the eye and the head, we start from the head position that corresponds to the eye threshold crossing point and move forward in time on the head data to arrive at the point where the head first shows a local maximum deviation with respect to the torso. This point represents the final position for the head trajectory segment and the corresponding eye position represents the final position for the eye trajectory segment. The trajectory segments obtained this way for all the six data sets are visually inspected to remove any trajectory segments that do not represent the required characteristics but are still captured by the automated process.

4.6.2 Simulation Details to Solve the Two Point Boundary Value Problems

In order to solve the Two Point Boundary Value Problems of the kind introduced in (4.20) and (4.26) we discretize the equations using Comsol-Multiphysics finite element software [64], widely used in the computational community to solve both, initial and boundary value problems. The software automatically generates Galerkin finite element approximation [8] for a specific PDE equation, once the problem is entered in its weak or strong formulation. The Comsol software facilitates the solution of multi physics nonlinear coupled problem, where the Jacobian in the Newton iteration scheme is evaluated through automatic differentiation [28]. The corresponding linearized system is then solved using a direct or iterative solver.

The equation system (4.20) and (4.26) are discretized and solved as a boundary value problem in time. The time domain $[0, 1]$ has been treated as a line segment and divided in 100 elements, and for each element we have chosen a quadratic Lagrange finite element approximation. This corresponds to 201 degree of freedoms (dofs) to

be solved for each equation, for a total of

$$N = (201) \times \text{number of equations}$$

unknowns for each nonlinear iteration where the number of equations is 6 for all the cases except for the head simulation using optimal control for which it is 7. The resulting system is solved using a direct solver, since the total number of unknowns N never exceeded 1407.

4.7 Results

Recorded data from 6 subjects have been used to plot the head and eye movement trajectories, when the Head/Eye complex has the task of acquiring a point target fixed in space with the eye starting from an initial primary position. The trajectories of the head and eye are projected on the heading/gaze space and plotted in Fig. 4.4. The trajectories are also plotted in Fig. 4.5 on the 'rotational vector' space. In general, the eye trajectories are plotted with respect to, both, the fixed torso coordinates and the moving head coordinates. From the eye trajectories in Fig. 4.4 we infer that the effect of head movement is compensated by the back tracking movement of the eye. Fig. 4.5 is less informative but shows that the effect of optimal and potential control on the head trajectories, and to some extent on the eye trajectories, are surprisingly close. The simulated trajectories are somewhat different from the actual trajectories observed and there are possibly two reasons for this. The first is that the Donders' and Listing's constraints are not tightly satisfied by the actual trajectory. This is evident from Tables 4.1 and 4.2, where we observe that the eye can deviate from the Listing's constraint by up to 2 degrees. The second is that the parameters of the optimal and potential controllers need 'fine tuning'. Such an inverse optimal/potential control problem has not been looked at, in this paper.

One of the key finding of this paper is evident in Figs. 4.6a and 4.6b, where the eye trajectory is shown to track a computed trajectory (shown in black). Additionally we illustrate the point that the eye tracking is achieved in an optimal control setting by minimizing a cost function (4.23) and the 'optimal eye trajectory' is displayed in Figs. 4.6c and 4.6d. The eye tracking is also achieved in a potential control setting by choosing a potential function (4.31) and the 'potential eye trajectory' is displayed

in Figs. 4.6e and 4.6f.

For each of the three simulations, the eye tracking error is plotted in Fig. 4.7. Error is displayed in 'blue' by computing the angle between corresponding unit quaternion vectors and in 'red' by computing the angle between unit gaze vectors. While looking at this figure, one would ask the following two questions. How quickly does the error plot go to zero? How stable is the error plot in the neighborhood of zero? From Fig. 4.7c it is evident that the potential eye trajectory goes to zero 'rapidly' but it overshoots immediately. On the other hand, we observe from Fig. 4.7b that the optimal eye trajectory goes to zero 'relatively slow'. The tracking error for the measured eye trajectory, displayed in Fig. 4.7a, show that the error goes to zero 'rapidly' as well, and is quite stable. Although, Fig. 4.7 displays the error plot for one subject performing one manoeuvre, this picture has been generalized in Table 4.3 by cumulating the data over all the manoeuvres. The table shows that for each of the six subjects, the potential eye trajectory goes to zero 'most rapidly'. The table also introduces and displays a stability factor and claims that the optimal eye trajectory is 'most stable', for each of the six subjects. The actual eye trajectories lie in between the optimal and the potential.

Head trajectories were simulated and studied in [62] and Fig 4.8 describes how rapidly does the head reaches its final end point. The figure displays surprising similarity between the actual and the optimal trajectories in comparison to the actual and potential trajectories.

Finally in Figs. 4.9, 4.10 and 4.12, the actual torque input to the head/eye complex is compared with the simulated inputs by assuming, separately, that the optimal and the potential control schemes are implemented.

4.8 Discussions

Recorded data shows that during the process of capturing a point target, fixed in space, human head/eye coordinates their movements. In order to stabilize the image on the retina, the eye has to backtrack the forward movement of the head. By constructing a dynamic model, we show in this paper that the backtracking movement of the eye can be reconstructed essentially using two alternate forms of control strategy, introduced earlier by the authors [22], [62] and [43], for eye and head movement prob-

Table 4.3: This table cumulates the data in Fig. 4.7 over multiple subjects and manoeuvres. The number α under 'Envelope' refers to the interval $[0, \alpha]$. The six rows for each number under 'Envelope', correspond to the data collected from six different subjects, indexed from 1 to 6. The number under 'Time' refers to the first time the error in Fig. 4.7 enters the corresponding envelope, averaged over multiple manoeuvres. The number under the 'Stability Factor' is the area under the 'error curve' in Fig. 4.7 in the interval $[\tau, 1]$ (averaged over the interval and over the multiple manoeuvres), where τ is the corresponding 'Time' entry.

Envelope	Actual		Optimal		Potential	
	Time	Stability Factor	Time	Stability Factor	Time	Stability Factor
0.05	0.1835	0.0150	0.2339	0.0062	0.1503	0.0124
	0.1390	0.0069	0.1024	0.0035	0.0614	0.0104
	0.1760	0.0082	0.1449	0.0048	0.0886	0.0124
	0.1196	0.0084	0.2344	0.0061	0.1496	0.0115
	0.1627	0.0155	0.2340	0.0060	0.1470	0.0127
	0.0939	0.0062	0.0933	0.0025	0.0617	0.0038
0.035	0.2310	0.0134	0.2532	0.0054	0.1613	0.0121
	0.1667	0.0056	0.1181	0.0029	0.0700	0.0102
	0.2040	0.0069	0.1689	0.0037	0.1023	0.0120
	0.1319	0.0080	0.2574	0.0050	0.1615	0.0111
	0.2183	0.0133	0.2570	0.0050	0.1593	0.0124
	0.1222	0.0049	0.1017	0.0021	0.0661	0.0036
0.025	0.3406	0.0102	0.2677	0.0049	0.1703	0.0119
	0.1824	0.0048	0.1357	0.0024	0.1119	0.0092
	0.2414	0.0056	0.1874	0.0032	0.1143	0.0118
	0.1496	0.0075	0.2763	0.0045	0.1719	0.0109
	0.3237	0.0108	0.2747	0.0045	0.1690	0.0122
	0.1344	0.0046	0.1094	0.0018	0.0700	0.0035

lems separately. Eye and head movement data from six subjects have been analyzed in detail and the results are cumulated to derive conclusions reported in this paper. Additionally, for the purpose of illustration, simulation results from one subject has been displayed in various figures presented.

In Fig. 4.4, the head and the eye trajectories have been displayed after projecting them onto the heading/gaze space. The actual and the simulated head/eye movements clearly show that the eye backtracks the forward movement of the head. In Fig. 4.5, the head and the eye trajectories are displayed on the 'rotational vector' space. This figure illustrates the point that, as a trajectory there is a surprising

closeness between the simulated trajectories under the two different control strategies. However, the simulated trajectories are far from the actual trajectory, indicating the fact that the control strategies require 'fine tuning'.

One of the main result of this paper is illustrated in Fig. 4.6. In the beginning of the paper, we had conjectured that the eye has to track a computed signal (in the head coordinate), based on the head movement and the location of the point target. This is required, in order for the head and eye to satisfy respectively the Donders' and Listing's constraints and for the image to be stabilized on the retina once the eye captures the target. The display on Fig. 4.6b shows the validity of this conjecture, by displaying the computed signal to be tracked (in black). The actual eye movement trajectory (in blue) shows the tracking movement of the eye. In Figs. 4.6d and 4.6f the tracking movements of the eye are displayed under optimal and potential controls, respectively. The tracking errors are displayed in Fig. 4.7 and illustrates the point that the actual tracking errors drop to zero faster than the error under optimal control, and about the same time as the potential control. Unfortunately, the error under potential control, overshoots and settles down 'rather slowly'. The error plots, between the current and the final head orientation, in Fig. 4.8 show surprising similarity between actual and the optimal head movements. Under potential control, the head moves rapidly in the beginning and slows down later, towards the end.

In Figs. 4.9 and 4.10, the torque vectors are plotted for the head and the eye movements respectively. We compute the torques required for the actual head/eye movements to follow the observed trajectories. We compute the torques required when the head/eye has to follow the optimal control strategy and the potential control strategy. As expected, the potential control takes higher values compared to the optimal control. For head movement control, closer to the end point, the potential control tapers off to zero whereas the optimal control continues to maintain high values. The actual torque, reconstructed from the data, does not taper off to zero for the head movement control, either. In this sense, the head movements are qualitatively similar to the optimal control strategy. All torques taper off to zero for the eye movement but the torque profile for the optimal torque goes to zero slower in comparison to the actual torque and torque computed under potential control. Potential control and the actual control, both taper off to zero around the same time for eye

movements, even though the potential control start from a higher magnitude. In this sense, the actual controls in eye movements are qualitatively similar to the controls obtained under the potential control strategy.

From the cumulative data recorded in Fig. 4.12, we infer quite expectedly that the optimal controllers correspond to control torques of least energy for every subject cumulated over multiple manoeuvres. The potential control invariably has a higher L^2 norm, indicating perhaps the price one has to pay for a control strategy that is simple to implement. The reconstructed actual control from simulation I, always has an energy level substantially higher than the optimal control, indicating perhaps that the human eye and the head controllers are far from optimal, in terms of the energy of the control signal.

From Table 4.3 we observe that, by and large, the potential controller is quick to capture the target. It is however unable to retain the target 'stably' and as a result the 'stability factor'[10] is not that small. The optimal controller, on the other hand, is relatively slow in capturing the target but has a small 'stability factor', indicating that the target once captured is retained well. The actual eye movements fall somewhere in between. For the parameters chosen in this paper, their ability to capture the target is never faster than the potential controller, and the stability factor is always higher than the optimal controller. It is interesting to note that in some cases, the optimal controller captures the eye faster than the actual eye movement, and also stabilizes the target better.

4.9 Conclusion

This paper extends our earlier study on head movement control problem [62] where, either the head movements are actuated by a controller which minimizes a suitably chosen cost function (optimal control) or the control signals drive the head towards a path that reduces a suitably chosen potential function (potential control). We apply the optimal and potential control strategies to both, the head and the eye movement problems. An important distinction between potential and optimal control strategies is that, potential controller drives the system-states rapidly in the beginning followed by small changes towards the end. On the other hand, an optimal controller drives

[10] A smaller stability factor indicates that the target is more stable.

the system-states somewhat evenly throughout the entire time of actuation. A consequence of this qualitative difference between a potential and an optimal controller is that, the applied torques during potential control are large initially and taper off to small values subsequently during actuation. On the other hand, the control torques during optimal control maintain large values, most of the time, during entire period of actuation. On the basis of the this criterion, we find that the actual head movement has the qualitative features of an optimal head movement.

From the point of view of 'how rapidly the tracking error goes to zero' and 'how stable the target is, once it is acquired', the actual eye movement falls somewhere in between optimal and the potential control schemes discussed in this paper. Further work is required to explain the tracking control strategy implemented by the 'human brain' for the purpose of target acquisition and stability.

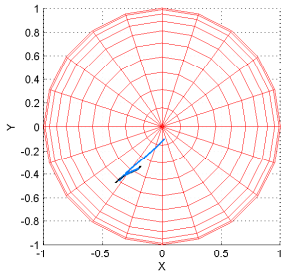

(a) Both Eye and Head are closely following a measured trajectory from a human subject. Note that the actual eye trajectory (blue curve) is surprisingly close to the computed trajectory (black curve) that the eye is expected to track.

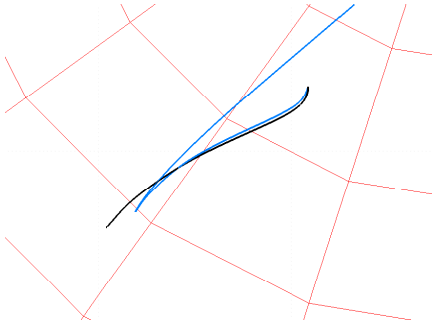

(b) Both Eye and Head are closely following a measured trajectory from a human subject (closeup view of Fig. 4.6a).

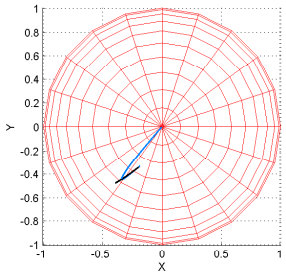

(c) Eye backtracking while the head moves optimally between initial and final point of a measured trajectory from a human subject.

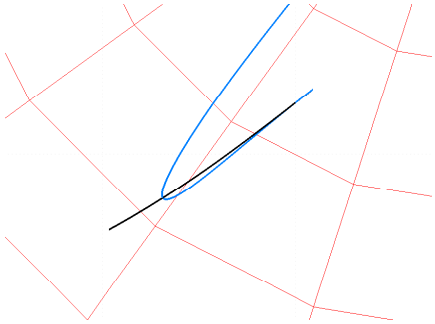

(d) Eye backtracking while the head moves optimally between initial and final point of a measured trajectory from a human subject (closeup view of Fig. 4.6c).

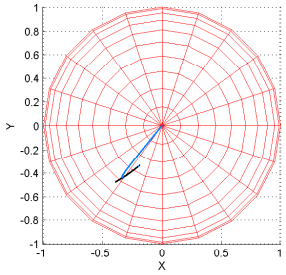

(e) Eye backtracking while the head moves potentially between initial and final point of a measured trajectory from a human subject.

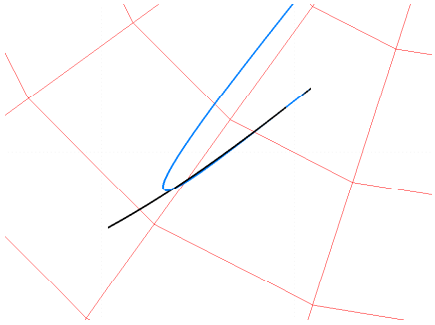

(f) Eye backtracking while the head moves potentially between initial and final point of a measured trajectory from a human subject (closeup view of Fig. 4.6e).

Figure 4.6: The head trajectories are not shown. The blue curves are the eye trajectories projected on the gaze space. The black curve is the computed trajectory $\xi(t)$ that the eye is expected to track, computed based on the head trajectory and the target position.

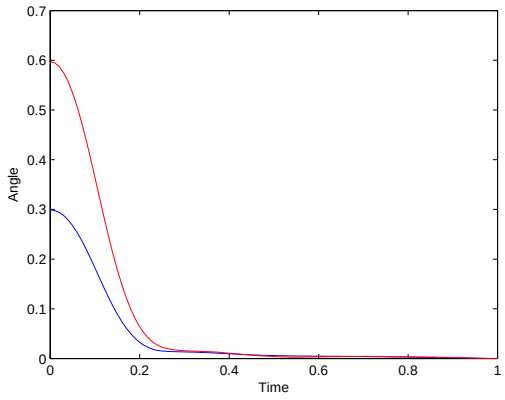

(a) Eye tracking error when head is following observed trajectory from a human subject.

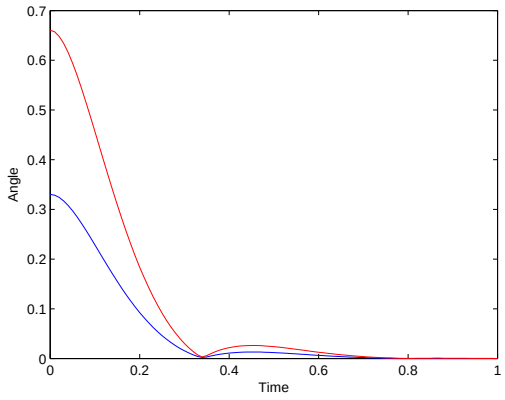

(b) Eye tracking error when head is following optimal trajectory on the Donders' surface with constrained initial and final points.

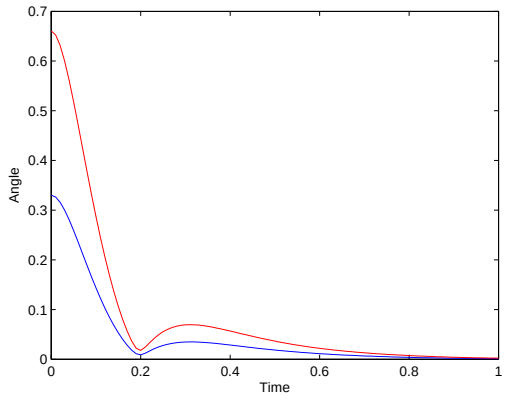

(c) Eye tracking error when head is potentially controlled towards a final point and is constrained by the Donders' surface.

Figure 4.7: Eye tracking error, in torso coordinates, has been expressed as angles. Blue: Angle between the eye quaternion and the target represented as a quaternion. Red: Angle between the eye direction and the target direction.

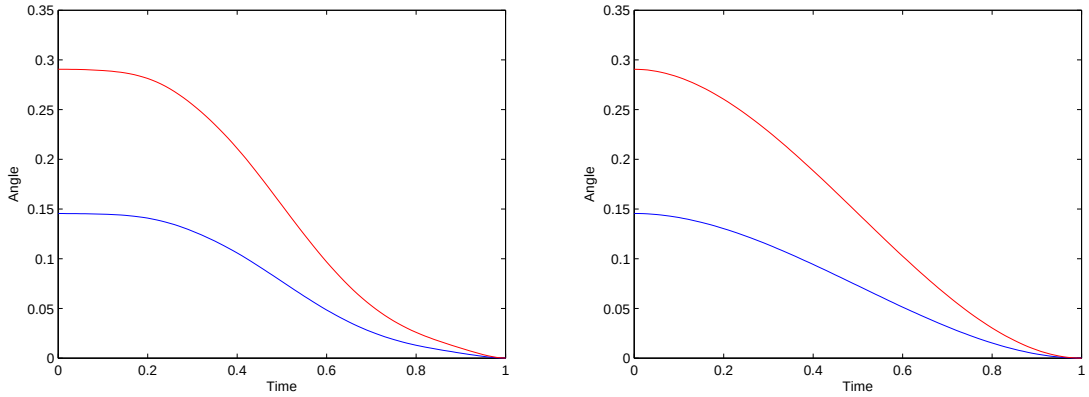

(a) Head is following observed trajectory from a human subject.

(b) Head is following optimal trajectory constrained by the Donders' surface with fixed initial and final conditions.

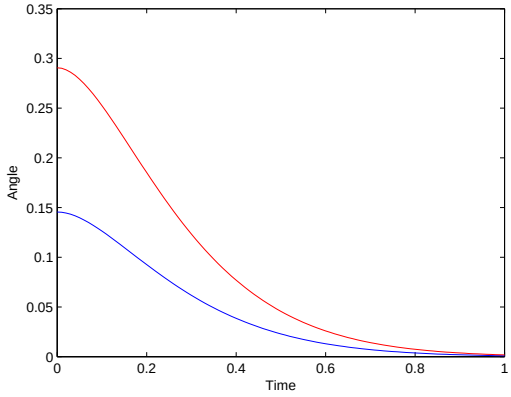

(c) Head follows a path of decreasing potential function towards a final point and is constrained by the Donders' surface.

Figure 4.8: Head error between current and final position, in torso coordinates, has been expressed as angles. Blue: Angle between the 'Current Head Quaternion' and the 'Final Head Quaternion'. Red: Angle between the 'Current Head Direction' and the 'Final Head Direction'.

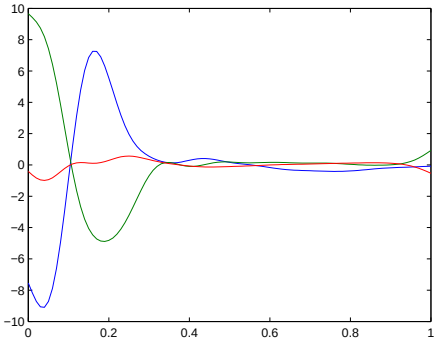

(a) Head and Eye are following a measured trajectory.

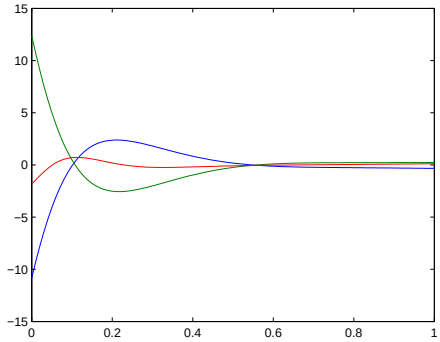

(b) Head is following an optimal trajectory where the end points are constrained and the Eye is backtracking the head.

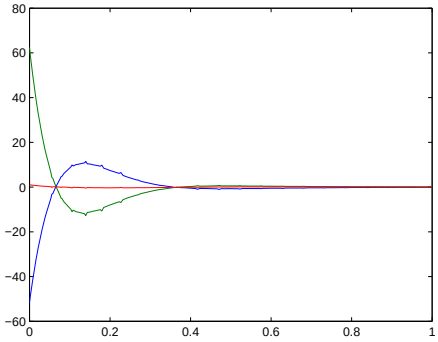

(c) Head is potentially controlled and the Eye is backtracking the head.

Figure 4.9: The figure displays three components of the torque applied to the eye dynamics. In Fig. 4.9a, the torque vector required for the eye dynamics to follow the observed trajectory is displayed. In Figs. 4.9b, 4.9c the optimal and the potential torques are respectively displayed.

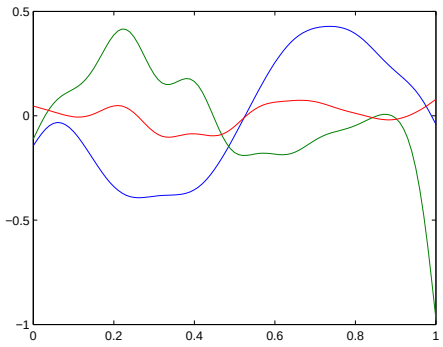

(a) Head and Eye are following a measured trajectory.

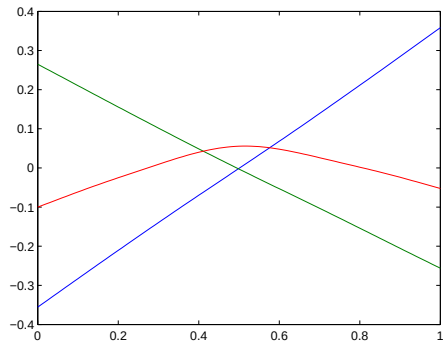

(b) Head is following an optimal trajectory where the end points are constrained and the Eye is backtracking the head..

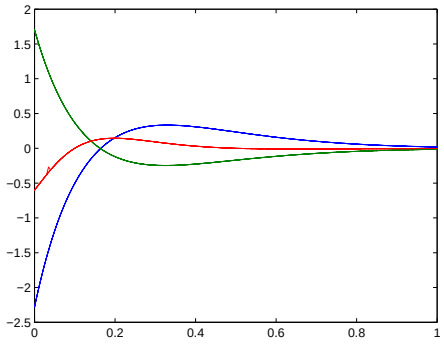

(c) Head is potentially controlled and the Eye is backtracking the head.

Figure 4.10: The figure displays three components of the torque applied to the head dynamics. In Fig. 4.10a, the torque vector required for the head dynamics to follow the observed trajectory is displayed. In Figs. 4.10b, 4.10c the optimal and the potential torques are respectively displayed.

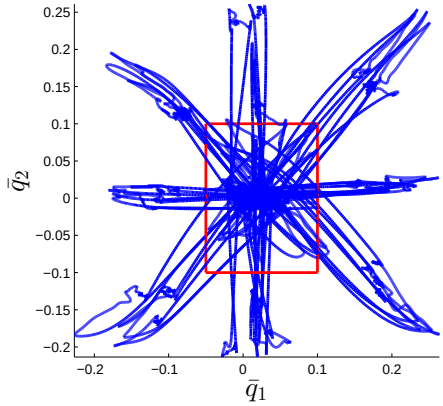

Figure 4.11: The eye trajectory data from Fig. 4.3a projected on the $(\bar{q}_1, \bar{q}_2)$ plane. The red box indicates the threshold for the eye deviation from the straight gaze direction, required to extract individual head/eye trajectories.

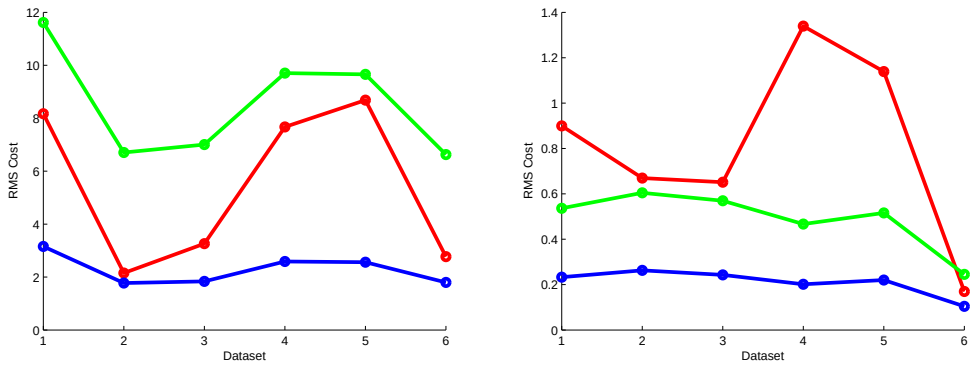

(a) Cumulative RMS Cost of Eye Control. (b) Cumulative RMS Cost of Head Control.

Figure 4.12: RMS Cost of head and eye control cumulated over multiple manoeuvres. Each of the six subjects are indexed from 1 to 6 in the x-axis. The 'blue' color is for the optimal control, 'red' color is for the actual control and the 'green' color is for the potential control.

BIBLIOGRAPHY

[1] R. Abraham and J. E. Marsden. *Foundations of Mechanics*. AMS Chelsea Publishing, American Mathematical Society, Providence, Rhode Island, 1978.

[2] S. L. Altmann. *Rotations, Quaternions, and Double Groups*. Oxford University Press (Hardcover), 1986; Dover Publications (Paperback)., 2005.

[3] K. H. Ang, G. Chong, and L. Yun. PID control system analysis, design and technology. *IEEE Trans. Control Systems Technology*, 13(4):559–576, 2005.

[4] D. Angelaki. Eyes on target: What neurons must do for the vestibuloocular reflex during linear motion. *J. Neurophysiol.*, 92:20–35, 2004.

[5] D. Angelaki and B. J. M. Hess. Control of eye orientation: Where does the brain's role end and the muscle's begin (review article). *European J. of Neuroscience*, 19:1–10, 2004.

[6] W. M. Boothby. *An Introduction to Differentiable Manifolds and Riemannian Geometry*. Academic Press, CA, 1986.

[7] J. Boyd. *Chebyshev and Fourier Spectral Methods*. Dover Publications, New York, second edition, 2000.

[8] Susanne C. Brenner and L. Ridgway Scott. *The Mathematical Theory of Finite Element Methods,* 3^{rd} *Edition*. Springer, New York (Hardcover), 2008.

[9] F. Bullo and A. D. Lewis. *Geometric Control of Mechanical Systems*. Springer Verlag, 2004.

[10] S. L. Campbell and C. D. Meyer Jr. *Generalized Inverses of Linear Transformations*. New York: Dover, 1991.

[11] G. Cannata and M. Maggiali. Models for the design of bioinspired robot eyes. *IEEE Trans. on Robotics*, 24(1):27–44, Feb. 2008.

[12] C. Canuto, M. Y. Hussaini, A. Quarteroni, and T. A. Zang. *Spectral Methods*. Springer, Berlin, 2006.

[13] M. Ceylan, D. Y. P. Henriques, D. B. Tweed, and J. D. Crawford. Task-dependent costraints in motor control: Pinhole goggles make the head move like an eye. *The Journal of Neuroscience*, 20(7):2719–2730, April. 2000.

[14] J. D. Crawford, J. C. Martinez-Trujillo, and E. M. Klier. Control of three-dimensional eye and head movements. *Current Opinion in Neurobiology*, 13(6):655–662, Dec. 2003.

[15] J. D. Cutnell and K. W. Johnson. *Physics, Ninth Edition*. Wiley, Jan 3, 2012.

[16] F. C. Donders. Beiträge zur lehre von den bewegungen des menschlichen auges. *Holländische Beiträge zu den anatomischen und physiologischen Wissenschaften*, 1:104–145, 1848. Press, 1996.

[17] Fletcher Dunn and Ian Parberry. *3D Math Primer for Graphics and Game Develepment, 2^{nd} Edition*. CRC Press, Taylor and Francis Group, Boca Raton, London, New York (Hardcover), 2011.

[18] F. Fahroo and I. Ross. Costate estimation by a legendre pseudospectral method. *J. Guid. Control Dynam*, 24:270–277, 2001.

[19] A. G. Feldman and M. Latash. Testing hypotheses and the advancement of science: recent attempts to falsify the equilibrium point hypothesis. *Exp. Brain Res.*, 161:91–103, 2005.

[20] A. Fick. Neue versuche *ü*ber die augenstellungen. *Untersuchungen zur Naturlehre des Menschen*, 193, 1858.

[21] Charles Fox. *An Introduction to the Calculus of variations*. Oxford University Press (Hardcover), 1954; Dover Publications (Paperback), 2010.

[22] B. K. Ghosh and I. Wijayasinghe. Dynamics of human head and eye rotations under Donders' constraint. *IEEE Trans. on Automat. Contr.*, 57(10):2478–2489, Oct. 2012.

[23] B. K. Ghosh and I. B. Wijayasinghe. Dynamic control of human eye on head system. In *Proc. of the 29^{th} Chinese Control Conference*, pages 5514–5519, Beijing, China, July 2010.

[24] S. Glasauer. Current models of the ocular motor system. *Neuro-Ophthalmology, Dev. Ophthalmology*, 40:158–174, 2007.

[25] S. Glasauer, M. Hoshi, U. Kempermann, T. Eggert, and U. Büttner. Three dimensional eye position and slow phase velocity in humans with downbeat nystagmus. *J. Neurophysiol.*, 89:338–354, 2003.

[26] B. Glenn and T. Vilis. Violations of listing's law after large eye and head gaze shifts. *J. Neurophysiol.*, 68:309–318, 1992.

[27] H. Gomi and M. Kawato. Equilibrium-point control hypothesis examined by measured arm-stiffness during multi-joint movement. *Science*, 272:117–120, 1996.

[28] Andreas Griewank and Andrea Walther. *Evaluating Derivatives: Principles and Techniques of Algorithmic Differentiation,* 2^{nd} *Edition.* SIAM (Softcover), 2008.

[29] A. A. Handzel and T. Flash. The geometry of eye rotations and listing's law. *Adv. Neural Inform. Process. Syst.*, 8:117–123, 1996.

[30] T. Haslwanter. Mathematics of three-dimensional eye rotations. *Vision Res.*, 35(12):1727–1739, 1995.

[31] T. Haslwanter. Mechanics of eye movements: Implications of the orbital revolution. *Ann. N. Y. Acad. Sci.*, 956:33–41, 2002.

[32] A.V. Hill. The heat of shortening and dynamic constants of muscle. *Proc. Roy. Soc. B.*, 126:136–195, 1938.

[33] O. Kremmyda, S. Glasauer, L. Guerrasio, and U. Büttner. Effects of unilateral midbrain lesions on gaze (eye and head) movements. *Ann. N. Y. Acad. Sci.*, 1233:71–77, 2011.

[34] J. B. Kuipers. *Quaternions and Rotation Sequences.* Princeton University Press, 2002.

[35] J. B. Listing. *Beiträge zur physiologischen Optik.* Göttinger Studien, Vandenhoeck und Ruprecht, Göttingen, 1845.

[36] W. P. Medendorp, J. A. M. Van. Gisbergen, M. W. I. M. Horstink, and C. C. A. M. Gielen. Donders' law in torticollis. *J. Neurophysiology*, 82:2833–2838, 1999.

[37] W. P. Medendorp, B. J. M. Melis, C. C. A. M. Gielen, and J. A. M. Van Gisbergen. Off-centric rotation axes in natural head movements: implications for vestibular reafference and kinematic redundancy. *J. Neurophysiology*, 79:2025–2039, 1998.

[38] F. A. Miles and S. G. Lisberger. Plasticity in the vestibulo-ocular reflex: A new hypothesis. *Annual Review of Neuroscience*, 4:273–299, 1981.

[39] H. Misslisch, D. Tweed, and T. Vilis. Neural constraints on eye motion in human eye-head saccades. *J. Neurophysiol.*, 79:859–869, 1998.

[40] R. M. Murray. Nonlinear control of mechanical systems: A lagrangian perspective. *Annu. Rev. Control*, 21:31–45, 1997.

[41] R. M. Murray, Z. Li, and S. S. Sastry. *A Mathematical Introduction to Robotic Manipulation*. CRC, Boca Raton, FL, 1994.

[42] Oliver M. O'Reilly. *Intermediate Dynamics for Engineers: An Unified Treatment of Newton-Euler and Lagrangian Mechanics*. Cambridge University Press, Cambridge, New York, Melbourne, Madrid, CapeTown, Singapore, Sao Paulo, Delhi (Hardcover), 2008.

[43] A. D. Polpitiya, W. P. Dayawansa, C. F. Martin, and B. K. Ghosh. Geometry and control of human eye movements. *IEEE Trans. in Aut. Contr.*, 52(2):170–180, Feb. 2007.

[44] L. S. Pontryagin, V. G. Boltyanskii, R. V. Gamkrelidze, and E. F. Mishchenko. *The Mathematical Theory of Optimal Processes*. John Wiley & Sons, New York, 1962.

[45] P. Radau, D. Tweed, and T. Vilis. Three dimensional eye head and chest orientations following large gaze shifts and the underlying neural strategies. *J. Neurophysiol.*, 72:2840–2852, 1994.

[46] D. Robinson. The mechanics of human saccadic eye movement. *J. Physiol.*, 174:245–264, 1964.

[47] J. Ruths and J.-S. Li. A multidimensional pseudospectral method for optimal control of quantum ensembles. *The Journal of Chemical Physics*, 134:044128, 2011.

[48] Stanley W. Sheppard. Quaternion from rotation matrix. *Journal of Guidance and Control*, 1(3):223–224, May-June, 1978.

[49] S. Smith. Lebesgue constants in polynomial interpolation. *Ann. Math. Informaticae*, 33:109–123, 2006.

[50] D. Stefanatos, J. Ruths, and J.-S. Li. Frictionless atom cooling in harmonic traps: A time-optimal control approach. *Physical Review A*, 882, 063422, 2010.

[51] D. Straumann, T. Haslwanter, M. C. Hepp-Reymond, and K. Hepp. Listing's law for the eye, head, and arm movements and their synergistic control. *Exp. Brain Res.*, 86:209–215, 1991.

[52] M. Theeuwen, L. E. Miller, and C. C. A. M. Gielen. Are the orientations of the head and arm related during pointing movements? *J. Motor Behav.*, 25:242–250, 1993.

[53] D. Tweed. Three dimensional model of the human eye-head saccadic system. *J. Neurophysiology*, 77:654–666, 1997.

[54] D. Tweed, B. Glenn, and T. Vilis. Eye-head coordination during large gaze shifts. *J. Neurophysiol.*, 73:766–779, 1995.

[55] D. Tweed, T. Haslwanter, and M. Fetter. Optimizing gaze control in three dimensions. *Science*, 281(28):1363–1365, Aug. 1998.

[56] D. Tweed and T. Vilis. Implications of rotational kinematics for the oculomotor system in three dimensions. *J. Neurophysiol.*, 58(4):832–849, 1987.

[57] D. Tweed and T. Vilis. Geometric relations of eye position and velocity vectors during saccades. *Vis. Res.*, 30:111–127, 1990.

[58] D. Tweed and T. Vilis. Listing's law for gaze directing head movements. In A. Berthoz, W. Graf, and P. P. Vidal, editors, *The Head-Neck Sensory Motor System*, pages 387–391. New York: Oxford, 1992.

[59] H. von Helmholtz. *Handbuch der Physiologischen Optik.* Number 3, Leopold Voss, Hamburg & Leipzig, 1910. Leipzig: Vos., 3^{rd} edition, 1866.

[60] H. Weyl. *The Concept of a Riemann Surface.* Addison-Wesley Pub. Co. (Hardcover), 1964; Dover Publications (Paperback), 2009.

[61] I. Wijayasinghe, J. Ruths, U. Büttner, B. K. Ghosh, S. Glasauer, O. Kremmyda, and Jr-Shin Li. Axis angle parametrization of the Donders' surface with applications to the head movement control. *International Journal of Control*, 2013.

[62] I. Wijayasinghe, J. Ruths, U. Büttner, B. K. Ghosh, S. Glasauer, O. Kremmyda, and Jr-Shin Li. Potential and optimal control of human head movement using Tait-Bryan parametrization. *submitted to Automatica*, 2013.

[63] F.E. Zajac. Muscle and tendon: Properties, models, scaling and application to biomechanics and motor control. *CRC Critical Reviews in Biomedical Engineering*, 17:359–411, 1989.

[64] William B. J. Zimmerman. *Multiphysics Modelling with Finite Element Methods.* World Scientific Publishing Company, Incorporated, 2006.